An Emission Model for the Particle-in-Cell Method

Vom Fachbereich 18, Elektrotechnik und Informationstechnik der
Technische Universität Darmstadt

zur Erlangung
der würde eines Doktor-Ingenieurs (Dr.-Ing.)
genehmigte

DISSERTATION

von
M.Sc. Jagadish C. Mudiganti
geboren am 18 April 1976 in Hyderabad, Indien

Darmstadt 2006

Referent :	Prof. Dr.-Ing. Thomas Weiland
Korreferent :	Prof. Dr.-Ing. Volker Hinrichsen
Tag der Einreichung :	30.08.2006
Tag der mündlichen Prüfung :	01.11.2006

D 17
Darmstädter Dissertation

Contents

Chapter 1

Motivation

1.1 Importance of an Emission Model

The theory of electron emission and the associated numerical methods used in simulations have been extensively researched and developed over the early and later half of the last century. Ever since a whole gamut of electron devices have been constructed, employing a wide variety of electron sources delivering the current densities required as per the problem specifications. Electron sources can be found in many applications such as cathode ray tubes widely used in display devices, microwave tubes, particle accelerators, plasma generators, optical devices etc.

The design of electron sources begins with the selection of the type of excitation that is to be used in extracting the electrons from an emitting material. It was found from practice that quite a number of the electron devices have often failed to provide the current densities required as the amount of charge that can be drawn from a unit surface area of the emitter is either insufficient, or in a different scenario have short life time when subjected to very high temperatures or electric fields. To overcome the above problems, many techniques have been developed such as maximizing the effective surface area of emission within the restrictions of physical dimensions or by using a variety of material combinations to enable more free electrons inside the material that can be extracted easily. After the extraction, the electrons generated have to be channeled from emitter into the device. For this purpose a set of electrodes are employed to generate fields around the emitter that would draw the electrons from emitter. To make the design process easier and reliable, a variety of simulation tools have been developed that can simulate emission from complex emitter geometries using different excitation methods. In almost all of the emission models that have been developed until

now, approximations are introduced in surface modeling, such as a staircase grid which alters the emission angle of electrons with respect to the actual surface. A tetrahedral grid can overcome the above problem but at the expense of computational time.

In the wake of the above problems the need for a comprehensive emission model that is computationally feasible and at the same time accurate is very much necessary. The work presented in the following chapters will show that all the above problems are addressed systematically and a generalized emission model is developed that is accurate and flexible to meet the requirements of any specific application. The emission model developed here is coupled with the state-of-the-art electromagnetic field solver based on *Finite Integration Technique (FIT)* developed by *Thomas Weiland* in 1977. The *FIT* has seen many useful additions since then, addressing almost the whole spectrum of electromagnetic field problems with the help of a conformal boundary fitted grid. The different steps that are required in an emission model are given in the flow chart Fig.1.1.
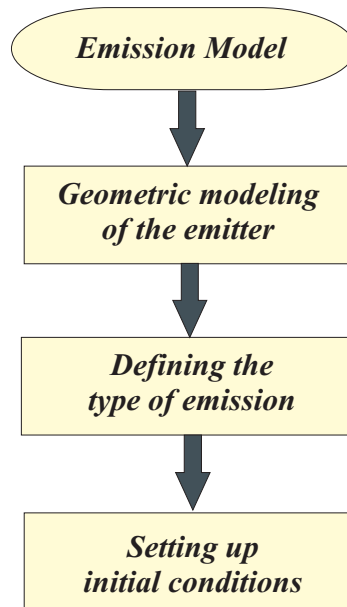
Figure 1.1: Flow chart depicting the tasks of a typical emission model

The first among that process is identifying the physical shape of the electron source and generating a surface grid that will define the spatial distribution

of the electrons. The next step is to identify the type of emission, the materials involved and their properties in order to calculate the current. Once the current is known the charge has to be calculated and assigned to computational particles with a phase space distribution. These tasks essentially constitute the emission model.

1.2   Overview of the Work

In *Chapter* 2 that follows, the *Theory of Electron Emission* is presented, where different processes involved in extracting electrons from materials are discussed and the governing equations for the calculation of current and charge are presented.

In *Chapter* 3 *The Finite Integration Technique (FIT)*, for calculating the field solutions is presented. A brief description of how the *Maxwell equations* are discretized and solved in a problem space is shown. The conformal mesh that is used in the above technique will also be presented.

In *Chapter* 4 *The Particle in Cell method* used in simulating field-charge interaction is discussed. The chapter deals with the methods commonly used in calculation of forces exerted by the external fields on particles and the resulting charged particle dynamics.

The *Chapter* 5 deals with the *Geometric Modeling* of the emitters and a brief introduction to surface grid generation using *Constrained Delaunay Triangulation* algorithm. The different methods to obtain a problem specific surface mesh and emission samples will also be discussed.

In *Chapter* 6 *The Space Charge Limited Emission (SCL)* will be discussed. The various methods by which the current can be calculated under limiting conditions are presented, besides the iterative methods that are used to calculate a field-charge consistency condition are discussed.

In *Chapter* 7 *Simulations and Applications* are presented comparing different methods used in modeling *SCL* emission. As an application problem, simulation of a *Travelling Wave Tube Amplifier (TWTA)* is presented at the end.

In *Chapter* 8 the *Summary* of work is discussed and an *Outlook* on further improvements in the model are mentioned.

Chapter 2

Theory of Electron Emission

2.1 Classification of Solids Based on Conductivity

The fundamental theory of electron emission was developed long back and since then many new mechanisms involving a wide range of materials and geometries have been tried to bolster the performance and current densities required for typical applications. The materials used for electron emission can be broadly classified as conductors and semi-conductors. A cathode or an electron gun is the basic source of electrons. To understand the process of emission it is vital to know the properties of these materials and their energy distribution [1]. The quantum theory states that electrons inside a solid occupy specified energy levels given by their quantum numbers. According to *Fermi-Dirac* statistics electrons fill up all the lower energy levels first. The maximum energy which an electron can have at absolute zero of temperature with all lower energy levels filled is E_f or *Fermi energy*. In other words *Fermi energy* level is the uppermost surface of all energy states where electrons can be found inside a metal. The energy distribution of electrons inside a metal can be written as eq. (2.1)

$$n(E)dE = \frac{4\pi(2m)^{3/2}}{h^3} \left(\frac{\sqrt{E}}{1 + e^{(E-E_f)/kT}} \right) dE \qquad (2.1)$$

where the probability that an energy state is occupied is given by the *Fermi function* as eq. (2.2)

$$f(E) = \frac{1}{1 + e^{(E-E_f)/kT}} \tag{2.2}$$

where $E_f = h^2/2m \, (3n/8\pi)^{2/3}$ is the *Fermi energy*, m is the mass of electron, k is the Boltzmann's constant, T is the temperature in absolute scale and n is the number of electrons per unit volume.

The band theory of solids defines materials based on different energy states occupied by the charge carriers or electrons [2]. The three energy bands with which materials can be classified are valence band, conduction band and the forbidden band or forbidden energy gap. All the highest energy levels of an atom, of a material where electrons are paired constitute the valence band. On the other hand a conduction band is a set energy levels where electrons are free to move inside the material. In other words all unpaired electrons lying in the outermost shell of an atom of a material constitute the conduction band. The forbidden energy gap is the energy band where there are no charge carriers and it separates the valence and conduction bands. Based on these energy band definitions, materials can broadly be classified as

1. **Conductors :** The type of materials where the valance and conduction bands are overlapped and the electrons are free to move inside the material. In other words, materials where the lowest energy levels are all filled and have an excess of electrons filling up the higher energy states extending into the conduction band Fig. 2.1(a).

2. **Semi-Conductors :** The type of materials where the valance and conduction bands are separated by a small energy gap. At room temperature there are fewer charge carriers in the conduction band and an external excitation or impurities is required to enable them to move across into conduction band Fig. 2.1(b).

3. **Insulators :** The materials which have a large energy gap separates the valance and conduction bands. There are hardly any free charge carriers inside the material for conduction. If all the electrons inside an atom are paired up, there can be no electrons free to move inside such a material Fig. 2.1(c).

Now it is easy to deduce from the above argument that for a material to be used as an electron emitter, it should have sufficient number of electrons in the conduction band which can be extracted by a variety of ways discussed in latter sections. This makes the conductors the best choice for emitters,
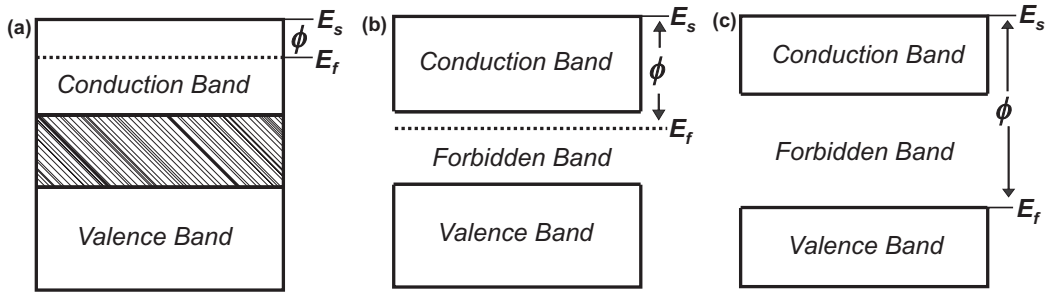
Figure 2.1: (a) The energy band diagram of a conductor. The shaded region is the overlapping of the conduction and valence bands. E_s is the reference energy of unbounded states and E_f is the *Fermi energy* level. ϕ is the potential barrier or work function of the material and it is the energy required for the electron to come to the level of surface energy and escape from the material.
(b) The energy band structure of a semi-conductor with a forbidden energy gap. An electron must cross this energy gap and additionally possess energy to overcome the potential barrier to escape from the material.
(c) The energy band structure of an insulator where there is a large forbidden energy gap separating the conduction and the valence bands, which makes it almost impossible for the electrons to cross into conduction band or escape from the material.

but with new breakthroughs in semi-conductor technology, a wide variety of semi-conductor electron sources are also being developed.

Based on the knowledge of band structure of materials, the *work function ϕ* can now be defined as the difference between the *Fermi energy E_f* and the maximum energy level of the conduction band E_s of a material. In other words, work function is the potential barrier the electrons have to cross before they escape from the material. It is vital to note that semi-conducting materials can have more than one work function. Although the actual work function corresponds to the potential barrier between the *Fermi level* and the surface of the material, it may sometimes include the work function required to bring an electron from valence band into the conduction band.

There are three major kinds of electron emission based on the type of excitation applied to an emitter. These can be classified as

    1. *Thermionic Emission* (electrons extracted by heating the emitter)

2. *Field Emission* (electrons extracted by tunneling under high electric fields)

3. *Photo Emission* (electrons extracted by irradiating emitter with light of suitable frequency)

2.2   Thermionic Emission

When a metal is heated to very high temperatures, electrons gain sufficient energy to overcome the potential barrier and escape from the metal. The electron emission subject to thermal excitation is called *thermionic emission.* For the electrons to be free from the metal, need energy at least equal to *potential barrier* ϕ or *work function* of that particular metal. In other words the energy of an electron after escaping from the metal would be $E \geq E_f + \phi$. Where E_f is the *Fermi energy* as described before. From the energy plot Fig. 2.2 we can conclude that sufficient electrons can escape from surface at very high temperatures. According to *Fermi-Dirac* statistics electrons can be considered as indistinguishable particles in phase space defined by $dxdydzdu_xdu_ydu_z$. In an equilibrium state, the total number of electrons in an elemental volume of a metal can be obtained by multiplying the *Fermi-Dirac probability distribution function* eq. (2.2), with the phase space, which then yields eq. (2.3)

$$dN = \frac{2m^3\nu\, du_x\, du_y\, du_z}{h^3\left(1 + e^{(E-E_f)/kT}\right)} \tag{2.3}$$

where $\nu = dxdydz$ is the elemental volume of the metal. Since we are interested in the current normal to the surface of the metal, we integrate eq. (2.3) over all values of velocities in the normal direction. If z axis is considered as the normal to the metal surface and u_{z0} is the minimum velocity of the electrons after they overcome the potential barrier, the current can be written as

$$J = \frac{2m^3e}{h^3}\int_{-\infty}^{\infty}\int_{-\infty}^{\infty}\int_{u_{z0}}^{\infty}\frac{u_z\, du_x\, du_y\, du_z}{e^{\left(\frac{u^2m}{2} - E_f\right)/kT} + 1} \tag{2.4}$$

where x, y form the plane of the metal surface and $u = \sqrt{(u_x^2 + u_y^2 + u_z^2)}$ is the velocity of electrons inside the metal. The exponential term in the above equation is much higher than one, even for the electrons that are emitted
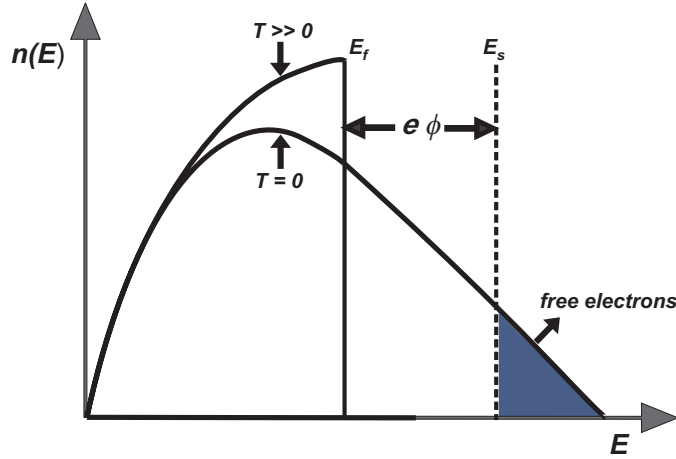
Figure 2.2: The distribution of electrons at room temperature. As the temperature increases electrons which are already at *Fermi level* gain sufficient energy to cross the potential barrier and escape into free space.

with zero velocity, hence the above equation can be rewritten as

$$J = \frac{2m^3 e}{h^3} e^{\frac{E_f}{kT}} \int_{-\infty}^{\infty} e^{-u_x^2 m/2kT}\, dx \int_{-\infty}^{\infty} e^{-u_y^2 m/2kT}\, dy \int_{u_{z0}}^{\infty} u_z\, e^{-u_z^2 m/2kT}\, dz$$

using the standard integrals and rearranging terms one would get

$$J = \frac{4\pi mek^2}{h^3} e^{E_f/kT} T^2 e^{(-u_{z0}^2 m)/2kT} \tag{2.5}$$

where $-u_{z0}^2 m/2 = E$ is the minimum energy which an electron has after it overcomes the potential barrier. Substituting $E - E_f = \phi$, the work function of the metal in the above equation, we get

$$J = A_0 T^2 e^{-\phi/kT} \tag{2.6}$$

which is the well known *Richardson-Dushman* equation for temperature limited current from a metal of unit surface area per unit time [3,4].

where $A_0 = 4\pi mek^2/h^3$ is a constant with a value $120.4 A/cm^2\,^0K^2$, T is the temperature in absolute scale, ϕ is the work function of the metal and k is the Boltzmann's constant.

2.2.1   Schottky Effect

The current derived in eq. (2.6) does not take the external electric field into consideration. In many applications electrons are accelerated with high electric fields after being extracted from the cathode altering the work function of the material and eventually the current Fig. 2.3 [5,6]. This phenomena is called *Schottky effect*. By the method of images the force acting on an electron that is just outside the metal due to a mirror charge inside, separated by a small distance x is obtained by the gradient of potential $-e^2/4x$. Similarly the potential outside the metal due to an anode potential of V volts is $eE_{field}x$, where $E_{field} = -V/d$ and d is the distance of cathode from anode. Now the work function is reduced by the term $e^2/4x + eE_{field}x$, which is the net potential outside the metal due to the image charge plus the external electric field. The maximum reduction in work function can be found by taking the first derivative of the above term, which gives $x = 1/2(e/E_{field})^{1/2}$. The work function is now reduced by an amount $e^{3/2}E_{field}^{1/2}$. The modified *Richardson-Dushman* equation for current under the influence of external electric field can be written as eq. (2.7)

$$J = A_0 T^2 e^{-\left(\phi - e^{3/2}E_{field}^{1/2}\right)/kT} \tag{2.7}$$

where E_{field} is the external electric field.

The charge associated with the current derived in eq. (2.7) can be calculated by knowing the distribution of electrons inside a volume enclosing the surface of the emitter. Now if an electron possesses energy $mu_{z0}^2/2$ after losing energy $mu_z^2/2$ in crossing the potential barrier at the surface, we can write the velocity distribution of electrons as

$$dN_z = \frac{4\pi m^2 kT}{h^3} e^{(E_f - E)/kT} du_z \tag{2.8}$$

Where the energy $E = (mu_{z0}^2/2 + mu_z^2/2)$ is the total energy of all electrons in the volume enclosing the surface of the metal. Integrating the above
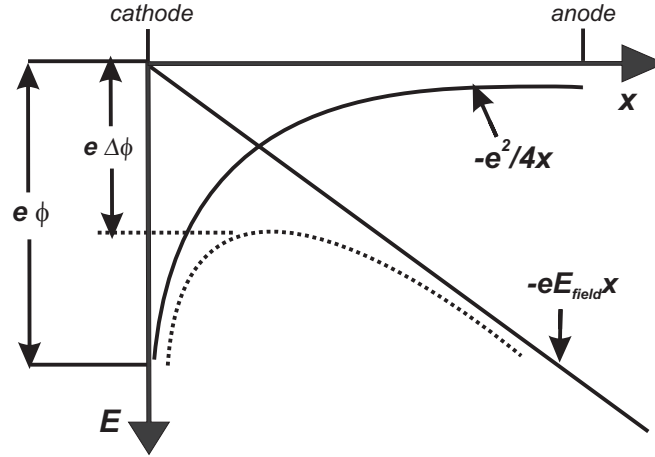
Figure 2.3: The energy E of the electrons plotted as the distance from the cathode x. It can be noted that the work function is reduced by an amount $\Delta\phi$ as the anode potential is steadily increased.

equation and substituting the expression of current in it would result in the equation relating charge associated with the above current density

$$N = \frac{J}{2e}\sqrt{\frac{2m\pi}{kT}} \tag{2.9}$$

where N is the number of electrons coming out of unit surface area of the metal per unit time.

2.2.2 Temperature Variation of the Work-Function

In the equation of current derived in eq. (2.7), we have not considered the temperature variation of the work function. As the temperature of the emitter increases, there will be a change in the bulk properties of that material and consequently a change in the energy levels, so that the work function does not remain the same. The change in work function is given by

$$\phi_0 = \phi + \alpha T$$

where α is a temperature dependent variable evaluated from the Richardson's constant A as $\alpha = k/e\ln(A/A_0)$.

2.3   Field Emission

The quantum mechanics states that, a particle inside a potential well has small but finite probability to escape from the well. Taking the *Schrödinger's stationary wave equation* eq. (2.10)

$$\nabla^2 \psi + \frac{2m}{\hbar^2} E \psi = 0 \tag{2.10}$$

for an electron inside a material defined by periodic potential wells spaced at intervals L, Fig. 2.4, the solution for the above wave function would be

$$\psi = e^{j(\pi n r)/L} u(x, y, z)$$

where $u(x, y, z)$ is a function having same periodicity as the lattice inside the material. It can be seen from the solution that the wave amplitude decays exponentially at the potential barrier, so there exists a probability for the amplitude to be finite on the other side of the barrier. This phenomenon is called *tunneling effect* where electrons with lower kinetic energy tunnel through the higher potential barrier. But the probability of tunneling depends on the width of the potential barrier. If the potential difference between anode and cathode is of the order of several thousand volts, the width of the potential barrier can be reduced to few electron volts thus enabling large number of electrons to tunnel through the barrier. The process of emitting electrons with the application of high electric fields at room temperature is called *field emission.*

To derive the equation for the current we first have to define the *tunneling* or *transmission coefficient*. The transmission coefficient is a function of the kinetic energy of an electron, the external electric field and the potential barrier or the work function of the material. For a potential barrier with no image charge and considering the same notation as before, with $x - y$ plane forming the plane parallel to the surface of the material and z axis normal to the surface, *Fowler* and *Nordheim* have derived the *transmission coefficient* $T(E_z)$ for an electron as

$$T(E_z) = \frac{4\sqrt{E_z(\phi - E_z)}}{\phi} e^{\left(-\frac{4\sqrt{8\pi^2 m/h^2}}{3E_{field}} (\phi - E_z)^{3/2} \right)} \tag{2.11}$$
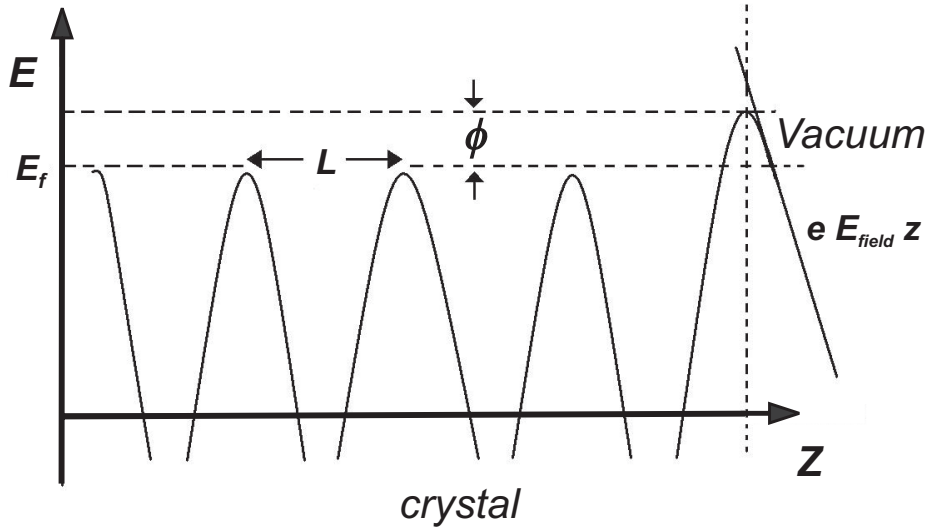
Figure 2.4: The energy level diagram of a crystal with periodicity L. The electric field at the surface is E_{field}. High electric fields enable the electrons to tunnel across the potential barrier into vacuum

where E_z is the kinetic energy of electron normal to the surface of the material, E_{field} is the Electric field and ϕ is the field emission work function of the material.

Recalling the *Fermi-Dirac* distribution function of electrons in the phase space we have

$$dN = \frac{2m^3 \, du_x \, du_y \, du_z}{h^3[1 + e^{(E-E_f)/kT}]} \qquad (2.12)$$

where $E = m(u_x^2 + u_y^2 + u_z^2)/2$ is the total kinetic energy of the electron.

The product of the transmission coefficient and the total number of electrons inside the phase space with normal kinetic energy gives the field emission current eq. (2.13)

$$J = \frac{2em^3}{h^3} \int_0^{\sqrt{2E_f/m}} T(E_z) \, u_z \, du_z \int_{-\infty}^{\infty} \int_{-\infty}^{\infty} \frac{du_x \, du_y}{[1 + e^{(E-E_f)/kT}]} \qquad (2.13)$$

where $\sqrt{2E_f/m}$ is the maximum velocity of electrons at the *Fermi level*. By integrating the eq. (2.13) and assuming that $E_f - E > kT$ we have

$$J = \frac{4\pi m^2 e}{h^3} \int_0^{\sqrt{2E_f/m}} T(E_z) \, u_z \, (E_f - E) \, du_z$$

replacing $E_f - E = \alpha$ and expanding the above equation in terms of this quantity, we have

$$J = \frac{eE_f^{1/2} E_{field}^2}{2\pi h(E_f + \phi)\phi^{1/2}} \, e^{\left(-\frac{4\sqrt{8\pi^2 m/h^2}}{3E_{field}}\phi^{3/2}\right)} \qquad (2.14)$$

which is the *Fowler-Nordheim* equation for the field emission current per unit surface area per unit time [3,7].

The equation above is good for planar field emitters where electric field density over the surface of the material is more or less constant. But in the presence of sharp edges, the local electric field values can be of the order of several thousand volts per unit surface area of the emitter, resulting a high current. We have to include the shape factors of the emitter and also the area of such edges or tips. The current equation is modified for the above corrections, which can be written as

$$J = aE_{field}^2 e^{-b/E_{field}} \qquad (2.15)$$

where $a = 1.4x10^{-6}\alpha\beta^2/(\phi e^{9.8/\sqrt{\phi}})$ and $b = 6.5x10^7\phi^{3/2}/\beta$, α is the area of the effective emission and β is the field enhancement factor.

After obtaining the current from the emitter, we follow the same procedure as in thermionic emission to find the charge associated with this current density. For this we divide current density with eu_z and take integral of u_z over

the same values as in the eq. (2.13)

$$N = \frac{J}{e \displaystyle\int_{-\infty}^{\infty} \int_{-\infty}^{\infty} \int_{0}^{\sqrt{2E_f/m}} \frac{du_x du_y du_z}{(1 + e^{(E-E_f)/kT})}} \tag{2.16}$$

The exponential term in the denominator of eq. (2.16) is very much greater than one, hence neglecting the latter and integrating the equation gives the charge associated with the current eq. (2.14)

$$N = \frac{Jm^2}{2\pi e k^2 T^2} \tag{2.17}$$

2.4   Photo-Electric Emission

When a metal or semi-conductor is irradiated by light of suitable frequency it emits electrons. The electron absorbs a quantum of energy $h\nu$ from a photon and gains sufficient kinetic energy to escape from the material Fig. 2.5. This phenomenon is known as *photo-emission*. The number of electrons emitted depends on the intensity and the frequency of the incident light. Besides the material properties, there is a minimum frequency of the radiation that is required to generate current. The energy required by a photon to emit an electron is $h\nu_0$, where ν_0 is the lower limit of the frequency known as cutoff frequency. To emit an electron from the material this energy must be at least equal to the work function of the material

$$h\nu_0 = \phi$$

writing the above equation in terms of the cutoff wavelength we have

$$\lambda_0 = \frac{12.36x10^{-7}}{\phi} m \tag{2.18}$$

Following the same approach as in *thermionic* and *field emission*, the velocity distribution when multiplied by the transmission coefficient gives the total current. *Fowler* considered the probability of transmission to be a constant
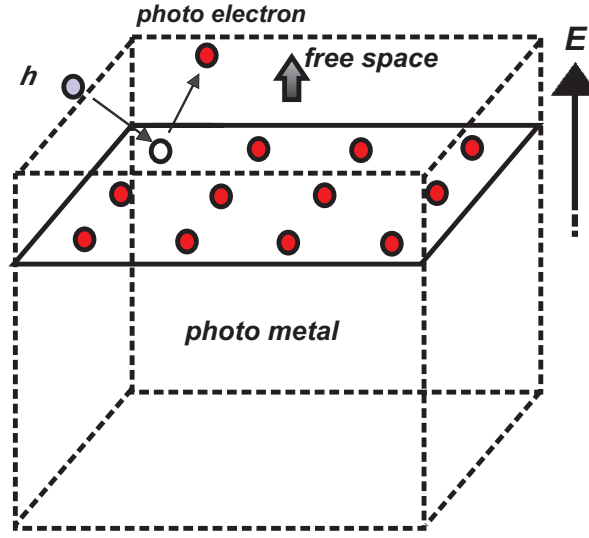
Figure 2.5: The figure illustrates the photo-emission. A photon of energy $h\nu$ impinges on an electron at the *Fermi energy level* and transfers its energy to the electron, which then has sufficient kinetic energy to escape the metal.

since the energy spectrum of photo electrons is narrow. If we call the probability of transmission as a constant α and write the distribution function in terms of normal energy, we have the equation for current as

$$J = \frac{4\pi m e k^2 T^2 \alpha}{h^3} \int_{E_c-h\nu}^{\infty} \ln(1 + e^{(E_f-E)/kT}) dE_z \qquad (2.19)$$

where E_c is the critical energy an electron needs to escape potential barrier or $E_c - E_f = \phi$. Integrating the above equation would give the photo current per unit surface area of a metal [3]

$$J = \alpha A_0 T^2 f(x) \qquad (2.20)$$

where,

$$f(x) = \begin{cases} e^{-x} - \frac{e^{-2x}}{4} + \frac{e^{-3x}}{9} - \ldots & \text{for } u_0 \leq 1 \\[2ex] \frac{x^2}{2} + \frac{\pi^2}{6} - \left(e^{-x} - \frac{e^{-2x}}{4} + \frac{e^{-3x}}{9}\right)\ldots & \text{for } u_0 > 1 \end{cases}$$

$$x = \frac{(\nu - \nu_0)}{kT} \tag{2.21}$$

Again considering a thermal velocity spread inside the metal and dividing eq. (2.19) with gives the total charge per unit surface area of the metal

$$N = \frac{JkT}{ef(x)} \tag{2.22}$$

where $f(x)$ has the same meaning as above.

Chapter 3

The Finite Integration Technique

3.1 Maxwell's Equations

The methods to obtain the solutions of electromagnetic fields can be broadly classified into two categories. The ones, that give exact solutions of the mathematical relations governing a field problem, known as analytical methods and those which give approximate solutions accommodating more complex field problems and are known as numerical methods. The choice of a method depends on the problem space over which the solutions are to be obtained, the kind of mathematical relations governing the problem and the boundary conditions that have to be fulfilled by the solutions. It is obvious that analytical solutions cannot be obtained for problems involving complex physical geometries or for inhomogeneous, anisotropic medium or mixed, time dependent boundary conditions. In such cases numerical methods are applied to get accurate solutions depending on the number of constraints. Here we discuss the *Finite Integration Technique (FIT)* as the basis for field solutions and show how the discrete representation is consistent with the general laws of electromagnetics. We also discuss the flexibility of the method in handling complex surfaces and material definitions, which would be vital for the development of an emission model discussed in later chapters.

The laws governing the classical electromagnetic theory are given by *Maxwell equations* [8]. In a stationary state the integral and consecutive differential forms can be written as

$$\oint_{\partial A} \vec{E}(\vec{r},t) \cdot d\vec{S} = - \int_A \frac{\partial \vec{B}(\vec{r},t)}{\partial t} \cdot d\vec{A} \Longleftrightarrow \nabla \times \vec{E}(\vec{r},t) = \frac{\partial \vec{B}(\vec{r},t)}{\partial t} \qquad (3.1)$$

$$\oint_{\partial A} \vec{H}(\vec{r},t) \cdot d\vec{S} = \int_A \left(\frac{\partial \vec{D}(\vec{r},t)}{\partial t} + \vec{J}(\vec{r},t) \right) \cdot d\vec{A} \Longleftrightarrow$$
$$\nabla \times \vec{H}(\vec{r},t) = \frac{\partial \vec{D}(\vec{r},t)}{\partial t} + \vec{J}(\vec{r},t) \qquad (3.2)$$

$$\int_{dV} \vec{D}(\vec{r},t) \cdot d\vec{A} = \int_V \rho(\vec{r},t) \cdot dV \Longleftrightarrow \nabla \cdot \vec{D}(\vec{r},t) = \rho(\vec{r},t) \qquad (3.3)$$

$$\int_{dV} \vec{B}(\vec{r},t) \cdot d\vec{A} = 0 \Longleftrightarrow \nabla \cdot \vec{B}(\vec{r},t) = 0 \qquad (3.4)$$

where $\vec{E}$ and $\vec{H}$ are the electric and magnetic field strengths, and $\vec{D}$ and $\vec{B}$ are the electric and magnetic flux densities $\forall\ A, V \in \Re^3$. For a non steady state field problem, the conservation of charge was later on included into *Ampere's law* by *Maxwell* in the form of continuity equation

$$\oint_{\partial A} \vec{J}(\vec{r},t) \cdot d\vec{A} = - \int_V \frac{\partial \rho(\vec{r},t)}{\partial t} \cdot dV \Longleftrightarrow \nabla \cdot \vec{J}(\vec{r},t) = \frac{\partial \rho(\vec{r},t)}{\partial t} \qquad (3.5)$$

where $\vec{J}$ and ρ are the current and charge densities respectively. The field strengths and the flux densities mentioned in the equations (3.1)-(3.5) are related to each other through material parameters. In the absence of permanent electric or magnetic polarizations, the material equations for an isotropic medium are

$$\begin{aligned}
\vec{D}(\vec{r},t) &= \varepsilon \vec{E}(\vec{r},t) \\
\vec{B}(\vec{r},t) &= \mu \vec{H}(\vec{r},t) \\
\vec{J}(\vec{r},t) &= \vec{J_i}(\vec{r},t) + \kappa \vec{E}(\vec{r},t)
\end{aligned} \qquad (3.6)$$

where ε, μ, κ are the permittivity, permeability and conductivity respectively. $\vec{J_i}(\vec{r},t)$ term is associated with free current sources. The eq.'s (3.1)-(3.6) along with initial and boundary conditions completely define an electromagnetic field problem.

3.2 Finite Integration Algorithm

The numerical solutions to the *Maxwell's Equations* require discretization of a bounded problem space Fig. 3.1 [9]. The grid that encompasses the problem space is a collection of a finite number of non-overlapping cells, each of which will uniquely hold the information of the continuous space variables. The topology of these cells will be lines or edges, faces and volumes in one, two and three dimensions respectively and together they form a cell complex G.
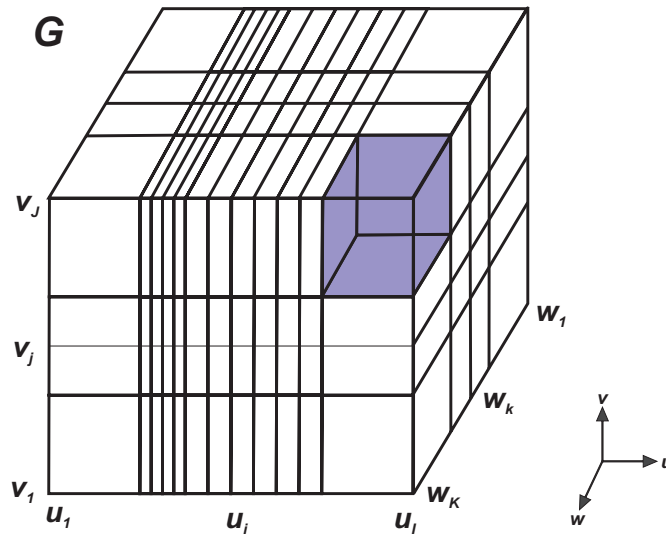

Figure 3.1: A Cartesian grid that expands along a problem domain with a total number of grid points $N_p = I * J * K$ and each cell index given by $n(i, j, k) = i + (j-1)I + (k-1)IJ$. I, J, K being the total number of points on each axes of the coordinate system.

3.2.1 Grid Maxwell Equations

The *Finite Integration Technique* discretizes the *Maxwell integral equations* in the problem space using a dual staggered grid complex G and $\tilde{G}$ [10]. The need for such a dual grid arrangement stems from the fact that the *Maxwell equations* are coupled with electric and magnetic fields inter-related to each other and the dual grid arrangement represents a geometrical equivalent of these equations. Both of these cell complexes, referred as primary and dual

grid are constructed in such a way that the nodes of a cell from primary grid form the barycenters of the corresponding cell of the dual grid and vice versa. Now we shall discuss the *FIT* with the help of a simple three-dimensional Cartesian grid although it can be implemented in general for any orthogonal, non-orthogonal or unstructured grids. The method also includes sub-grids used in the problems that require local mesh refinement. With the help of dual grid system we can now write the *Finite Integration (FI)* state variables as [11,12]

$$
\begin{aligned}
\hat{e}_r &= \int_{L_r} \vec{E}(\vec{r}) \cdot d\vec{S} & \hat{h}_r &= \int_{\tilde{L}_r} \vec{H}(\vec{r}) \cdot d\vec{S} \\
\hat{\hat{d}}_r &= \int_{\tilde{A}_r} \vec{D}(\vec{r}) \cdot d\vec{A} & \hat{\hat{b}}_r &= \int_{A_r} \vec{B}(\vec{r}) \cdot d\vec{A} & (3.7) \\
\hat{\hat{j}}_r &= \int_{\tilde{A}_r} \vec{J}(\vec{r}) \cdot d\vec{A} & q_r &= \int_{\tilde{V}_r} \rho(\vec{r}) dV
\end{aligned}
$$

Where $L_r, \tilde{L}_r, A_r, \tilde{A}_r, \tilde{V}_r$ are the lengths of the edges, area of the faces and volume of each primary and dual cells respectively. As can be seen from the Fig. 3.2 the electric and magnetic field strengths are integrated along the edges of the primary and dual grids, respectively. Similarly the electric and magnetic fluxes are integrated over the faces of each cell of the primary and dual grids.

Taking one face of a primary grid cell fig. 3.3(a),3.3(b), we can write the discrete counterpart of eq. (3.1) as

$$
\hat{e}_u(i,j,k) + \hat{e}_v(i+1,j,k) - \hat{e}_u(i,j+1,k) - \hat{e}_v(i,j,k) = -\frac{d}{dt}\hat{\hat{b}}_w(i,j,k+1))
$$

The above discretization is applied to the rest of the edges and faces of the grid complex $G, \tilde{G}$ to obtain a set of independent algebraic equations that can be written in matrix form as

$$
\mathbf{C\hat{e}} = -\frac{\mathbf{d}}{\mathbf{dt}}\hat{\hat{\mathbf{b}}}
$$

Following the same approach and considering eq. (3.4), the discretization of fluxes over the faces of a cell fig.3.4(a),3.4(b), can be written as
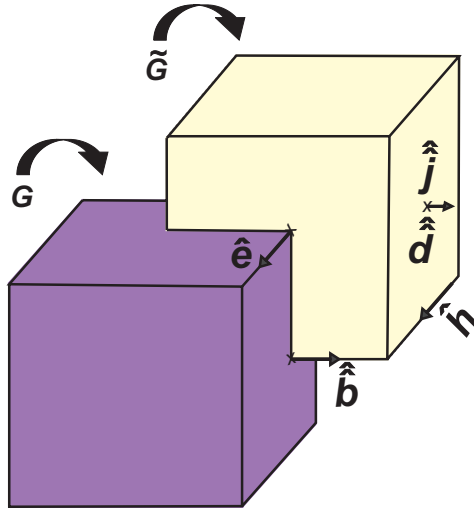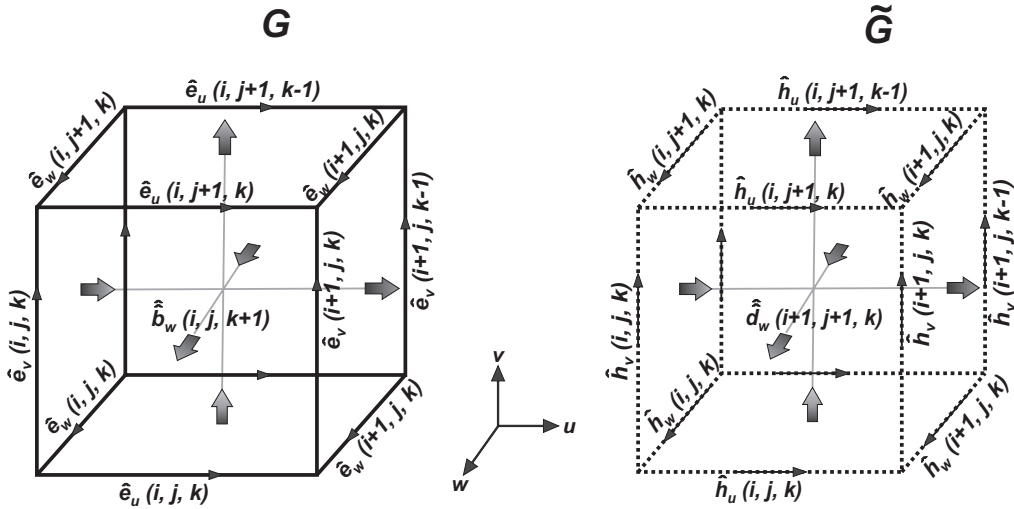
Figure 3.2: The grid couplet in *FIT*

Figure 3.3: (a) Electric field components along primary grid edges.
(b) Magnetic field components along dual grid edges.

$$-\hat{\hat{b}}_u(i-1,j,k)+\hat{\hat{b}}_v(i,j,k)-\hat{\hat{b}}_v(i,j,k)+\hat{\hat{b}}_v(i,j-1,k)-\hat{\hat{b}}_w(i,j,k)+\hat{\hat{b}}_w(i,j,k+1)=0$$

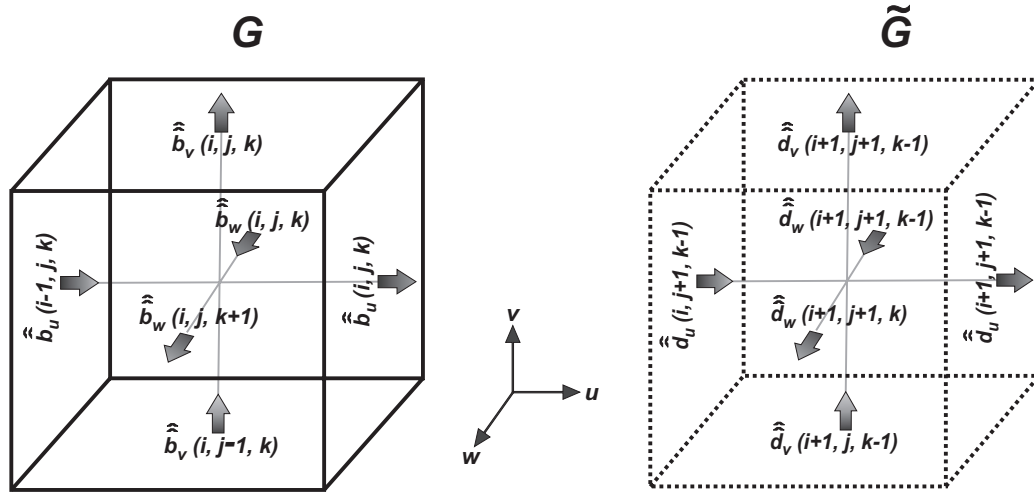which, for the entire grid complex, will transform into matrix form as

Figure 3.4: (a) Magnetic flux on the faces of primary grid or, consequently, along the edges of dual grid.
(b) Electric flux on the faces of dual grid or, consequently, along the edges of primary grid.

$$\mathbf{S}\hat{\hat{\mathbf{b}}} = \mathbf{0}$$

After similar discretization of the other two *Maxwell equations*, with magnetic field components along the edges of dual grid $\tilde{G}$ and electric current and flux densities over the faces, we obtain a set of matrix equations referred to as *Maxwell Grid Equations (MGE)*.

$$
\begin{aligned}
\mathbf{C}\hat{\mathbf{e}} &= -\frac{\mathbf{d}}{\mathbf{dt}}\hat{\hat{\mathbf{b}}} \\
\mathbf{\tilde{C}}\hat{\mathbf{h}} &= \frac{\mathbf{d}}{\mathbf{dt}}\hat{\hat{\mathbf{d}}} + \hat{\hat{\mathbf{j}}} \\
\mathbf{\tilde{S}}\hat{\hat{\mathbf{d}}} &= \mathbf{q} \\
\mathbf{S}\hat{\hat{\mathbf{b}}} &= \mathbf{0}
\end{aligned}
\tag{3.8}
$$

Where $\mathbf{C}, \mathbf{\tilde{C}}, \mathbf{S}, \mathbf{\tilde{S}}$ are topological matrices with elements carrying a value of either -1,0,1 and are the discrete counterparts of the continuous differential operators **curl** and **div**. We can see from the above equations that $\mathbf{C}, \mathbf{\tilde{C}}$ are the discrete **curl** operators on primary and dual grids respectively and they only carry information on how the electric and magnetic field components, $\hat{e}$

and $\hat{h}$ are integrated on both the grids. Likewise, the discrete **div** operators $\mathbf{S}, \tilde{\mathbf{S}}$ will carry the information to integrate the electric and magnetic flux $\hat{\tilde{d}}$ and $\hat{\tilde{b}}$ on the dual grid system.

The discrete **curl** and **div** operators so obtained can be verified to fulfil the analytical relations [11]

$$\begin{aligned}
\mathbf{div\,curl} = \mathbf{0} &\iff \mathbf{SC} = \mathbf{0}, \tilde{\mathbf{S}}\tilde{\mathbf{C}} = \mathbf{0} \\
\mathbf{curl\,grad} = \mathbf{0} &\iff \mathbf{C}\tilde{\mathbf{S}}^{\mathbf{T}} = \mathbf{0}, \tilde{\mathbf{C}}\mathbf{S}^{\mathbf{T}} = \mathbf{0}
\end{aligned}$$

The fulfillment of the above algebraic properties by the discrete system ensures the conservation of charge and energy.

3.3   Material Operators in *FIT*

The *Maxwell Grid Equations (MGE)* are exact and no approximations have been made while discretizing them [14]. The approximations come into play when we consider material equations relating the fields to their flux densities. The first step is to discretize the material equations with respect to the dual grid complex, which will again result in a set of matrix equations,

$$\begin{aligned}
\hat{\tilde{\mathbf{d}}} &= \mathbf{M}_\varepsilon \hat{\mathbf{e}} \\
\hat{\tilde{\mathbf{b}}} &= \mathbf{M}_\mu \hat{\mathbf{h}} \\
\hat{\tilde{\mathbf{j}}} &= \mathbf{M}_\kappa \hat{\mathbf{e}} + \hat{\tilde{\mathbf{j}}}_{\mathbf{i}}
\end{aligned} \tag{3.9}$$

where $\mathbf{M}_\varepsilon, \mathbf{M}_\mu, \mathbf{M}_\kappa$ are the discrete material matrices.

Here we have to make a note that since the material distribution may not be continuous across each primary-dual grid couplet, we have to find an approximation technique that would average the material properties and enable us to solve the above equations. Let us consider the first of eq. (3.9) where we have the permittivity ε of the medium connecting the electric flux $\hat{\tilde{d}}$ integrated on dual grid faces to the electric field $\hat{e}$ integrated along the edges of the primary grid. The first assumption is to consider a homogenous material distribution in the primary grid cell as shown in the Fig. 3.5(a). As can

be seen, each of the four primary grid cells are filled with a material of permittivity $\varepsilon_1, \varepsilon_2, \varepsilon_3, \varepsilon_4$ respectively and the dual grid face which cuts through each of the primary grid cells has areas $\tilde{A}_1, \tilde{A}_2, \tilde{A}_3, \tilde{A}_4$ respectively. Now the permittivity on this dual grid face can be averaged as

$$\bar{\varepsilon} = \frac{\varepsilon_1 \tilde{A}_1 + \varepsilon_2 \tilde{A}_2 + \varepsilon_3 \tilde{A}_3 + \varepsilon_4 \tilde{A}_4}{\tilde{A}_1 + \tilde{A}_2 + \tilde{A}_3 + \tilde{A}_4} \tag{3.10}$$

Extending the same argument to the case of conductivity κ, where the current density on a dual grid face is coupled to the electric field vector along the edges of primary grid cells, we write the average conductivity on a dual grid face as

$$\bar{\kappa} = \frac{\kappa_1 \tilde{A}_1 + \kappa_2 \tilde{A}_2 + \kappa_3 \tilde{A}_3 + \kappa_4 \tilde{A}_4}{\tilde{A}_1 + \tilde{A}_2 + \tilde{A}_3 + \tilde{A}_4} \tag{3.11}$$
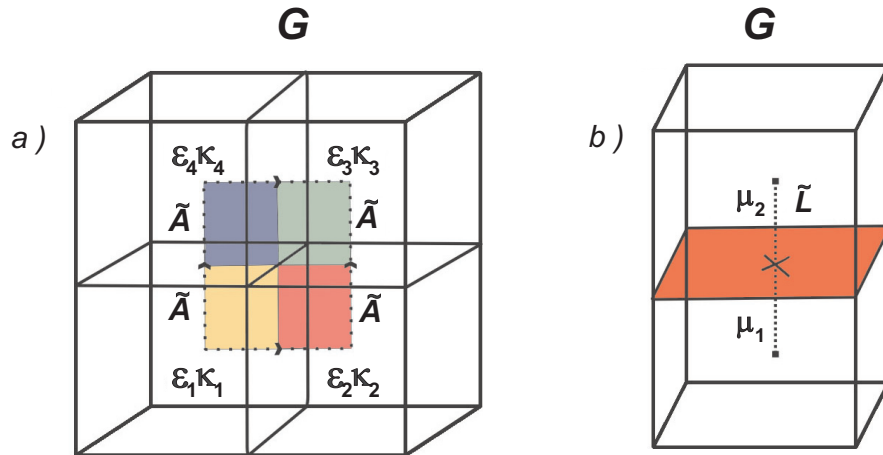

Figure 3.5: (a) Averaging permittivity and conductivity along a dual grid face. (b) Averaging Permeability along a dual grid edge.

The remaining material parameter to be averaged is permeability μ that couples the magnetic flux $\hat{\vec{b}}$ from a primary grid face to the magnetic field $\hat{h}$

along the corresponding dual grid edges, fig. 3.5(b). As we already assumed the material filling of a primary grid cell to be homogenous the average of permeability along a dual grid edge is,

$$\bar{\mu} = \frac{\mu_1 \tilde{L}_1 + \mu_2 \tilde{L}_2}{\tilde{L}_1 + \tilde{L}_2} \tag{3.12}$$

For homogenous, isotropic material distribution the above averaging when applied to the entire grid complex will result in a set of diagonal matrices $\mathbf{D}_\varepsilon, \mathbf{D}_\kappa, \mathbf{D}_\mu$. Until now we have averaged only the material parameters and are yet to couple the grid voltages on the edges to the flux densities on the faces of a grid cell. If we consider the field and flux to be constant along the edges and faces, the final discrete material equations can be written as

$$\frac{\int_{\tilde{A}_i} \vec{D}(\vec{r}) \cdot d\vec{A}}{\int_{L_i} \vec{E}(\vec{r}) \cdot d\vec{S}} \approx \frac{\bar{\varepsilon}_i |\tilde{A}_i|}{|L_i|} = \frac{\hat{\hat{\mathbf{d}}}_i}{\hat{\mathbf{e}}_i} \quad \implies \quad \frac{[\mathbf{D}_\varepsilon]_\mathbf{i}[\tilde{\mathbf{D}}_\mathbf{A}]_\mathbf{i}}{[\mathbf{D}_\mathbf{S}]_\mathbf{i}} = \frac{\hat{\hat{\mathbf{d}}}}{\hat{\mathbf{e}}} \quad \implies \quad \hat{\hat{\mathbf{d}}} = \mathbf{M}_\varepsilon \hat{\mathbf{e}}$$

$$\frac{\int_{\tilde{A}_i} \vec{J}(\vec{r}) \cdot d\vec{A}}{\int_{L_i} \vec{E}(\vec{r}) \cdot d\vec{S}} \approx \frac{\bar{\kappa}_i |\tilde{A}_i|}{|L_i|} = \frac{\hat{\hat{\mathbf{j}}}_i}{\hat{\mathbf{e}}_i} \quad \implies \quad \frac{[\mathbf{D}_\kappa]_\mathbf{i}[\tilde{\mathbf{D}}_\mathbf{A}]_\mathbf{i}}{[\mathbf{D}_\mathbf{S}]_\mathbf{i}} = \frac{\hat{\hat{\mathbf{j}}}}{\hat{\mathbf{e}}} \quad \implies \quad \hat{\hat{\mathbf{j}}} = \mathbf{M}_\kappa \hat{\mathbf{e}}$$

$$\frac{\int_{\tilde{L}_i} \vec{H}(\vec{r}) \cdot d\vec{S}}{\int_{A_i} \vec{B}(\vec{r}) \cdot d\vec{A}} \approx \frac{\bar{\mu}_i^{-1} |\tilde{L}_i|}{|A_i|} = \frac{\hat{\mathbf{h}}_\mathbf{i}}{\hat{\hat{\mathbf{b}}}_\mathbf{i}} \quad \implies \quad \frac{[\mathbf{D}_\mu^{-1}] \cdot [\tilde{\mathbf{D}}_\mathbf{S}]}{\mathbf{D}_\mathbf{A}} = \frac{\hat{\mathbf{h}}}{\hat{\hat{\mathbf{b}}}} \quad \implies \quad \hat{\hat{\mathbf{b}}} = \mathbf{M}_\mu \cdot \hat{\mathbf{h}}$$

where, $\mathbf{D}_\mathbf{A}, \tilde{\mathbf{D}}_\mathbf{A}, \mathbf{D}_\mathbf{S}, \tilde{\mathbf{D}}_\mathbf{S}$ are the diagonal area and edge length matrices for primary and dual grids respectively, and $\mathbf{M}_\varepsilon = \mathbf{D}_\varepsilon \tilde{\mathbf{D}}_\mathbf{A} \mathbf{D}_\mathbf{S}^{-1}$, $\mathbf{M}_\kappa = \mathbf{D}_\kappa \tilde{\mathbf{D}}_\mathbf{A} \mathbf{D}_\mathbf{S}^{-1}$, $\mathbf{M}_\mu = \mathbf{D}_\mu \mathbf{D}_\mathbf{A} \tilde{\mathbf{D}}_\mathbf{S}^{-1}$ are the final matrices that have complete information about materials and the grid dimensions.

3.4 Conformal Material Operators

The approach to discretize materials, discussed in the previous section will result in a staircase approximation of curved objects, as can be seen in Fig 3.6(a). Taking a fine mesh would increase the computational costs and may

still lead to erroneous results for problems that are curvature dependent. As will be seen in later chapters, the process of emission requires the field components normal to the surface and in such cases a staircase mesh will fail to provide the right field values on the boundary. There are many schemes under *FIT* that can handle this problem depending on the accuracy required and computational costs that can be afforded. The first of them are triangular Fig. 3.6(b) or tetrahedral material fillings inside the volume of a cell. This method has a better description of the boundaries than the staircase approximation. There also exists sub-grid schemes that can make a refinement of the mesh locally at a curved boundary Fig. 3.6(c) [15]. The non-orthogonal grid as shown in Fig. 3.6(d) can handle the problem of curved boundaries with much higher efficiency but at the expense of additional computational costs in interpolating the fields and flux densities on the grid couplet which now are non-orthogonal to each other [16]. A new technique called *Conformal Finite Integration Technique (CFIT)* as seen from Fig. 3.6(e), is capable of accurately modeling the curved boundaries even with coarser grids and is very apt for the problem of emission [17]. This method preserves the orthogonal structure of the original *FIT* by keeping the topological matrices intact, but adjusts the material matrices with the new edge lengths and areas of the faces, considering the exact material intersections with each edge and face of the primary and dual grid cells. The re-adjustment of material matrices take only a little more of computational time during pre-processing but will give accurate results for the fields on boundaries. Because of the requirement of high field accuracy in emission modeling, this technique is used in all simulations in this work.

3.5   Electro- and Magneto-statics

In field problems where only the steady state response of the system is of interest, the *FIT* will employ a static field solver, which in turn will considerably reduce the computational burden. Here the *Poisson's equation* is solved by defining scalar potentials ϕ on cell nodes. The corresponding fields can be obtained by taking the gradient of these potentials along the corresponding cell edges [18].

$$\vec{E}(\vec{r}) = -grad\phi_e(\vec{r}) \tag{3.13}$$

Substituting the above equation into eq (3.5) and the corresponding result into eq. (3.2) will yield
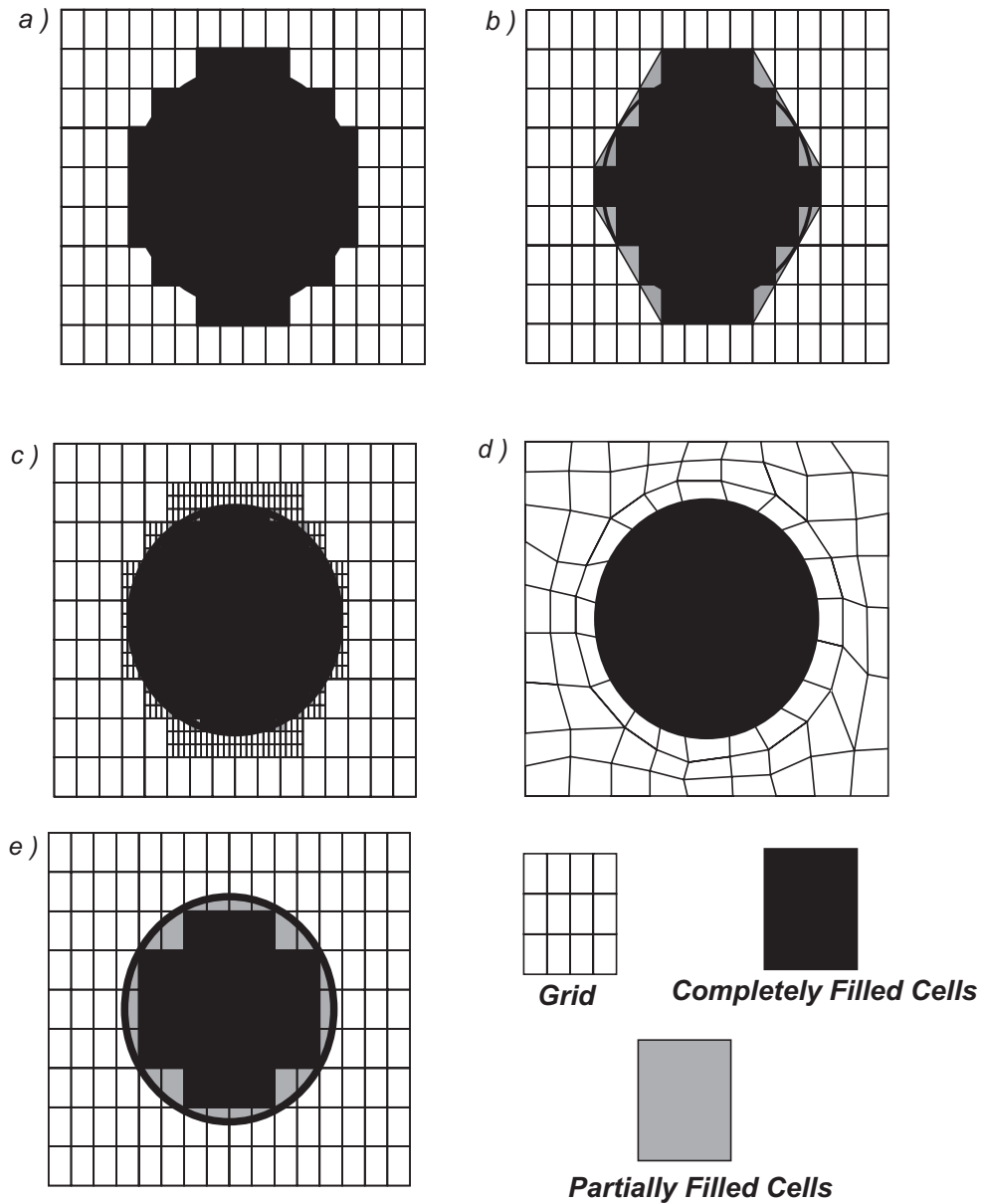
Figure 3.6: (a) Staircase approximation. (b) Triangular filling of material. (c) Sub-grid technique applied near material boundaries. (d) Non-orthogonal grid. (e) Conformal Boundary Approximation technique considers the exact material filling inside each grid cell ensuring the solutions to be accurate on the boundaries.

$$\nabla \cdot (\varepsilon \nabla \phi_e(\vec{r})) = -\rho(\vec{r}) \tag{3.14}$$

which is *Poisson's equation*. Using the topological and material matrices the above equation can be transformed into discrete form as

$$\mathbf{S}\mathbf{D}_\varepsilon \tilde{\mathbf{D}}_\mathbf{A} \mathbf{D}_\mathbf{S}^{-1} \tilde{\mathbf{S}}^\mathbf{T} \phi_\mathbf{e} = -\mathbf{q_e} \tag{3.15}$$

Where, $\tilde{\mathbf{S}}^\mathbf{T} = -\mathbf{G}$ is the gradient matrix and q_e the total charge enclosed inside a grid cell. Once the boundary conditions are specified, the above matrix equation can be solved.

The magneto-static fields are solved in similar way. The magnetic field from permanent magnets is calculated using the static field solver of *CST EM STUDIO* and is imported into the emission model [19,20]. The magneto-static solver need not be executed in each iteration cycle since only static magnetic fields are considered in emission model. The fields produced by the electrons are neglected as the simulations performed in this work are non-relativistic.

Chapter 4

The Particle-in-Cell Method

The systems containing charged particles and external forces acting upon them have been studied by many different methods. The basic mathematical model of all these methods is to simulate the physical phenomena with an appropriate computational model reproducing the original system as closely as possible. The simulation method defines a six dimensional phase space (positions and velocities in 3D) distribution of the test particles, an interpolation method to find the forces acting on the particles and an appropriate solution for the equations of motion. Here we give a brief overview of different methods used for simulating particle systems.

It can be observed that most of the fluid dynamic problems or plasma simulations use the *magneto-hydrodynamic (MHD)* method where the electrically conducting fluid dynamics is modeled with the combination of *Navier-Stokes* and the *Maxwell equations*. In this method the phase space distribution function, such as *Maxwell-Boltzmann*, defines the positions and velocities of the charged particles macroscopically. This method usually suits large physical systems where the simulation of macroscopic behaviour of the charged particles would suffice. On the other hand it is often required to study the dynamics of the system before it reaches an equilibrium state, that demands a study of the physical phenomena microscopically. One way to do this is by defining particles in the six dimensional phase space given by the *Vlasov equation* [22]

$$f(\vec{x}, \vec{p}, t) = \frac{\partial f}{\partial t} + \frac{\vec{p}}{m} \frac{\partial f}{\partial x} + q \left(\vec{E} + \frac{\vec{p}}{m} \times \vec{B} \right) \frac{\partial f}{\partial p} = 0 \qquad (4.1)$$

where $\vec{x}$ is the position vector of the particle, $\vec{p}$ the momentum, q the charge,

m the mass of the particle, $\vec{E}$ the electric and $\vec{B}$ the magnetic fields acting upon the particle.

The space charge and the current densities can now be obtained by integrating the above distribution function in the momentum space as

$$\rho(\vec{x},\vec{p},t) = q \int f(\vec{x},\vec{p},t)d^3p, \quad \vec{J}(\vec{x},\vec{p},t) = q \int \vec{v}f(\vec{x},\vec{p},t)d^3p \qquad (4.2)$$

where ρ, $\vec{J}$ are the charge and current densities respectively and $\vec{v}$ the velocity of the particle.

4.1   Equations of Motion

The numerical integration of *Vlasov equation* eq.(4.1) along with the *Maxwell equations* in 3D amounts to considerable computational burden. The *Vlasov-Maxwell* system of equations is non linear and in six dimensional phase space becomes impractical to solve as the number of operations to update fields scales as the square of the number of computational particles. An alternative to overcome these difficulties are *Particle Methods*, where the trajectories of the particles can be obtained by numerically integrating linear ordinary differential equations that are characteristic equivalent of *Vlasov equation* and written as

$$m\frac{d\vec{v}}{dt} = \vec{F}, \quad \frac{d\vec{x}}{dt} = \vec{v} \qquad (4.3)$$

where, $\vec{F} = q\vec{E} + q(\vec{v} \times \vec{B})$ is the *Lorentz force* acting on the particle.

Again, based on the type of the problem under study, *Particle Methods* can be subdivided into *Particle-Particle (PP)*, *Particle-Mesh (PM)* methods. The *PP* method is based on the calculation of force exerted on a particle by all other particles in the system. If we have N_p particles then the operation count would be of the order $O(N_p^2)$. For a system consisting of many particles the method would be computationally expensive. To avoid the above problem and make the system computationally feasible and robust we choose *PM* method where the physical system is discretized by a mesh and particles are distributed among these mesh cells. In the first step particle charges are

deposited on the mesh and solved for the new fields along with the boundary conditions. The fields so obtained are then interpolated from mesh to the particle positions and the equations of motion are integrated. Since the number of charged particles in a physical system is far beyond the capability of a computer model, we group a set of charged particles into a macro particle. The charge deposition and the force interpolation scheme when applied over macro particles introduces a discretization error depending on the spatial resolution of mesh or the particle dimension. Also the grid resolution should be smaller than the smallest wavelengths of the physical system. The tradeoff between the accuracy of simulation and the computational time demands a careful selection of the mesh resolution and the number of computational particles.

4.2 Particle-in-Cell Method

The *Particle-in-Cell (PIC)* method as the name suggests defines macro particles inside a physical domain discretized by a mesh. The idea is to solve for the scalar potentials or fields in the entire physical domain using the standard grid based methods such as *Finite Integration Technique (FIT)* with appropriate initial and boundary conditions and interpolate the force exerted by these fields on all particles that lie inside the corresponding mesh cell Fig. 4.1 [23,24]. Once the force on each particle is known, we can integrate the equations of motion given by eq. (4.3) to get the new particle positions and velocities. The charge carried by each macro particle is then assigned to the cell nodes in which it lies and the above procedure is repeated in each time step. The *PIC* scheme can be visualized from the flow chart shown in Fig. 4.2. We shall briefly discuss about different operations that are part of a *PIC* cycle.

4.3 Particle Initialization and Emission

We initialize a *PIC* simulation by defining the particle positions and their initial velocities. As will be described in the Chapter 5, the emission sources are identified and position vectors for particles are defined over the surface. The velocities are initialized by *Maxwell-Boltzmann* distribution function eq. (2.3) or can also be set to zero, depending on whether the initial conditions of particles play a major role in overall particle dynamics of that particular system.
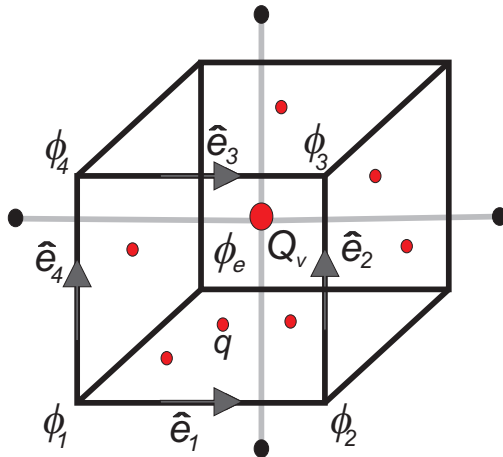
Figure 4.1: A visual representation of the Particle-in-Cell method where the electric potentials ϕ are defined on the primary grid cell nodes. Q_v is a macro particle that is the net charge inside the grid-cell obtained after summing up the charge of all independent macro particles q.

4.4   Charge and Force Interpolation Schemes

The next important step is to find an interpolation scheme, which will assign the charge of all particles inside a cell to the corresponding cell nodes and consequently interpolate the forces on particles due to the fields defined at the cell nodes. There are different schemes to do this depending on the accuracy required and the computational cost. Here we shall discuss the schemes in one dimension for simplicity, which can be easily extended to higher dimensions.

4.4.1   Nearest Grid Point (NGP)

It is a zeroth order weighting scheme where the force is calculated from the nearest grid point from the particle position and the same procedure is applied to the charge deposition Fig. 4.3.

If we consider a one dimensional mesh with corresponding mesh nodes separated by a distance H then the weighting function for the NGP scheme can be written as,
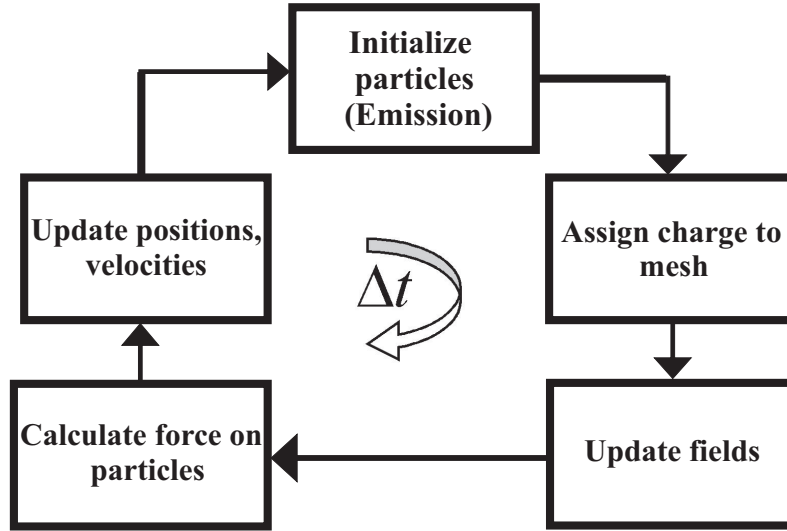
Figure 4.2: A Particle-in-Cell simulation cycle

$$W(x - x_p) = \begin{cases} 1, & |x - x_p| \leq \frac{H}{2} \\ \\ 0, & |x - x_p| > \frac{H}{2} \end{cases} \tag{4.4}$$

where, x_p is the position of the particle and x is the position of the grid point. It can be noted that the weighting function in this case is a delta function. Now the force interpolation function can be written using eq. (4.4) as,

$$\vec{F}(x_p) = q_p \sum_{p=0}^{N_p - 1} W(x - x_p) \vec{E}_p \tag{4.5}$$

where, N_p is the number of grid points, q_p is the charge and $\vec{E}_p$ is the electric field at the grid point. The force due to magnetic field is also calculated in the same way and the total force is obtained by summing up the electric and magnetic force terms. It can be noted from Fig. 4.4(b) that the *NGP* scheme when applied to a periodic system of two equal and opposite charges separated by a distance L, yields force which is discontinuous compared to that of a continuous force variation Fig. 4.4(a). This is obvious since the delta function used in the weighting function varies with a period equal to the grid spacing. This results in a very noisy force interpolation. Similarly
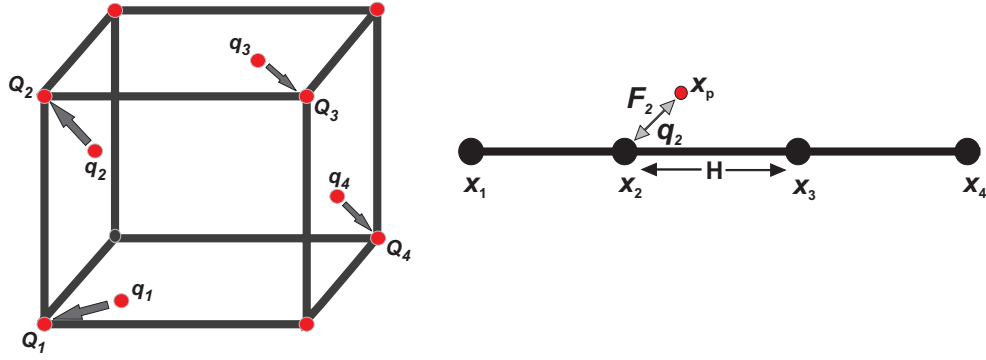
Figure 4.3: The figure illustrates the NGP scheme. The charge of a particle is entirely assigned to the grid point which is nearest to it. An exact opposite operation is done in the case of force interpolation.

the charge deposition over the grid can be written as,

$$\rho(x) = \sum_{p=0}^{N_p-1} \frac{q}{h} W(x - x_p) \tag{4.6}$$

where $\rho(x)$ is the total charge density at a grid point x and q is the charge of the particle located at x_p. The charge interpolation with NGP method can be visualized from Fig. 4.6(a). It can be seen that the charge is assigned to the grid point which lies inside the shape function defined by eq. (4.4).

4.4.2   Cloud in Cell Method (CIC)

The CIC method tries to rectify the noisy interpolation of NGP but at more computational expense [23,25,26]. Considering the same one dimensional mesh as in the case of NGP method and taking two mesh points x and $x+H$ for interpolation, we can write the total CIC force function as a linear combination of individual forces obtained by applying NGP separately to each mesh point. The weighting function can now be written as,

$$W(x - x_p) = \begin{cases} 1 - \dfrac{|x - x_p|}{H}, & |x - x_p| \leq H \\ \\ 0, & \text{otherwise} \end{cases} \tag{4.7}$$
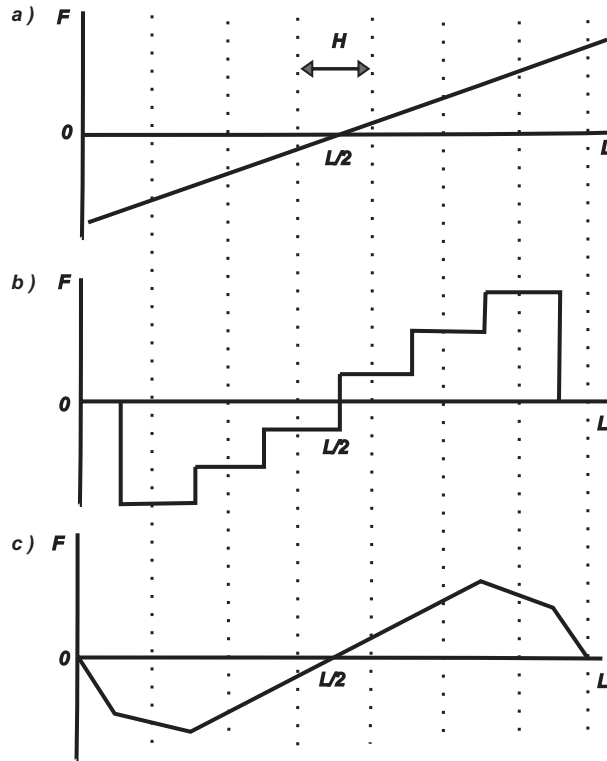
Figure 4.4: (a) The force experienced by a particle in a one dimensional system with equal and opposite charges lying at $x = 0$ and $x = L$. (b) The force interpolation of the same system using NGP approximation which gives rise to a staircase force field. (c) CIC interpolation smoothens the staircase using a triangular weighting function.

The force interpolation for the case of two points mentioned above can now be obtained by taking a linear combination of the force functions derived using the above weighting function at the individual points.

$$\vec{F}(x) = \left[\frac{(x_{p+1} - x)}{h} \right] \vec{E}_p + \left[\frac{(x - x_p)}{h} \right] \vec{E}_{p+1} \qquad (4.8)$$

The above force interpolation plotted in Fig. 4.4(c) varies smoothly. The charge deposition follows the same approach as before but with the weight-
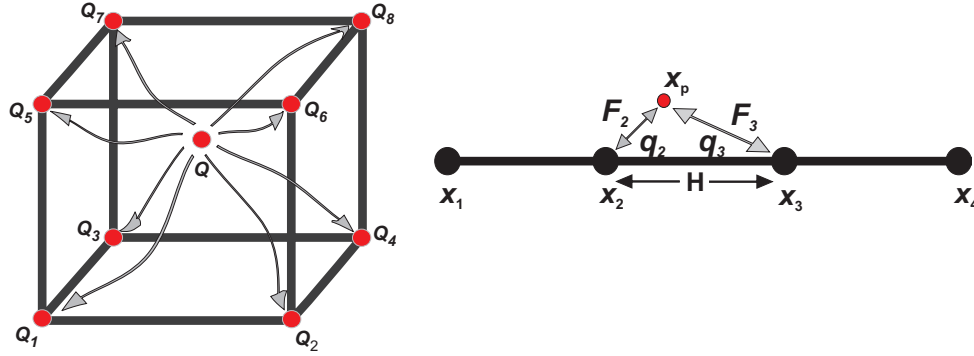
Figure 4.5: A Cloud in Cell charge deposition can be visualized here. The charge Q is assigned to all the nodes of the cell using a weighting function that is a linear combination of the distances of each cell node with that of the particle $Q = \sum_{i=0}^{8} q_i$. The same operation is reversed for the force interpolation.

ing function given by eq. (4.7). It can be seen from Fig. 4.6(b) that the charge weighting now varies smoothly even across the mesh boundary. In three dimensions the scheme can be visualized with Fig. 4.5 where the interpolation is done by the linear combination of weighting functions from each node surrounding the particle.

There are higher order methods like Triangle Shape Cloud (TSC) and cubic splines where the charge is spread among more mesh points adjoining the particle, reducing the noise further. The weighting functions in such methods can be derived following the same approach as in *CIC*, by taking the forces as a linear combination of individual forces from more adjoining nodes. Though such approximations give greater accuracy, it adds to the computational burden. The charge interpolation scheme for a higher order method can be visualized from Fig. 4.6(c).

4.5   Particle Pusher

Once the fields have been calculated over the entire problem domain using the above method, we can proceed to interpolate the fields at the particle positions and calculate the force. After calculating the forces acting on each particle we can solve eq. (4.3) and update the positions and velocities. There are different time integration schemes of which *Euler*, *Runge-Kutta* and *leap-frog* methods are widely used. The *Euler's* method which is a forward time
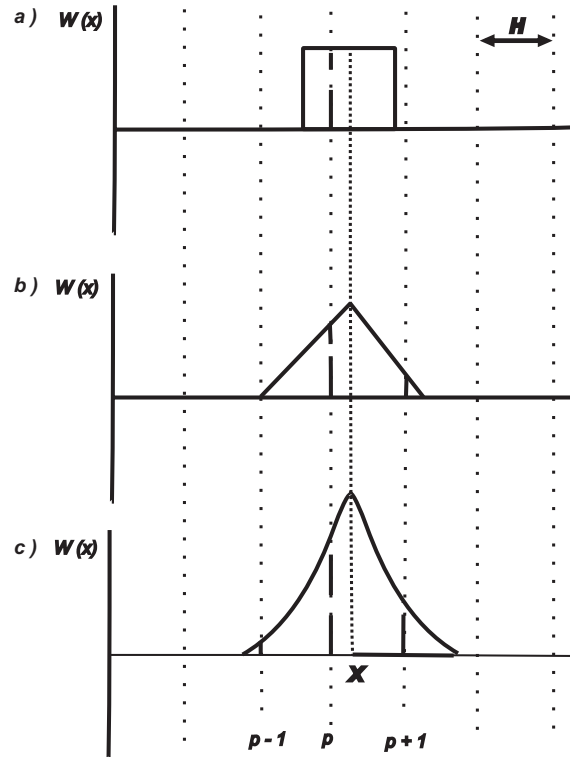
Figure 4.6: (a) The figure gives the *NGP* weighting function as a function of distance along the grid. A particle placed at x is assigned only to the grid point p as the weight for other two grid points is zero. (b) The triangular weighting function in the case of *CIC* enables that the charge be spread among the grid points around it. (c) A second order approximation such as a triangular shape cloud further smoothens the weighting function. Here it distributes the charge among all the nearest grid points.

difference scheme is only first order accurate and is unstable. Comparing the other two methods *leap-frog* method is of second order while the *Runge-Kutta* is fourth order accurate. When compared to *Runge-Kutta* the *leap-frog* scheme requires less storage space as it doesn't have to store intermediate vectors that arise in *Runge-Kutta* method, which makes it faster and economical for a *PIC* simulation. The stability, convergence and the time reversibility makes the leapfrog scheme an appropriate choice for our problem. Taking eq (4.3) and writing the difference equations using *leap-frog* method, we get

$$\frac{\left(v_i^{n+1/2} - v_i^{n-1/2}\right)}{\Delta t} = \frac{F_i^n}{m_i}, \quad \frac{\left(x_i^{n+1} - x_i^n\right)}{\Delta t} = v_i^{n+1/2} \tag{4.9}$$

where F_i^n is the *Lorentz force* on the ith particle due to electric E_i^n and B_i^n magnetic fields and q the charge of the particle. The force can now be written as,

$$F_i^n = qE_i^n + q\left(\frac{(v_i^{n+1/2} + v_i^{n-1/2})}{2} \times B_i^n\right) \tag{4.10}$$

Since the above scheme is time centered and as we cannot determine the velocity and position of the particle at the same instance of time, we push back the velocity by half time step $v(t - \Delta t/2)$ using the force calculated at time $t = 0$. The method can be visualized from Fig. 4.7.
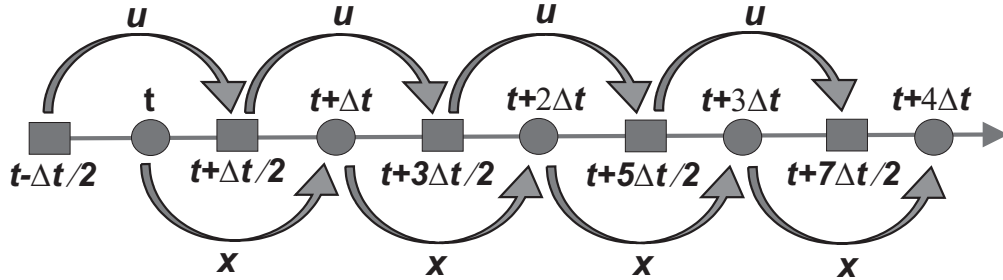

Figure 4.7: Time centered *leap-frog* method where the velocities and positions are calculated interchangeably between two consecutive forward and backward time values. The initialization requires making one backward Euler push of velocity at time $t = 0$.

The *Boris algorithm* for *leap-frog* time stepping of the *Lorentz force* is the most efficient and stable. This algorithm applies half energy change due to the electric field term, then one rotation due to the magnetic field that doesn't contribute to an energy change, and finally another half of the energy change to resolve the *Lorentz equation*. The force equation can be divided by considering the electric and magnetic forces separately. Taking two auxiliary

velocity terms v_1 and v_2 we can write the first electric acceleration term as

$$v_1 = v_i^{t-\Delta t/2} + \frac{qE_i^t \Delta t}{2m} \qquad (4.11)$$

then v_2 can be calculated from the magnetic rotation as

$$v_2 = v_1 + \left[(v_1 + v_2) \times \frac{qB_i^t \Delta t}{2m} \right] \qquad (4.12)$$

once we have the second velocity term we can calculate the velocity at the instance $t + \Delta t/2$ with another electric acceleration as

$$v_i^{t+\Delta t/2} = v_2 + \frac{qE_i^t \Delta t}{2m} \qquad (4.13)$$

Where the superscripts have been indexed in time for clarity of time stepping scheme. After we have the velocity at $t+\Delta t/2$, it can be substituted into eq. (4.9) to get the new positions. The above discussed methods together form the complete *PIC* simulation cycle.

The *Particle-in-Cell* method finds its applications in the simulation of plasma and vacuum electron devices. The hybrid *PIC-Monte Carlo* methods are used for the simulation of collisional plasmas [27,28,29].

Chapter 5

Geometric Modeling

5.1 Surface Mesh Generation

Surface mesh generation is the process of discretizing the surface of an emitter by a set of triangular elements called emission samples. These emission samples enable us to calculate the current and charge by interpolating the fields that are solved on an external grid. It has to be noted that an external grid is the discretization of the entire problem space, on the other hand a surface mesh is discretization of an emitter surface for defining initial positions of macro particles. The basic description of an emitter comes from a 3D geometric modeling tool such as *ACIS*, which provides for curve, surface and solid modeling of objects. The elements defining an object are a set of triangles in 2D and tetrahedra in 3D. The faces of such non-overlapping elements whose normals direct away from the object form a *Surface Mesh*. The spatial information of these elements can be obtained in the form of a *Standard ACIS Text (SAT)* file. The barycenters of the elements so obtained will be the initial positions of the macro particles, over which the grid variables are interpolated. The dimensions of surface elements are in general far bigger than the external grid. Which means that the discretization of external grid is finer than the surface mesh resulting in an inaccurate interpolation of fields on emitter.

It is evident from the above discussion that the emission model requires re-triangulation of the surface of an emitter, so that the dimensions of the surface elements are comparable to that of the external grid. The process of connecting a set of points in space enclosed by a convex hull, resulting in a unique set of triangles in 2D and tetrahedra in 3D is often referred to as *Delaunay Triangulation (DT)* [30]. A convex hull is a domain that encloses

all the points that are to be triangulated. In the case of 2D a convex hull is a polygon and in 3D it is a polyhedra. The *Delaunay triangulation* fulfills all conditions of geometrical modeling while retaining the topology of an object. We shall discuss the main properties of a *Delaunay triangulation* for a planar 2D surface and extend it to 3D using constraints. The input for triangulation is a finite set of distinct points or lines in space called vertices or edges respectively. This space is further divided into small sub-regions that enable the vertices or edges to be connected to each other with ease, retaining the exact topology. Once these small regions are triangulated the boundary vertices or edges from one sub region are connected with other sub-regions to complete the triangulation of the entire object. The two basic properties of *Delaunay triangulation*, which are essential for connecting points in space are discussed in next two sections.

5.2   Circum-Circle Criterion

A triangle T with vertices $V(V_1, V_2, V_3)$ is said to fulfil *Delaunay* of a set of points S if and only if no other point of S lie internal to the circum-circle defined by the points (V_1, V_2, V_3). In Fig. 5.1(a) we have three triangles T_1, T_2, T_3 with corresponding circum-circles C_1, C_2, C_3 obtained by connecting some arbitrarily distributed points in space. As we can see the triangulation is not *Delaunay* since the circum-circle C_3 of the triangle T_3 includes another point P of S. The result is that the triangulation is not unique. The triangle T_3 is corrected as shown in Fig. 5.1(b) which now satisfies the circum-circle criteria of DT.

5.3   Angle Criterion

The diagonal that splits the quadrilateral into two triangles T_1, T_2 should be such that it maximizes the minimum internal angles. In Fig. 5.2(a) we have the triangles T_1, T_2 with internal angles $\theta_1, \theta_2, \theta_3, \theta_4$. The internal angles have been maximized by re-arranging the diagonal of the quadrilateral as seen in Fig. 5.2(b). This operation results in triangles with better aspect ratio, which is defined as the ratio of the radii of inscribing to the circumscribing circle in 2D and that of the sphere in the case of 3D. Alternately it can also be defined as the ratio of the longest edge to the shortest edge of a triangle or tetrahedra.
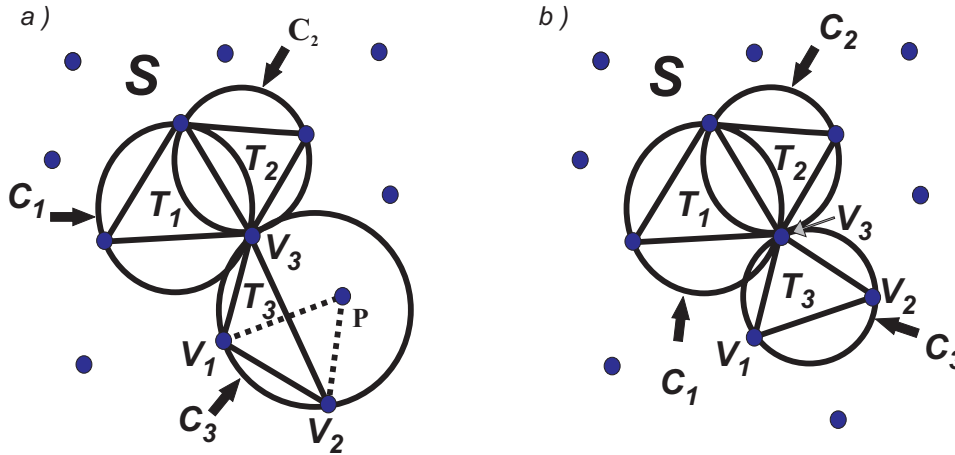
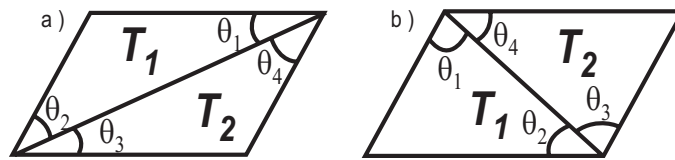Figure 5.1: (a) An illegal *Delaunay triangulation*. (b) A corrected triangulation with circum-circle C_3.

Figure 5.2: (a) An edge between triangles T_1, T_2 with minimum internal angles. (b) Maximizing the minimum angles with an edge flip.

5.4   Sub-Triangulation

Now we can extend the conditions mentioned in previous sections to 3D where the points in three-dimensional space sharing the same facet are connected to form a tetrahedra. But it is more complicated than 2D since the angle criterion is no longer valid and the aspect ratio is normalized with recursive sub-triangulation. As stated in the beginning, we need more sample points for every boundary external grid cell to keep the discretization and interpolation errors to minimum. To fulfill this criterion the first condition is to ensure that the largest edge of the triangle or tetrahedra is smaller than the smallest edge of the external grid and the second condition is to keep the aspect ration close to one, so as to have a uniform surface mesh. The ideal condition is when the aspect ratio is one, where all the edges are of equal length and such a triangulation has all the sample points uniformly distributed over the surface. However, *Delaunay triangulation* cannot guar-
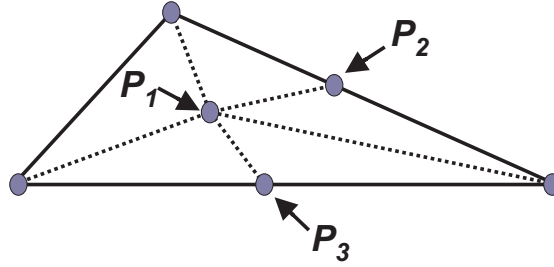
Figure 5.3: Points P_1, P_2, P_3 inserted to split the original triangulation. The dotted lines denote the new edges formed by new vertices.

antee the desired aspect ratios for a surface mesh and hence we have to apply a few constraints while triangulating the surface. Here we discuss the application of constraints in a simple 2D case, which are then extended to 3D but with increased complexity. The two common methods used in *Constrained Delaunay Triangulation (CDT)* are

1. *Insertion of Points :* In this method a point or vertex is added to a triangle to which the constraint is to be applied. The splitting of a triangle further into three more triangles automatically satisfies the properties of DT, which is already fulfilled by the parent triangle. For a triangle whose aspect ratio is poor, the point is usually inserted at the center of the longest edge and the sub-triangles are checked for the aspect ratio after splitting. The process is repeated iteratively until the aspect ratio and the edge lengths fall within the specified limits Fig. 5.3.

2. *Insertion of Edges :* Insertion of edges is commonly used in triangulation around sharp edges or critically curved surfaces. Triangulation in such regions has poor aspect ratio and further insertion of points and sub-triangulation might be computationally very expensive and may also result in an over populated set of samples. The solution can be found in re-adjusting the edges according to the angle criterion or rejecting the edges and reconnecting the points to eliminate skewed triangles. If we desire to have an edge between two vertices or points, the first step is to remove all other edges that intersect the desired edge Fig. 5.4(a) and reconnect all the points accordingly to have the new triangulation Fig. 5.4(b).
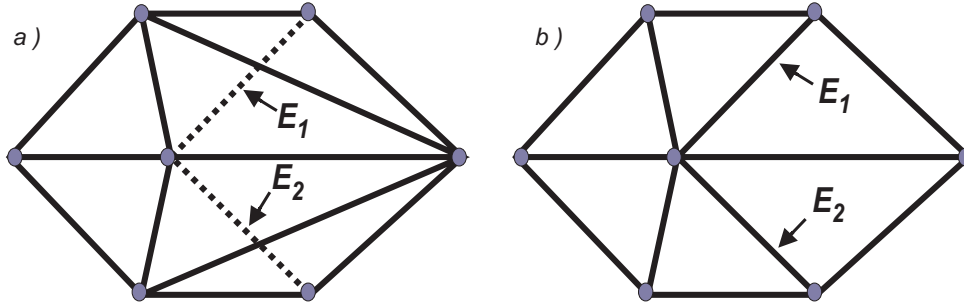
Figure 5.4: (a) E_1, E_2 are the edges to be inserted. (b) The edges which intersect with E_1, E_2 are deleted and the new edges come in their place.

5.5 Uniform and Adaptive Sampling

In most of the cases where we have no critically curved emission surfaces such as the sphere shown in Fig. 5.5(a), a uniform surface mesh Fig. 5.5(b) is better suited as there is no charge concentration over any particular region of the emitter surface and does not require curvature specific sampling. But in the case of emitters with fine tips or sharp edges which carry more charge, we can refine the surface mesh locally to get a reasonable charge per particle ratio and thus avoid interpolation errors Fig. 5.6. Especially in modeling *Field Emitter Arrays* where the charge emission is from many fine cathode tips etched on a semi-conducting substrate, local refinement of surface mesh is better suited.

5.6 Implementation

For the implementation of *CDT* we use the *Gnu Triangulated Surface (GTS)* library [31]. It is an open source object-oriented code for 3D surface meshes. It also provides the flexibility to operate on many topological attributes such as points, vertices, line segments, edges, faces, triangles or any general geometrical shape. The library includes options such as boolean intersection between surfaces, increasing or decreasing the number of edges and vertices, vertex split or an edge collapse and other geometric modeling operations. In the case of the emission problem we have two approaches to generate surface mesh Fig. 5.7, one that is performed based on all boundary cells of the external grid which intersect the emitter and is referred as cell based emission sampling and another which takes uniform samples over an entire emission object, referred as shape based emission sampling.
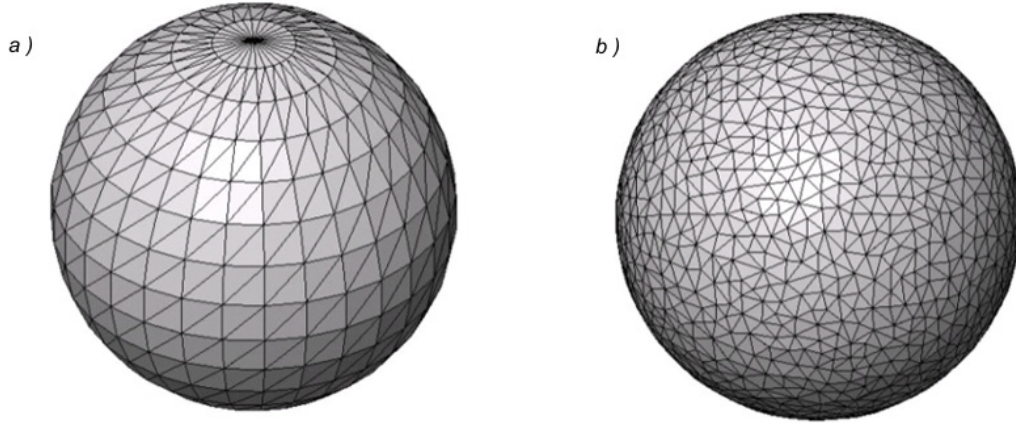
Figure 5.5: (a) Surface triangles from a basic geometrical kernel such as *ACIS*. The triangulation in this case has long edges at the vortex points and results in poor charge sampling. (b) Uniform distribution of samples after *Constrained Delaunay Triangulation*. The edges that are skewed are split based on a specified aspect ratio.

5.6.1   Cell Based Emission Samples

In this procedure we scan all the cells of external grid and identify the cells which have intersection with the emitter. First we define a bounding box which contains the emitter. After that we traverse through each cell and pass the cell coordinates and other constraints such as accuracy and curvature correction to the *GTS* sampling function which in turn returns position of the samples, normal vectors to the samples and the corresponding sample areas. Each emission cell is now termed as a booth, where all the sample information is stored.

5.6.2   Shape Based Emission Samples

As the name suggests, the samples are taken from the whole shape of an emitter by supplying the *GTS* with the accuracy and the maximum number of samples that we require. Later each of the samples so obtained are assigned to the emission booths by locating the cells in which the samples are bound. The sample information is stored in the corresponding booth cells as in the previous method.

Once the booth array is acquired with all the information about emission samples, we can initialize the positions, charge, current and velocities of the macro particles for a *PIC* simulation.
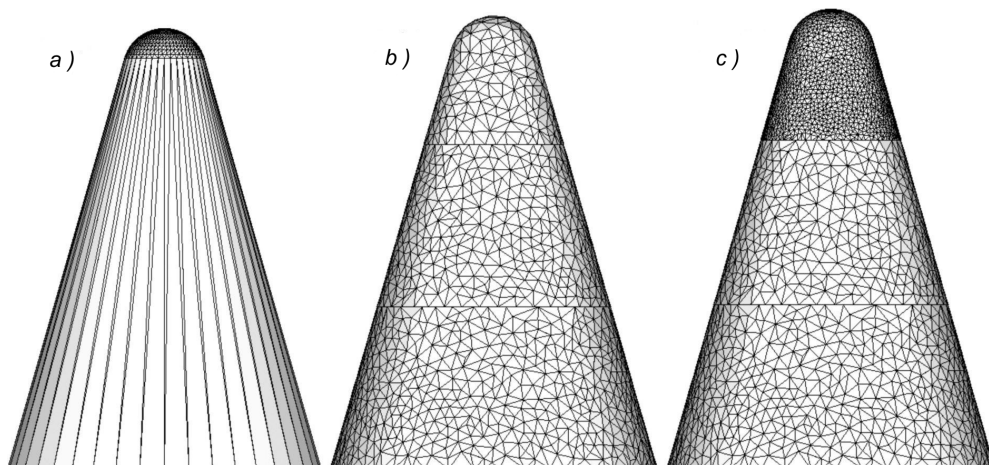
Figure 5.6: (a) Surface triangles from geometrical kernel *ACIS*. (b) Sub-triangulation using *CDT*. (c) Local surface mesh refinement required for emitters with fine tips. After obtaining uniform sampling of surface triangles, a new aspect ratio is specified for triangles lying near the tips. These triangles are further refined using *CDT*.
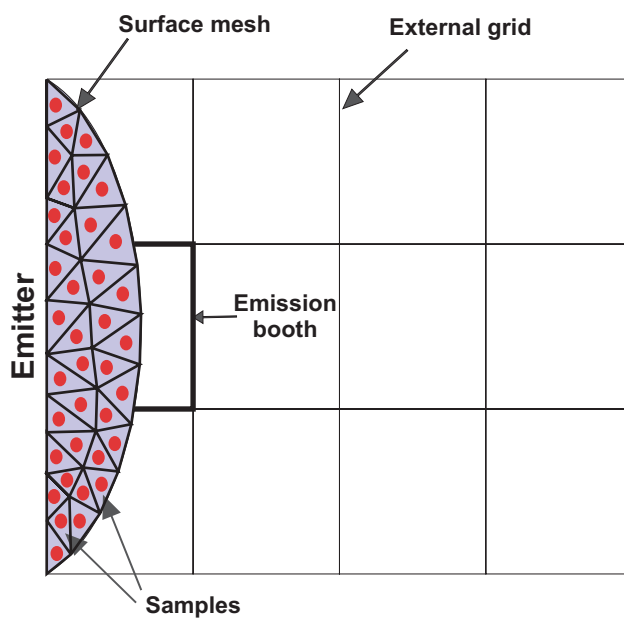

Figure 5.7: The figure depicts the discretization of emission surface and generation of samples for each emission booth.

Chapter 6

The Space Charge Limited Emission

In chapter 2 various primary emission mechanisms have been discussed, where the electron emission was mainly dependent on the external forces. But all practical electron devices have an upper limit to the current that they can supply. This limit on the current from an emitter can be defined by the conditions under which the device is operated. In further sections of this chapter, we discuss such conditions under which the current is limited and derive the governing equations and finally present the numerical methods to implement them in the emission model.

6.1 I-V Characteristics of a Diode

The current-voltage or the *I-V* characteristics of a diode is shown schematically in Fig.6.1. It can be observed from the *I-V* plot that the anode current is classified into different regions as a function of the anode voltage. The electrons emitted from a cathode have different energies defined by the *Fermi-Dirac distribution function*. The electrons, which come with greater energy move faster and reach the anode while the low energy electrons are slower. If the emission from cathode is continuous, the density of the electrons that are slow and lagging behind increases for a given anode potential. This eventual increase of low energy electrons results in an electron cloud or space charge around the cathode, which in turn acts as a negative grid neutralizing the anode potential. When the potential of this electron cloud or virtual cathode equals that of the anode potential, emission ceases. This condition of limiting the current by the formation of a *virtual cathode* or *space charge* is known as *Space Charge Limited (SCL)* emission [32,33]. This phenomenon is
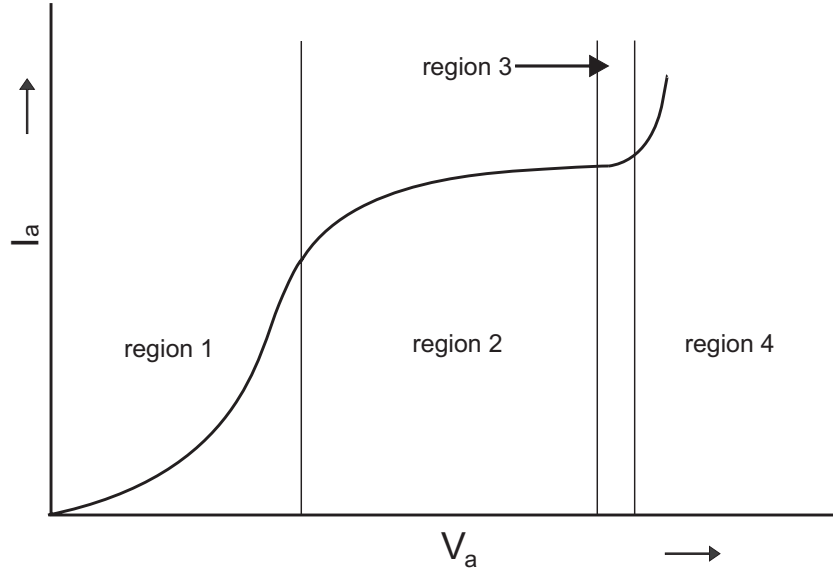
Figure 6.1: A schematic of current-voltage characteristics of a diode. It can be seen that the characteristic curve can be analyzed by dividing it into 4 regions of operation based on the anode potential. At low anode voltages the space charge and temperature of the cathode govern the anode current but at very high voltages the diode enters saturation

more pronounced at low anode voltages as the electrons that are emitted see low accelerating fields and bunch up around the cathode. When the anode potential is increased the current will start rising once again and the space charge limit transfers to a higher current limit.

The region 1 in Fig. 6.1 depicts the operation of a diode, where the anode current increases accordingly with the anode voltage, and for a fixed anode potential the current reaches a maximum value defined by the space charge limit. The current in a diode as a function of saturation current density can be written as,

$$|\mathbf{J}| = |\mathbf{J_0}|e^{V_{min}/kT} \tag{6.1}$$

where V is the anode potential with respect to cathode and V_{min} is the potential of space charge cloud and $|\mathbf{J_0}| = A_0 e^{-\phi/kT}$ is the saturation current. For given input parameters the *space charge limited* current at different space charge cloud potentials can be plotted as in Fig. 6.2 by solving eq. (6.1). In
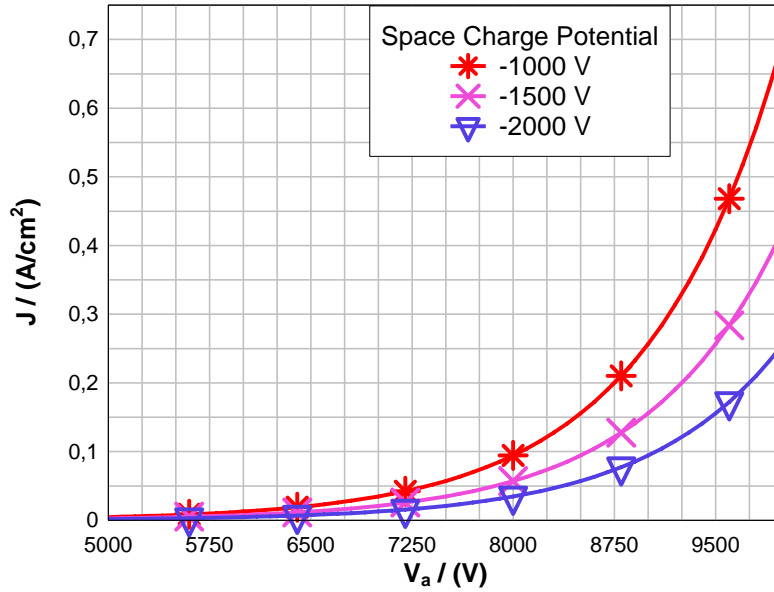
Figure 6.2: The plot taken between anode current and anode potential for different space charge limits. It can be observed that for a given anode potential, the total current that can be drawn is limited by the space charge between the electrodes. If the anode potential is increased further, it would result in a high saturation current and space charge effects cease. With more space charge, the saturation current limit only comes at relatively at higher voltages.

reality the emission will not cease completely but oscillates around a certain minimum value.

6.2   Current Limited by Temperature

In the region 2 of Fig. 6.1 we see that the current is almost independent of the anode potential and only varies as a function of the cathode temperature. Electron devices usually operating with thermionic cathodes fall into this region of operation where the current is limited by the amount of temperature to which the cathode can be raised. This dependence of current on the temperature is defined as *Temperature Limited emission.*

It can be observed from Fig. 6.3(a) that the current steadily increases with temperature for materials of different work function, and reaches a maximum. Further increase in the temperature will not give rise to a corresponding in-
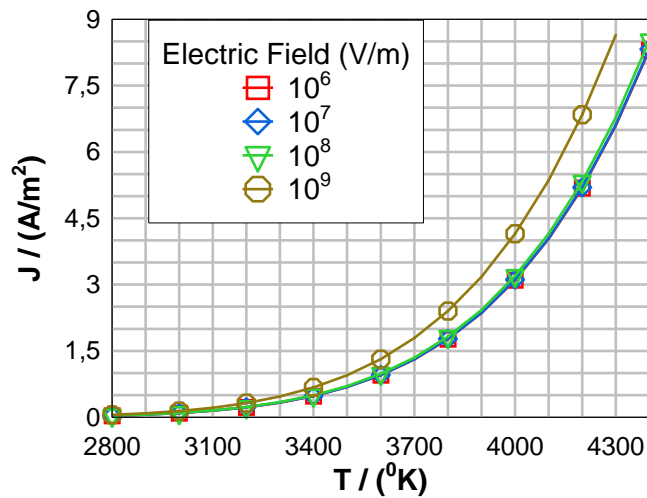
(a)
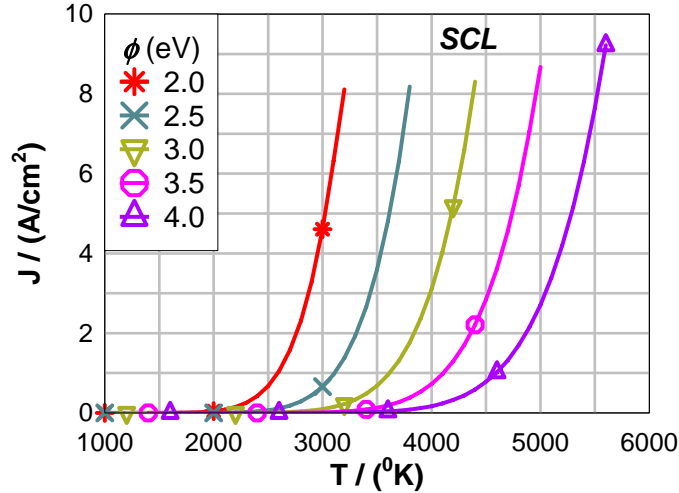
(b)

Figure 6.3: (a) The curves show the current density as a function of temperature. A higher temperature is required to draw current from a material of larger work function. But however the current in all cases varies to a certain limit beyond which the emission is dependent on space charge. It has to be noted that even if a large current is present at the cathode surface due to thermal heating, if an appropriate external field is not present to draw the electrons away, it would result in build up of space charge, which would force the charge back into the cathode. (b) In this curve the *Schottky effect* can be visualized. For a given material and work function the current is more when the external field is increased. It was an obvious result from the expression derived in Chapter 2. If the fields are further increased, it would result in a huge current and the field emission relations for current come into play.

crease in the current and the limit is said to have reached. Any attempt to increase temperature will only result in destroying the cathode, referred as thermal runaway. A high operating temperature also means less life span of the cathode. The current limited by temperature is given by the *Richardson-Dushman* eq. (2.6).

The region 3 of Fig. 6.1 shows an increase in the current for a small increment in the anode voltage. This phenomena is observed in thermionic cathodes. When the external field is of the order of many thousand volts per meter, more electrons can be drawn away from the cathode even after the cutoff set by temperature limited emission is reached. This is known as Schottky emission, defined by eq. (2.7).

In the region 4, the current increases exponentially with respect to anode voltage. This is known as field emission given by the *Fowler-Nordheim* eq. (2.14). Here the electric field due to anode voltage is so high that all the electrons which are emitted are collected by the anode and the diode is set to have reached saturation.

6.3   Current Limited by Space Charge

In eq. (6.1) we assumed the current to be dependent on the space charge potential V_{min}. The latter however depends on the emitted current. The self-consistent solution of this problem was first given by *Child* [34]. Let us consider a planar diode as shown in Fig. 6.4, with anode and cathode plates extending infinitely in the $x-y$ plane and separated by a distance d along the z axis. The anode is maintained at a potential V with respect to the cathode.

If we assume no charge inside the anode and cathode gap, the potential distribution varies linearly in the space separating the two electrodes. The saturation current density $\mathbf{J_0}$ in a diode can be obtained using eq. (2.6), substituting it in eq. (6.1) we can calculate the space charge limited current for a given potential minimum V_{min}. After obtaining the current, potential distribution inside the diode can be calculated by substituting it back into the *Poisson's equation*. The potential distribution inside the diode, assuming various values of potential minimum is give in Fig. 6.5. If we increase the charge further by increasing the value of potential minimum, the curve dips with more non-linearity near to the cathode indicating the formation of a space charge cloud or virtual cathode. If the charge is increased further, the potential of the space charge around the cathode increases. When the
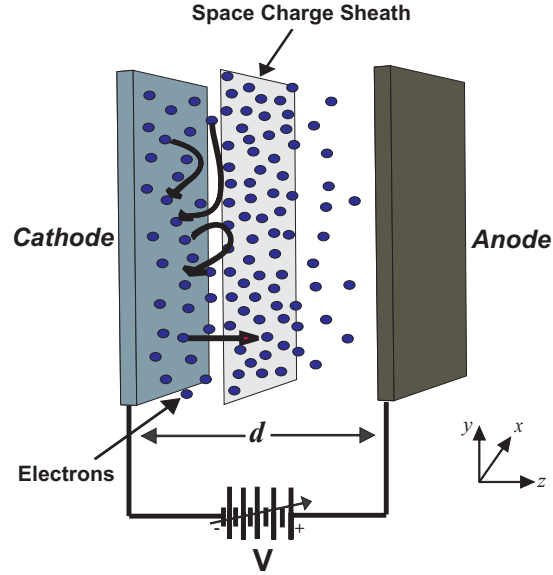
Figure 6.4: A picture depicting space charge effects on cathode emission. It can be seen from the figure that electrons of low energy will return back into cathode with a very short life-time and those with higher energy can manage to get across the space charge sheath.

potential minimum increases further, the curve crosses into the negative axis indicating that the virtual cathode, formed by the space charge sheath, has more repelling field on the emitting electrons than the accelerating field of the anode. At this moment the space charge limit is said to have reached.

The first boundary condition for the calculation of space charge limited current is that the total electric field on the surface of cathode be equal to zero $|\mathbf{E_z}| = 0$. Now the potential distribution in the anode-cathode gap can be written by the *Poisson's equation*[35], as

$$\frac{d^2V}{dz^2} = -\frac{\rho}{\varepsilon} \tag{6.2}$$

where V and ρ are the potential and charge density respectively, and ε is the permittivity of the medium. The reduction of the space charge problem to 1D stems from the mathematical hindrance in solving the *Poisson's equation* in 3D along with the equations of motion of electrons. For arbitrary anode and cathode geometries it is impossible to obtain a solution in 3D except for the numerical methods. The current and charge density are related as
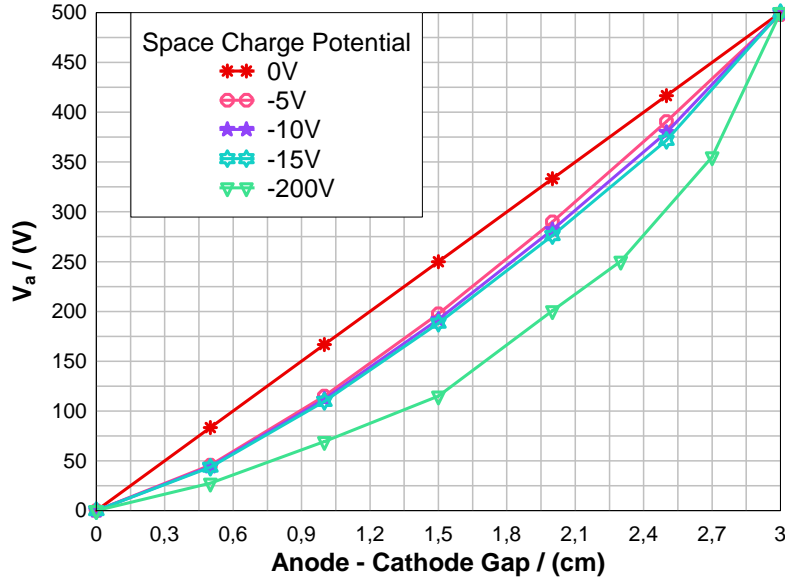
Figure 6.5: Potential plot of a parallel plate electrode with anode plate at 500V with respect to cathode and separated by a distance of 3cm. It can be seen that more charge between the plates defined by a larger potential minimum would neutralizes the anode potential. The curve crosses the abscissa when space charge potential reaches the anode potentials.

$$|\mathbf{J}| = \rho \cdot |\mathbf{u}| \tag{6.3}$$

where $\mathbf{J}$ and $\mathbf{u}$ are the current density and velocity of the electron respectively. Substituting the above equation in eq. (6.2) we get

$$\frac{d^2V}{dz^2} = -\frac{|\mathbf{J}|}{\varepsilon|\mathbf{u}|} \tag{6.4}$$

The conservation of energy can now be included into the above equation by considering the fact that the potential energy is totally converted into the kinetic energy of the electron, which can be written as

$$\frac{m|\mathbf{u}|^2}{2} = e(V_a - V_c) \tag{6.5}$$

where $V_a = V$ is the anode potential,$V_c = 0$ is the potential at the cathode and e, m are the charge and mass of the electron respectively. Next we Calculate $\mathbf{u}$ from the above equation and substitute in eq. (6.4). Multiplying it

then by $2dV/dz$ on both sides and integrating, we get

$$\left(\frac{dV}{dz}\right)^2 = \frac{4|\mathbf{J}|}{\varepsilon}\sqrt{\frac{V}{2\eta}} + c_1 \tag{6.6}$$

where η is the charge to mass ratio of electron and c_1 is the constant of integration. Now imposing the boundary condition that at the cathode $V_c = 0$ and also the condition that $|\mathbf{E_z}| = dV/dz = 0$, the constant is found to be equal to zero. The eq. (6.6) can now be written as,

$$\frac{dV}{dz} = 2\sqrt{\frac{|\mathbf{J}|}{\varepsilon}}\left(\frac{V}{2\eta}\right)^{1/4} \tag{6.7}$$

Integrating the above equation yields,

$$\frac{4V^{3/4}}{3} = 2\sqrt{\frac{|\mathbf{J}|}{\varepsilon}}\left(\frac{1}{2\eta}\right)z + c_2 \tag{6.8}$$

Again taking the boundary conditions $V_c = 0$ at $z = 0$ and $V_a = V$ at $z = d$, the second constant of integration c_2 is also found to be equal to zero. The above equation can then be re-written as,

$$|\mathbf{J}| = \frac{4\varepsilon}{9}\sqrt{2\eta}\frac{V^{3/2}}{z^2} \tag{6.9}$$

which is the *Child-Langmuir equation* for the current per unit surface area per unit time, in a space charge limited diode. The potential in the *anode-cathode gap* with the space charge current included can be easily obtained by re-writing the eq. (6.9). In a physical device, cathodes have a finite dimension unlike the infinite plane as assumed in the beginning of the above derivation. If A is the area of the cathode, the total current can be written as $I = PV^{3/2}$, where $P = 4\varepsilon\sqrt{2\eta}/9z^2$ is the *perveance* and depends only on the diode geometry.

The above derivation has many approximations that have to be modified to simulate practical problems. The assumption of the diode as an infinitely extending parallel plates was made to avoid the non-linear distribution of the fields at the edges. Similarly, it is assumed that the electric field and the

initial velocities of electrons tend to zero on the surface of the cathode. In reality the space charge cloud is only high enough to reduce the fields on the cathode to a minimum, but there would still be some electric field on the cathode. Also the electrons come out of the emitter with finite initial velocities due to the external fields and temperature of the cathode. The electrons that have sufficiently high energy can go across the potential minimum of the space charge cloud and reach the anode, and the electrons with less energy return back to the cathode. When the anode voltage is increased, the potential minimum moves towards the vicinity of the cathode surface, resulting in greater number of electrons to have energy sufficient to reach anode. And when the potential minimum is just about the cathode surface given by the condition $dV/dz = 0$, the space charge limit ceases and the anode draws all the electrons emitted by the cathode as given by eq. (6.1). With the above arguments the anode-cathode gap can now be divided into two regions, one that exists between cathode surface and the potential minimum V_{min} and another between the potential minimum and the anode. The current can now be written as,

$$|\mathbf{J}| = \rho \int_0^\infty |\mathbf{u}| d|\mathbf{u}| \qquad (6.10)$$

If the initial velocities of the electrons are assumed to vary between the limits $|\mathbf{u}|$ and $|u| + d|\mathbf{u}|$, we can write the velocities according to the *Maxwell-Boltzmann* distribution given by eq. (2.3). Substituting the same into the above equation and integrating by applying the boundary conditions of the two regions mentioned above, the new space charge limited current density with initial velocity correction can be obtained.

$$|\mathbf{J}| = \frac{2.336 \times 10^{-6}(V - V_{min})^{3/2}}{(z - z_{min})^2} \left(1 + \frac{2.66}{\sqrt{\chi}}\right) \qquad (6.11)$$

where z_{min} is the position of the potential minimum, T is the temperature of cathode in degrees Kelvin and $\chi = e(V - V_{min})/kT = 11,605(V - V_{min})/T$.

The values of the potential minimum and its position can be calculated for a given input of cathode temperature, saturation current and anode voltage. It has to be noted that the above equation results in a higher current density than that given by eq. (6.9), which was an over estimate of the space charge limit. A similar expression for space charge limited current can be calculated for electrons emitted with near ultra relativistic velocities, which can be the case in high field emission devices.

6.4 Current in Spherical and Cylindrical Diodes

Until now we only made necessary corrections to the original *Child's law* current assuming planar geometries. But in the actual practice there are hardly any applications which use planar emitters. In many emitter design problems it has been found that the current per unit surface area of a cathode is often less when compared to the system requirements. Since the emitter surfaces cannot stretch to large dimensions owing to the constraints set by the size of a device, it is a common practice to have a maximum effective surface area of the emitter within the same physical space to generate more current density. A practical alternative to achieve the above objectives is to employ a circular cylindrical [36] or a spherical cathode [37]. This not only increases the effective area of emission but also ensures an easy beam focusing mechanism for convex emitter surfaces.

The assumptions we made for a planar diode are no longer valid for the diodes of either circular or spherical symmetry. The *Poisson's equation* is taken in cylindrical coordinates eq. (6.12) assuming the potential variation only in the radial direction and constant along the other directions.

$$\frac{1}{r}\frac{\partial}{\partial r}\left(r\frac{\partial V}{\partial r}\right) = -\frac{\rho}{\varepsilon_0} \tag{6.12}$$

Using the same boundary conditions as in the planar diode, the space charge limited current for a circular cylindrical diode can be derived as,

$$|\mathbf{J}| = \frac{2.336 \times 10^{-6} V^{3/2}}{r_a r_c \beta^2} \tag{6.13}$$

where, r_a and r_c are the anode and cathode radii respectively and $\beta = \Omega - 2\Omega^2/5 + 11\Omega^3/120 - 47\Omega^4/3300 + \ldots$, with $\Omega = \ln(r_a/r_c)$.

Similarly taking the *Poisson's equation* in spherical coordinates eq. (6.14), with potential variation only along the radial direction and constant along θ and ϕ axis, we have

$$\frac{1}{r^2}\frac{\partial}{\partial r}\left(r^2\frac{\partial V}{\partial r}\right) = -\frac{\rho}{\varepsilon_0} \tag{6.14}$$

The space charge limited current derived by Langmuir and Blodgett for a

spherical diode is [37]

$$|\mathbf{J}| = \frac{2.336 \times 10^{-6} V^{3/2}}{\alpha^2} \tag{6.15}$$

where $\alpha = \Omega - 0.3\Omega^2 + 0,075\Omega^3 - 0.001432\Omega^4 + 0.002161\Omega^5 \ldots$ and Ω holds the same relation as in cylindrical case, but now for the radii of the respective spherical electrodes.

It should be noted that in the above corrections to the current, the *three-halves power law* holds irrespective of the diode geometry or initial conditions. The correction only comes in the *perveance* factor, which is dependent on the shape of the emitter.

6.5   Numerical Methods

The calculation of space charge limited current using analytical methods is again restricted to only few well-defined geometrical structures. The emitter geometries that are used in practice come in very arbitrary shapes and even though the emitter may have a particular symmetry, the other electrodes that are used to focus the beam may not confer to the same rule. All this sums up to a situation where the charge and potential distribution between the electrodes can no longer be defined with an analytical equation. The conformal field solutions discussed in Chapter 3 and a well-defined geometric model for emission can produce numerical solutions to the space charge limited problem with good accuracy. Here we shall consider two models that are implemented in this work and validate them for different diode geometries [38].

6.5.1   Virtual Cathode Method

The equations for current density derived in previous sections are useful only in one dimensional simulations. But for emitters of arbitrary shapes, *Child's law* current is impossible to derive without few approximations [39,40]. If the anode and cathode are concentric and have same axis of symmetry, the *Langmuir-Blodgett* corrections could have been applied to get an analytical solution. A solution to the problem of arbitrary emission geometries can be found by transforming the 3D emission surface into a set of 1D diode structures as shown in Fig. 6.6 This transformation requires finding a surface
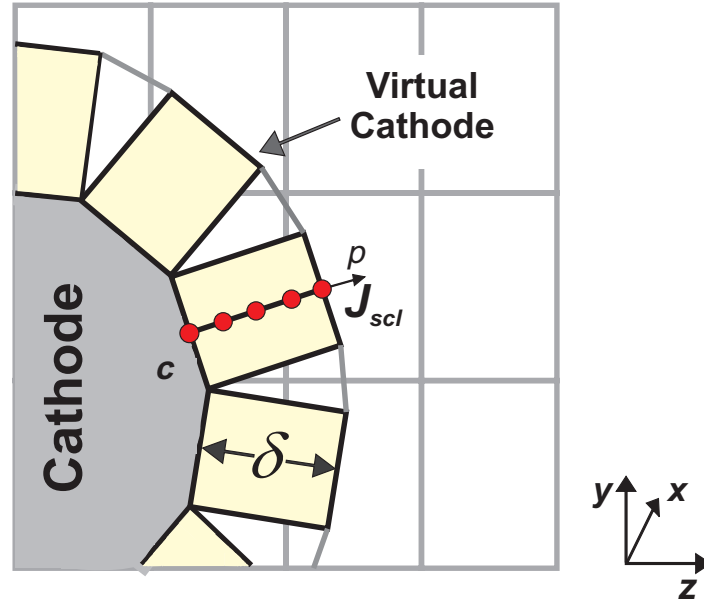
Figure 6.6: The figure depicts a 2D view of the *Virtual Cathode* method for the calculation of space charge limited current. It can be seen that the emission samples are translated along the normal through a distance δ, which is generally a couple of grid cells away from the cathode. The space between the parallel plates is filled with a uniform charge distribution after calculating the current J_{scl} using *Child's law*. The 1D approximation is applied over the whole emitter to calculate *SCL* current.

around the cathode inside which there is an almost linear variation of potential under no space charge conditions. This region can then be considered as a parallel plate diode obeying the 1D *Child's law*.

Referring back to Chapter 5 where the generation of a surface grid over an emitter was presented, it has been shown that the surface of an emitter is descretized with a set of sample elements over which current is calculated. If we consider a sample surface of same dimensions in the vicinity of cathode along the normal, both the sample surfaces can be considered as two plane parallel electrodes. The accuracy of the scheme depends on carefully selecting the distance at which the virtual cathode is to be located. This can also be done iteratively until we get an appropriate gap width δ. The procedure transforms a 3D problem into a set of 1D problems for the application of *Child's law*. If we can calculate the potentials on the surface of each of the samples of virtual cathode and assume it to be constant, we can apply

eq. (6.9) to the resulting 1D diode structure and find the *Child-Langmuir* current. This current will now be emitted from the virtual cathode.

6.5.2 Equivalent Gap Charge

The charge density inside a diode goes to infinity as we approach the surface of the cathode $\rho \propto -1/r$, where r is the distance between the point of observation and cathode. This condition cannot be modeled numerically. To avoid this problem we assume a constant charge density inside the gap separating the virtual and the actual cathode. We have already seen that using *CFIT* it is possible to compute the fields on geometries of any shape with good accuracy, and it only requires interpolation of these fields on the virtual cathode. In the first step we solve for the fields inside the whole diode. Next we use the Cloud in Cell interpolation to find the potentials or fields at any point inside a grid cell. After locating the position of the virtual cathode, the potential or fields on that surface is a weighted interpolation of all the potentials lying on the corresponding grid nodes. The space charge limited current can then be calculated as described in the previous section. Now we have to fill up the gap between the real cathode and the virtual cathode with an equivalent charge that satisfy the boundary conditions of the diode. Leaving the gap open without any charge will render the model unphysical. Now if $\phi(d)$ and $\phi(c)$ are the potentials at the virtual cathode and the actual cathode as shown in the Fig. 6.7, the potential distribution anywhere inside the gap can be written as,

$$\phi(z) = \phi(c) + [\phi(d) - \phi(c)] \left(\frac{z}{d}\right)^{4/3} \qquad (6.16)$$

where d is the position of the virtual cathode. Differentiating the above equation along the cathode gap gives

$$\frac{d\phi(z)}{dz} = \frac{4}{3}[\phi(d) - \phi(c)]\frac{z^{1/3}}{d^{4/3}} \qquad (6.17)$$

By applying the boundary condition for the electric field at $z = d$, we have

$$\frac{d\phi(z)}{dz} = \tilde{\mathbf{E}}_{\mathbf{n}}(\mathbf{d}) \qquad (6.18)$$

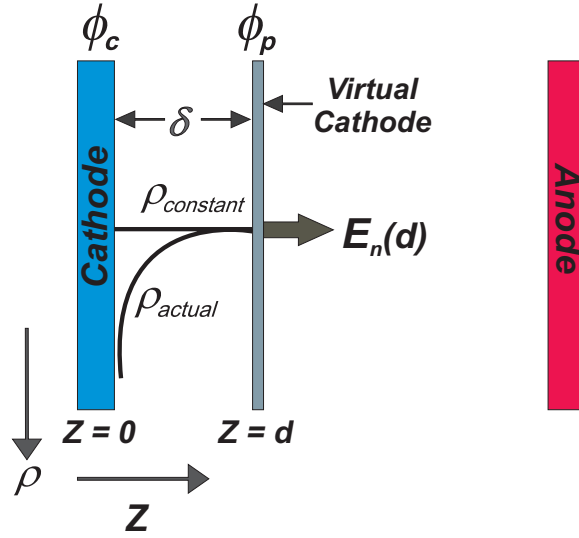 which is the normal electric field at the surface of the virtual cathode. Substituting it into eq (6.17) gives,

Figure 6.7: The figure depicts the charge distribution between the actual cathode and the virtual cathode. The actual charge density tends to infinity as the cathode is approached, which is replaced by an equivalent linear charge distribution.

$$[\phi(d) - \phi(c)] = \frac{3}{4}|\tilde{\mathbf{E}}_{\mathbf{n}}(\mathbf{d})|d \tag{6.19}$$

The first assumption to find an equivalent charge is to consider the charge constant inside the gap, although in reality the charge increases exponentially as one approaches the cathode. The first boundary condition is that this constant charge should satisfy the potentials and the electric fields at the virtual cathode in order to make the assumption valid. The idea behind considering a constant charge is to enable the integration of the *Poisson's equation*, which will yield

$$\frac{d\phi(z)}{dz} = \rho_{constant}z + c_1 \tag{6.20}$$

The constant of integration c_1 can be found by applying the boundary condition given by eq. (6.18), which then gives

$$\frac{d\phi(z)}{dz} = \rho_{constant}z + |\tilde{\mathbf{E}}_{\mathbf{n}}(\mathbf{d})| - \rho_{constant}d \tag{6.21}$$

Integrating the above equation once again along the gap gives,

$$\phi(z) = \frac{\rho_{constant}z^2}{2} + |\tilde{\mathbf{E}}_\mathbf{n}(\mathbf{d})|z - z\rho_{constant}d + c_2 \tag{6.22}$$

Again, the constant of integration c_2 can be determined by applying the boundary condition $\phi(z) = \phi(c)$ at $z = 0$. Re-arranging the terms after the substitution gives

$$\phi(z) - \phi(c) = \frac{\rho_{constant}z^2}{2} + z(|\tilde{\mathbf{E}}_\mathbf{n}(\mathbf{d})| - \rho_{constant}d) \tag{6.23}$$

Taking $z = d$ and substituting eq. (6.19) into the LHS of the above equation and re-arranging the terms will give

$$\rho_{constant} = \frac{|\tilde{\mathbf{E}}_\mathbf{n}(\mathbf{d})|}{2d} \tag{6.24}$$

which is the charge that is required to be filled inside the gap. It can be noted that this charge fulfils all the boundary conditions set by the space charge limited emission. If we consider a stream of particles equidistant along the normal connecting the real and virtual cathode surfaces Fig. 6.6, the above charge can be equally distributed among these particles. This procedure is repeated for all the samples over the emitter surface.

6.5.3   Simulation of a Planar Diode

The validation of the virtual cathode method can be made with a simple parallel plate diode. The diode considered here has an anode and a cathode of equal surface area of $1cm^2$ and are separated by a distance $d = 1cm$. The cathode is at a potential of -500V with respect to the anode. The problem space is discretized to a resolution of one million mesh cells, which then gives rise to a mesh resolution of around $0.01cm$. For the case of planar diode the gap width should theoretically play no role in the calculation of the space charge limited current since both the electrodes are parallel to each other and 1D *Child's law* can be directly applied. Two set of simulations have been made with a gap width of $\delta = 0.02cm$ and $\delta = 0.05cm$. The effect of the virtual cathode position can be clearly seen from the Fig. 6.8(a) and 6.8(b). The charge in the gap should vary linearly to ensure that the boundary condition at the virtual cathode is fulfilled. An increased gap width requires more particles to fill up the bigger space. From the simulations it can be

seen that the charge density in the anode-cathode gap conforms well with the analytical solution, as shown in the Fig. 6.9(a). Similarly a plot for the potential distribution in the anode-cathode gap is made in Fig. 6.9(b). It can be noticed that the error is less than five percent in either case and the deviation from the analytical curve only becomes obvious as we approach the cathode surface. A smaller gap width on the other hand can reduce the error in charge density while approaching the cathode surface.
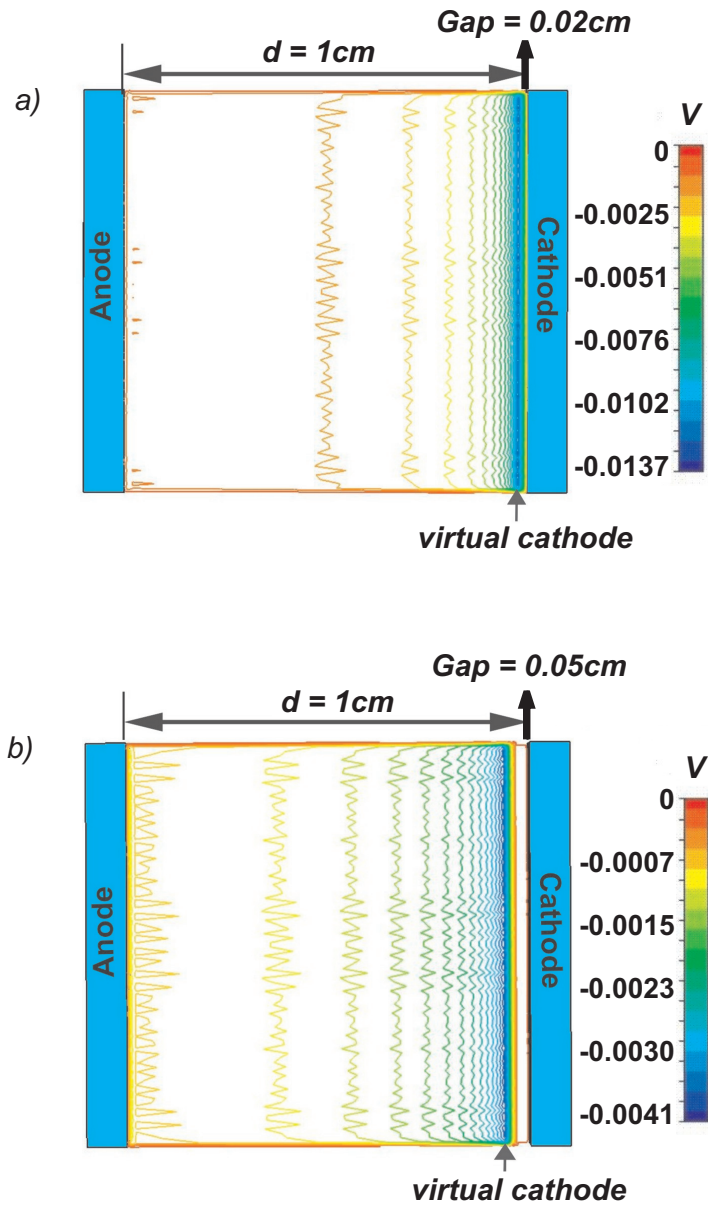
Figure 6.8: (a) A 2D view of a planar diode simulation with the virtual cathode method. The Iso-surface plot shows the gap and the potential distribution around it. The simulation has been performed with approximately 500 particles per time step.
(b) Simulation with the same input conditions but with an increased gap width, which can be visualized clearly by the displacement of virtual cathode. The noise in the contours is due to the interpolation error in post processor.
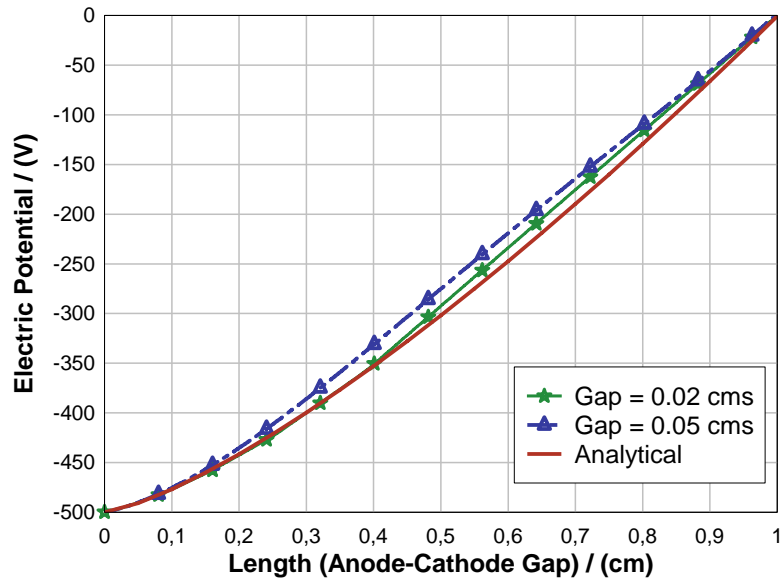
(a)
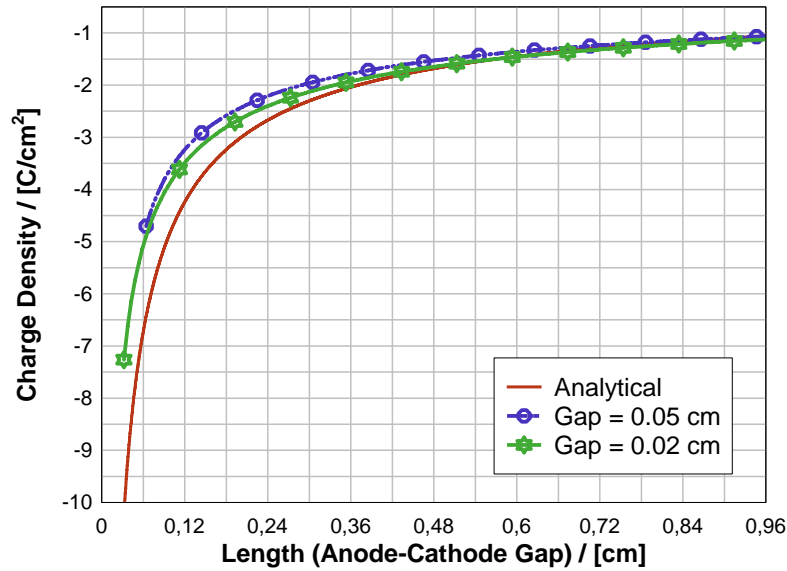
(b)

Figure 6.9: (a) The charge density as a function of the inter-electrode spacing for two different gap widths is shown.
(b) The potential distribution inside the gap anode cathode gap for the two gap widths.

6.5.4   Charge Conservation Method

The solution given to the 1D *Child's law* problem in the *Virtual Cathode* method still has few pitfalls and can result in erroneous results for emitters which are critically curved [41]. Besides it is cumbersome to find the right gap width for the solution to converge. This not only makes the *Virtual Cathode* method unstable for critical emitter shapes but also costly in terms of computational time as it requires additional interpolations of charge and fields inside the gap in each time step. Here we develop a *Charge Conservation* algorithm to overcome the afore mentioned problems.

As stated previously the space charge limited emission assumes the total electric field consisting of the tangential and normal components, to be zero on the surface of the cathode. The tangential component of the electric field on a perfect electric conductor is zero, which is intrinsic to the electrostatic field solver. Now we have to find the charge distribution and initial conditions of the particles, that would impose the condition of vanishing normal component of the electric field. It has been already shown that such a solution can be found by solving the *Poisson's equation* along with a set of initial conditions given by the equations of motion. The *Poisson's equation* in integral form can be written as,

$$\int\int_{dV} \varepsilon(\nabla\phi) \cdot d\vec{A} = \int\int\int_{V} qdV \tag{6.25}$$

where q is the charge inside the volume V. Substituting $\tilde{\mathbf{E}} = -\nabla\phi$ in the above equation and using eq. (3.6) results in eq. (3.3), which is the *Gauß law*. The significance of eq. (3.3) is that the total electric flux from the surface enclosing a volume is equal to the total charge enclosed by the volume. The numerical solution of this law is implemented in *CFIT* with its discrete counterpart given in eq. (3.7). As it is known that the electric fluxes are integrated over the faces of the dual grid, we consider all those boundary dual grid cells that intersect the emitter over which we have to calculate the current.

Once again writing the discrete counterpart of eq. (3.3) for a dual grid cell shown in Fig. 6.10, we have
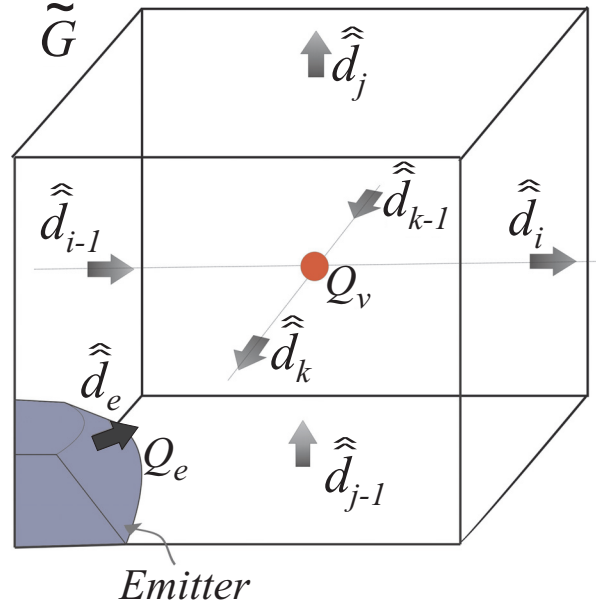
Figure 6.10: A boundary dual grid cell containing a part of the emitter

$$-\hat{\hat{d}}_{i-1} + \hat{\hat{d}}_i - \hat{\hat{d}}_{k-1} + \hat{\hat{d}}_k - \hat{\hat{d}}_{j-1} + \hat{\hat{d}}_j + \hat{\hat{d}}_e = -(Q_e + Q_v) \qquad (6.26)$$

where the electric fluxes are integrated over the exact areas of the corresponding cell faces, excluding the material intersections. It should also be noted that an additional electric flux term $\hat{\hat{d}}_e$ is only added for more clarity of understanding the original *Maxwell equation* and has no particular significance otherwise in the discrete model. The discrete equation represents the flux that flows through the cell surface, encompassing the entire volume, which in this case is a boundary dual grid cell.

The total charge inside a boundary dual grid cell at any instance of time is a combination of the charge already present inside the cell volume and the charge that enters from the adjoining cell faces. In this case it would be an emitter that would contribute charge to the dual grid cell. Hence the total charge inside the volume consists of two terms, Q_e the charge that enters the cell volume from an emitter and Q_v the charge already present inside the cell. However the *SCL* emission implicitly has the condition for normal component of the electric field to be zero, from which we have $\hat{\hat{d}}_e = 0$. Substituting this in eq. (6.26), we find that the left hand side is the total electric

flux through the faces of dual grid cell, which is already known. On the right hand side we known the charge enclosed by the boundary dual grid cell. By rearranging terms, the charge entering the dual grid cell from the emitter can be calculated.

$$Q_e = [\hat{\hat{d}}_{i-1} + \hat{\hat{d}}_i - \hat{\hat{d}}_{k-1} + \hat{\hat{d}}_k - \hat{\hat{d}}_{j-1} + \hat{\hat{d}}_j] - Q_v \qquad (6.27)$$

In other words Q_e is the charge that should be emitted to have a vanishing electric field on the emitting surface, which is nothing but the *space charge limited emission*. The process is repeated over all boundary dual grid cells until the solution converges. When there is no increase in the charge Q_e within a given tolerance, field-charge consistency is said to have reached.

6.5.5 Comparative Study for a Planar Diode

The *Charge Conservation* method has obvious advantages over the *Virtual Cathode (VC)* method. First it doesn't consider the 1D model for the calculation of the *Child's law* current, which is not only costly in terms of computations that have to be performed but also its dependence on the selection of an optimum gap width. On the other hand *Charge Conservation* method considers the exact volume and area integrals which are already implemented in *CFIT* with great accuracy, therefore we make no error in the charge and current calculations and the accuracy is totally dependent on the discretization of the problem space. It also has the flexibility to choose the initial velocity of the particles, since it directly obtains the charge and decouples the velocity with current calculation, which is more complex to deal in the *Virtual Cathode* method. A thermal velocity distribution of electrons for a space charge limited thermionic cathode can be easily introduced here, whereas in the *VC* method, it requires to integrate the velocity distribution function and find the location of the potential minimum outside the cathode. The *Charge Conservation* method considers the same planar diode for validation used in the previous case. The convergence of charge density using both the methods is compared in Fig. 6.11, which show good agreement with the analytical solution.

A comparison of the *CPU time* for simulating the above problem using both the methods is shown in Fig. 6.12. The plots show the time taken for executing the emission module, which includes the calculation of charge over all samples, interpolating the fields on the sample positions and generating a particle array with necessary initial conditions. It is evident from the graph
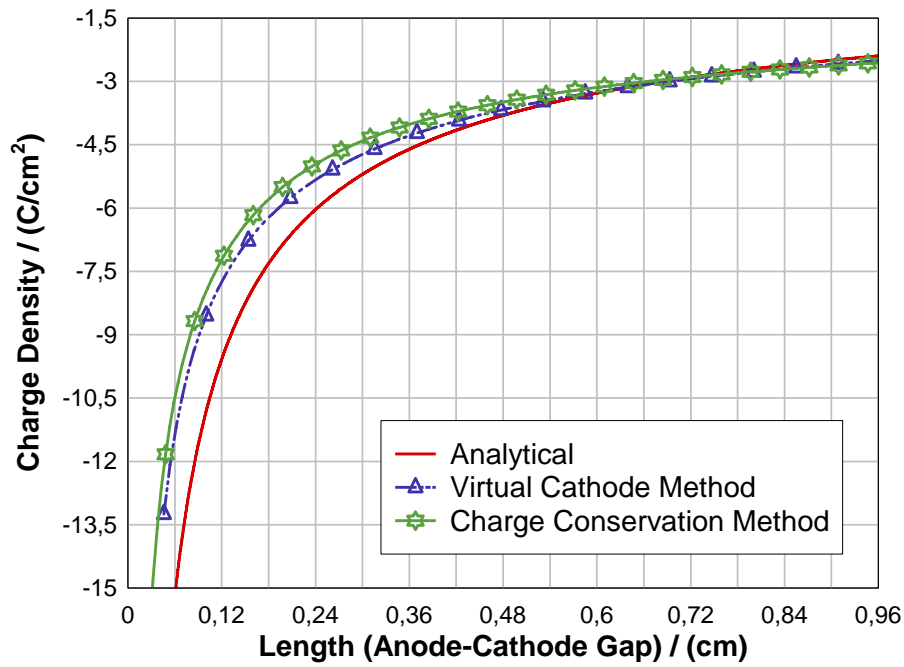
Figure 6.11: The graph shows the charge density inside the anode-cathode gap calculated using the *Charge Conservation Method* and the *Virtual Cathode Method* for a discretization of one million mesh cells.
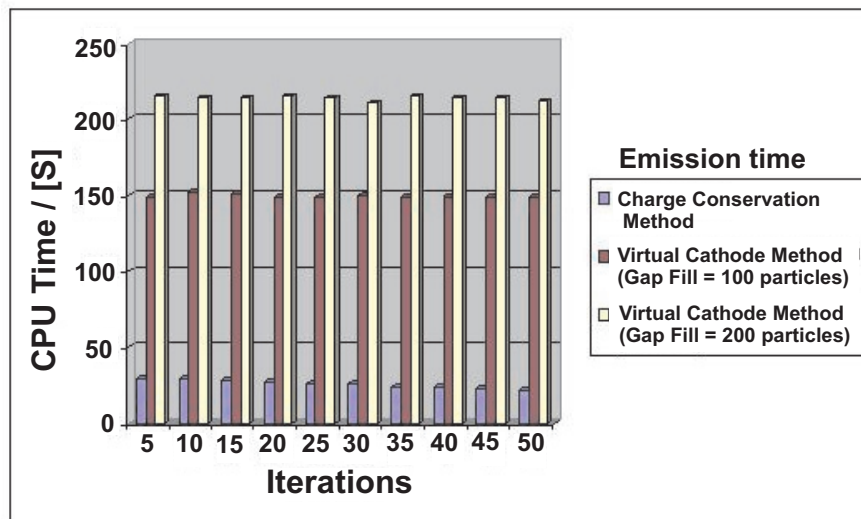

Figure 6.12: The *CPU time* for both *Virtual Cathode* and *Charge Conservation Method* for emitting 500 macro particles in each time step. The calculation time scales with *O(N)*, where *N* is the number of macro particles to be emitted.

that the *Virtual Cathode* method is computationally costlier than *Charge Conservation* method and the CPU time increases with an increase in the number of particles inside the gap.

6.6 Field-Charge Consistency

Until now the methods to calculate the space charge limited current given by *Child's law* have been presented. Now we have to select an iterative method with which the space charge is filled up in the entire problem space in each time step. In other words, the problem space should have a potential distribution that would satisfy the steady state condition given by the space charge limit. This requires injection of space charge into the problem space and solving for the fields until the solution converges and a steady state is reached, where the fields and space charge remain constant within a given tolerance. There are two iterative methods that can be used to achieve the field-charge consistency condition, which will be presented in this section.

6.6.1 Trajectory Iterative Algorithm

The *trajectory iterative algorithm* as the name suggests is an iterative method that recursively corrects the path of the electrons inside a problem space for a given potential distribution [42]. If we calculate the fields by solving the *Laplace equation*, we can then solve the particle equations of motion eq. (4.3) to trace the particle trajectories inside the problem space Fig. 6.13. Once the path of the charge particles is known, the space charge distribution and the corresponding change in the potential distribution is calculated. After updating the new fields the new charge to be emitted is calculated and the trajectories are traced again. This iterative procedure is continued until the charge and field converge to a steady state.

The iterative method starts with the calculation of the potentials everywhere inside the problem space and from the given potential distribution an equivalent charge is calculated using *Child's law*. The macro particles carrying this charge are traced till the end of the problem space by calculating the forces acting on the particle due to the fields. The charge is left on the nodes of all grid cells it traverses. From the second iteration cycle the *Poisson's equation* is solved, with the charge that was left over the grid points from the previous iteration. The Potential distribution in the beginning correspond to a problem that had no space charge inside the problem space. If the charge calculated from such a potential distribution is emitted, it would result in
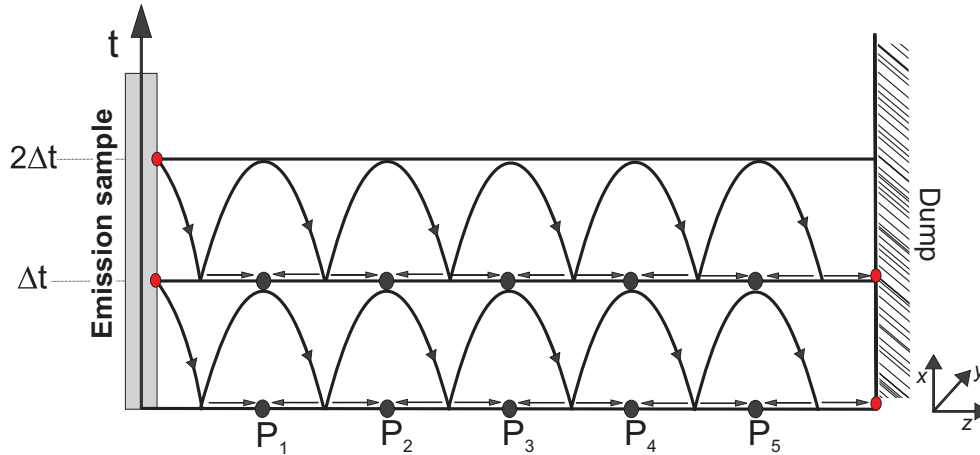
Figure 6.13: The figure depicts the *trajectory iterative algorithm*in 1D. Particles generated at an instance Δt are traced till the dump. In this process the charge is deposited on the grid nodes P_1, P_2, P_3, P_4, P_5 all along the trajectory. New trajectories can be traced in the time step $2\delta t$ after updating the fields due to the charge distribution in previous time step δt.

a sudden fluctuation in the potential distribution inside the problem space which is unphysical. This change in the potential distribution would then effect the charge that is to be emitted in the following iteration cycles. The cumulative error finally results in an oscillatory solution that will not converge towards the actual solution. The process of adjusting the potentials and charge in every iteration cycle for the solution to converge is known as relaxation [43]. Here we introduce a *relaxation factor* ω, which ensures that a fraction of the total charge calculated in each iteration is released into the problem space, so that the transition from a no space charge to a space charge limited state is smooth without oscillations. A *Successive Over Relaxation (SOR)* algorithm is used in this emission model for the iterative process to converge towards the desired solution. The charge that is to be emitted in each iteration can be written as

$$\rho_n = \omega\rho_n + (1 - \omega)\rho_{n-1} \qquad (6.28)$$

where ρ_n is the charge calculated in n^{th} time step and ρ_{n-1} is the charge that is emitted in the $(n - 1)^{th}$ time step. The convergence of the solution again depends on the initial guess of the relaxation factor and has to be adjusted according to the rate of convergence. If the charge in a time step exceeds
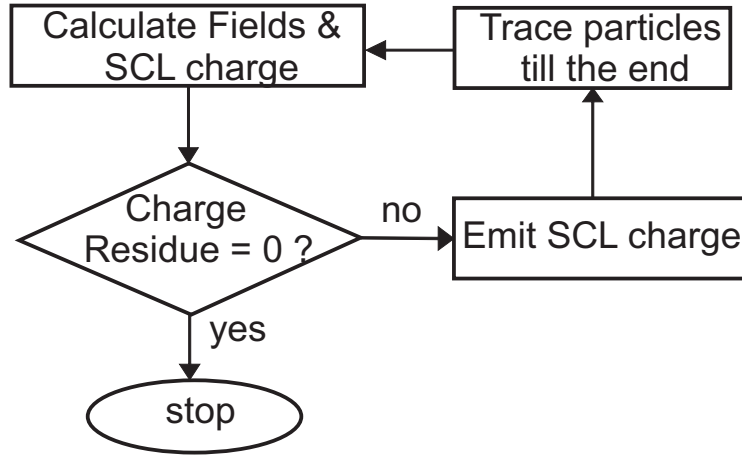
Figure 6.14: The flow chart of the *trajectory iterative algorithm.*

that of the previous time step, it is evident that the solution is diverging and the iterative process is terminated and a new relaxation factor is selected. The computational cycle of the *trajectory iterative algorithm* is given by the flow chart in Fig. 6.14.

6.6.2   Time Iterative Algorithm

The time iterative algorithm solves for the fields along with the equations of motion in each time step. The procedure starts by getting the potential distribution inside the problem space by solving the *Laplace equation.* The charge under space charge conditions is then calculated from the above potential distribution. This charge is emitted and the particles are pushed into the problem space. The new potential distribution is obtained using the *Poisson's equation* after depositing the charge on the respective grid nodes. It has to be noted that the particles are pushed only once before the new fields are calculated. Unlike the *trajectory iterative algorithm* the particles can only traverse through a single grid cell in each time step Fig. 6.15. The iterative procedure is repeated till a steady state has been reached and the charge and fields are consistent with each other. The flow chart of a typical time iterative algorithm is given in Fig. 4.2.

6.6.3   Convergence Studies

The important consideration in the selection of an iterative method is convergence. This in turn depends on the type of the problem that is being
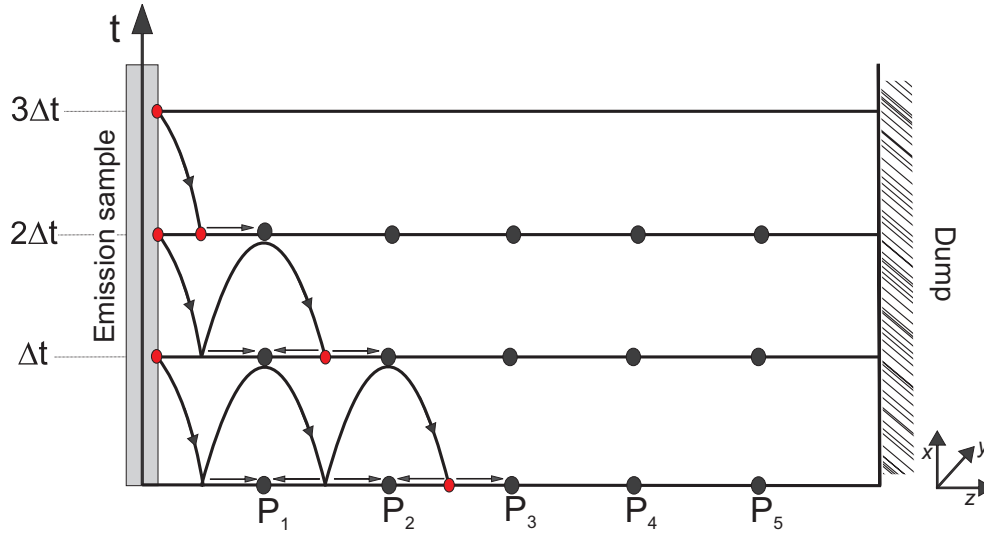
Figure 6.15: The figure shows a 1D *time iterative algorithm.* The particles emitted in the time step Δt are pushed into the problem space. The new fields are then calculated from the charge distribution at Δt. The new charge is now calculated at time step $2\Delta t$ and pushed into the problem space. The particle that had been emitter in Δt will also undergo a push. It can be seen that the particles can only traverse one cell in each time step.

solved. It is already known that the convergence of SOR method depends on the selection of an appropriate relaxation factor. The general limits of the *relaxation factor* ω is between 0 and 2. But for the problem of space charge limited emission the upper bound is equal to 1 and in almost all practical problems, is a fraction of that limit. The charge calculated with $\omega = 1$, when injected into the problem space will result in an inaccurate solution of the potential distribution. The result is a solution that oscillates with an amplitude equal to the error in the space charge and the solution diverges. This condition is often referred to as *under damping.* Hence we select $\omega < 1$,that injects the charge gradually into the problem space in each iteration. On the other hand if the initial guess of ω is less than the optimum value, oscillations can be avoided but the solution will not converge within the tolerance range. This condition is defined as *over damping.* The solution that converges within specified tolerance range in a reasonable number of iterations is called a *critically damped* solution.

The relaxation factor for space charge problems lies between 0 and 0.1. For practical simulations the value of relaxation parameter is lesser than 0.1 as

can be seen from the convergence plots Fig. 6.16. In simulations that employ fine grid, the relaxation factor takes a bigger value than a coarser grid for the same problem. A fine grid dampens the oscillations resulting from a large relaxation factor, whereas the coarser grid will continue to propagate the error.

The three graphs in Fig. 6.16 progressively show how the planar diode reaches the steady state. The iterations are continued until the final solution is within the tolerance range. It has to be noted that a smaller relaxation factor would not ensure a better convergence if the grid is coarser. In such cases the discretization error overrides all other criteria. Hence the number of particles that sample the charge distribution, the external grid resolution and the input conditions play the primary role in convergence of the solution. As another example the convergence of a spherical diode is considered as shown in Fig. 6.17. The afore mentioned criteria play a very important role for a spherical diode than the planar diode as the curvature effects come into the problem. The grid resolution is 2.5 million mesh cells and convergence is studied using four different relaxation factors. The three different cases of damping can be clearly seen using different relaxation factors.
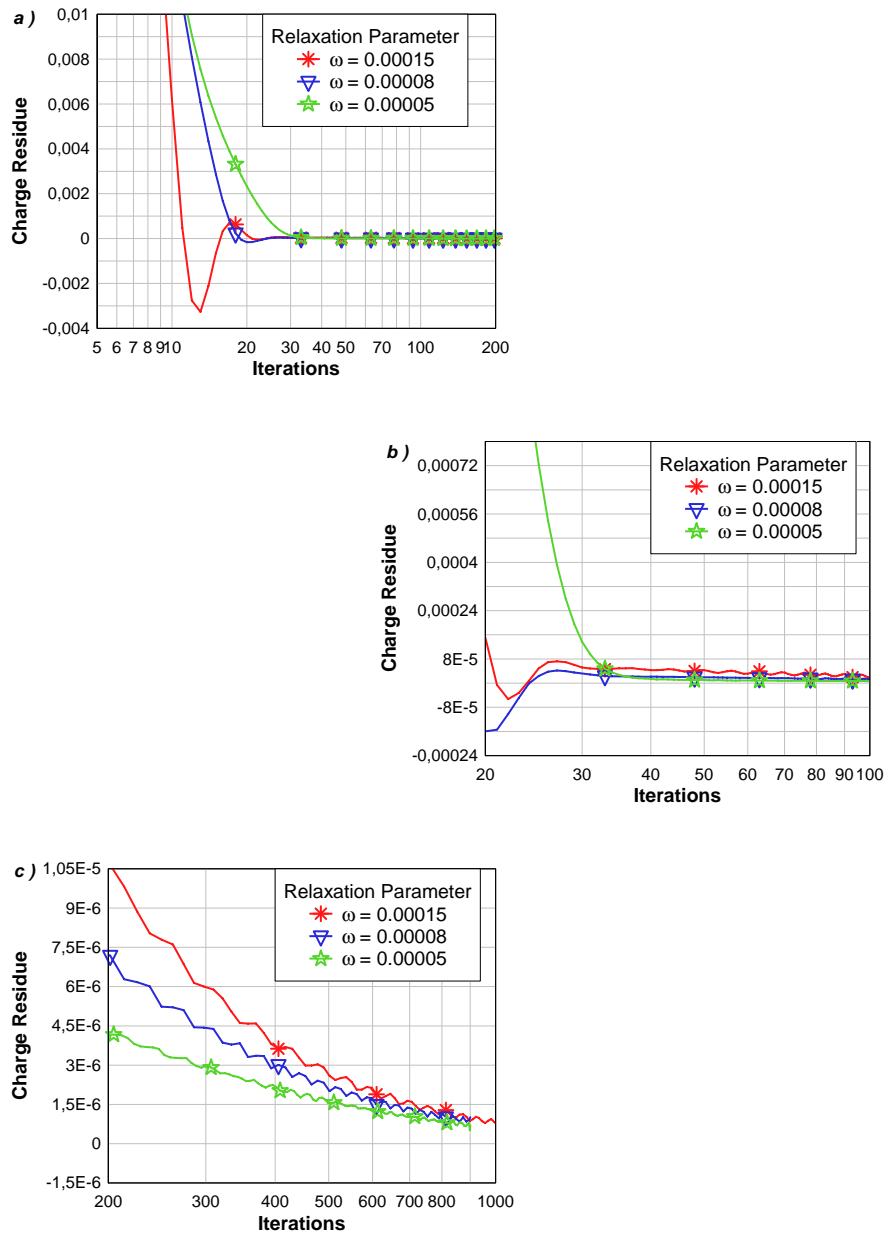
Figure 6.16: The convergence study of a spherical diode. (a) Convergence of the charge for three different relaxation factors. The solution for the larger relaxation factor $\omega = 0.005$ is *under damped*. (b) The solution converges faster for $\omega = 0.0005$ but oscillates above the tolerance range. (c) For $\omega = 0.00001$ the solution is *over damped* and for $\omega = 0.00007$ the solution shows good convergence and corresponds to *critical damping*.
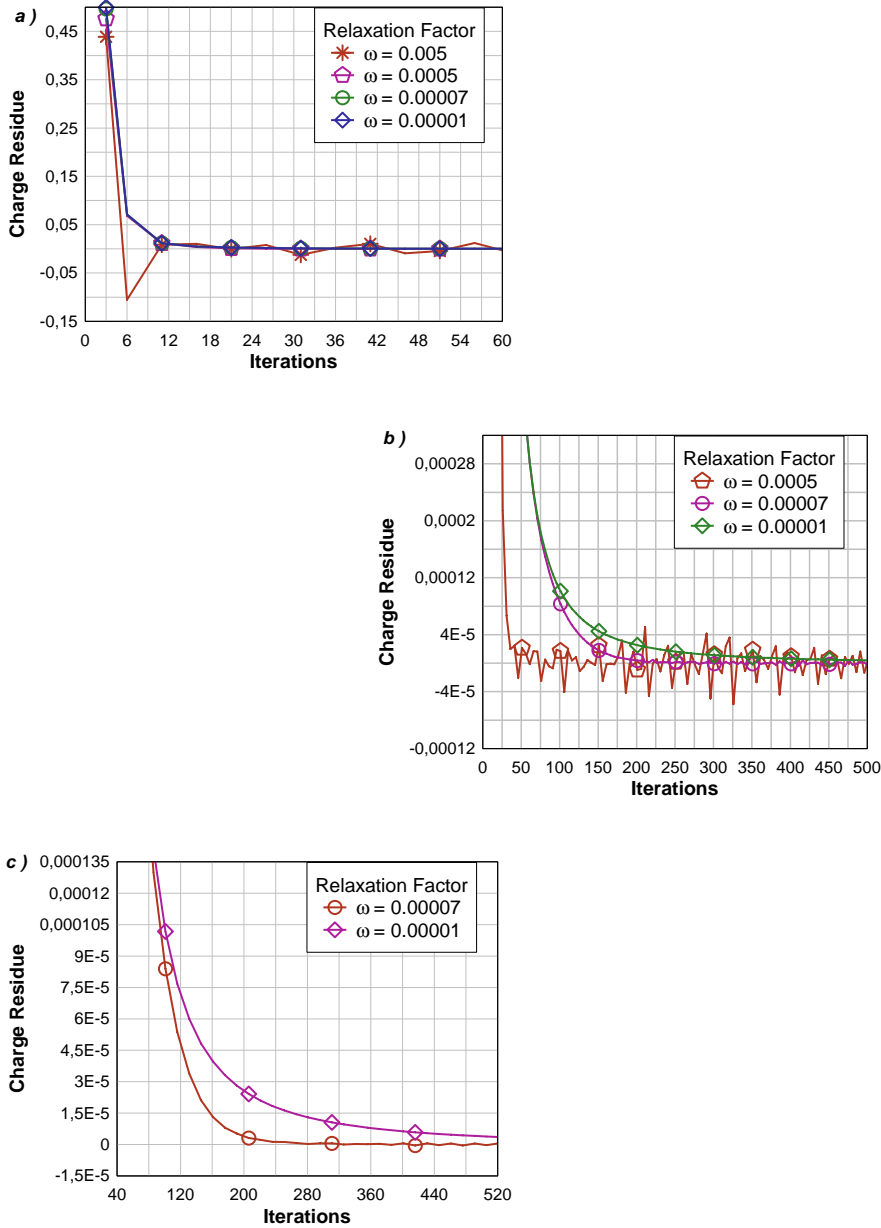
Figure 6.17: The convergence study of a spherical diode. (a) Convergence of the charge for three different relaxation factors. The solution oscillates for the larger relaxation factor $\omega = 0.00015$ and corresponds to the case of *under damping*. (b) The solution takes longer to converge for $\omega = 0.00008$. This is the case of *over damping*. (c) For $\omega = 0.00005$ the solution converges faster and corresponds to *critical damping*.

Chapter 7

Simulations and Applications

It has been shown in the previous chapter that both the *Charge Conservation* and *Virtual Cathode* method agree well with the analytical solution in the case of a planar diode. Since the planar diode already has an exact analytical solution in 1D, a numerical solution is of less importance. As it has been mentioned in the previous chapter, a planar diode is rarely found in practical applications due to the small effective area of emission. However, it stands as a benchmark test for the worthiness of a numerical model. For practical applications, emitters come in different sizes and shapes. To standardize the methods discussed in the previous chapter and to establish their robustness, a thorough study is made here using a spherical and cylindrical diode. As an application problem, the simulation of a *Traveling Wave Tube* is presented at the end of the chapter.

7.1 Spherical Diode

The spherical diode geometry is widely used in the design of the emitters. This is due to the fact that the effective surface area of emission is large for spherical symmetry when compared to planar emitters. In this test problem we consider two concentric spheres, with the smaller sphere of radius $r_c = 2.0 cm$ as cathode and the larger sphere with a radius of $r_a = 2.5 cm$ as anode Fig. 7.1. The anode is at a potential of $10kV$ with respect to the cathode. This particular spherical diode geometry gives rise to a divergent beam, and electrons travel radially outward and are collected on the anode. On the contrary if the cathode constitutes the outer sphere, the beam converges to the anode.

The analytical corrections to the 1D space charge limited current in the case
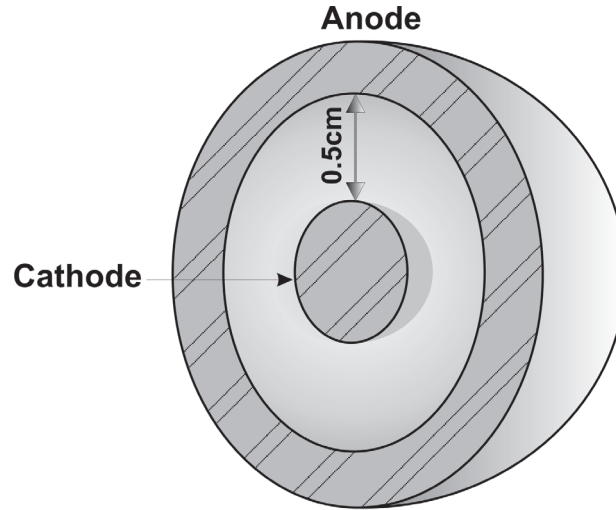
Anode

0.5cm

Cathode

Figure 7.1: The cross-sectional view of a spherical diode. A grid of 2.5 million mesh cells was used to dicretize the problem space.

of a spherical diode was made by *Langmuir* and *Blodgett* and is given by the eq. (6.15). The current is independent of the actual size of the electrodes. The equation given there has a *perveance* correction factor, which appears as a logarithmic series of the ratio of anode to cathode radii. This series which is given, up to six terms, holds good for the ratio of anode to cathode radius of less than 5 units. Hence the problem defined here fulfils the conditions set by the analytical equation given therein. The simulation has been performed starting from a grid resolution of 1 to 2.5 million mesh cells. The radial charge density inside the anode-cathode gap using the *Charge Conservation Method* is plotted in Fig. 7.2. It can be noticed that at small mesh resolutions the convergence is very poor owing to the fact that the emitter surface is curved and has to be finely discretized to minimize the curvature effect. The convergence study is made with a relaxation factor of $\omega = 0.00008$. The importance of grid resolution on the radial distribution of charge density is visualized in Fig. 7.3, where the charge density is calculated at a distance of $0.25cm$ away from the cathode, into the anode-cathode gap. It can be seen that for low grid resolution, the charge oscillates with a greater amplitude compared to a finer grid. Besides that, the charge is also offset with respect to the analytical solution by a higher value than the case of a finer mesh.

In a further simulation, a comparative study of the *Virtual Cathode* and *Charge Conservation* methods is done to validate the convergence of both
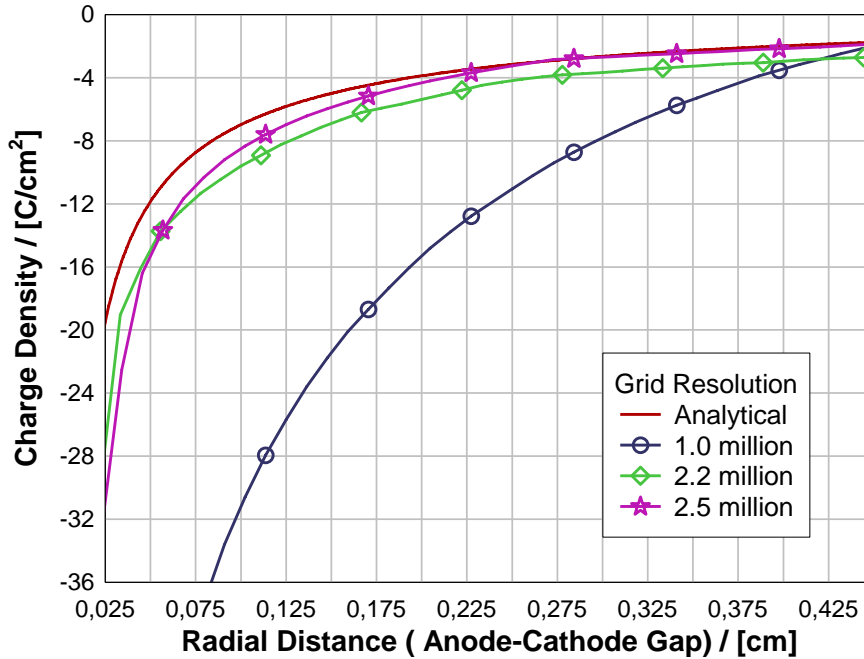
Figure 7.2: A plot of charge density as a function of the radial distance in the anode-cathode gap. The simulations have been performed using the *Charge Conservation* method.

for a curved emitter. Fig. 7.4 shows the charge density along the radial direction for both the methods. It can be observed that both the methods converge well with respect to the analytical solution.

A corresponding plot of the potential distribution in the anode-cathode gap is plotted using the two methods and both are found to confer well with the analytical curve Fig. 7.5. The discrepancy that might arise in the case of the *Virtual Cathode (VC)* method is due to its dependence on 1D model. Theoretically the *VC* method will have very good convergence if the radius of the anode is very large when compared to cathode, so that the radius of curvature seen by the virtual cathode tends to infinity making the electrodes look each other as parallel plates. In other words, the virtual cathode should be very close enough to the actual cathode to fulfil the above condition. But selecting such a gap width again depends on the grid resolution. On the other hand, inaccuracy in the *Charge Conservation* method arises purely from the discretization error.
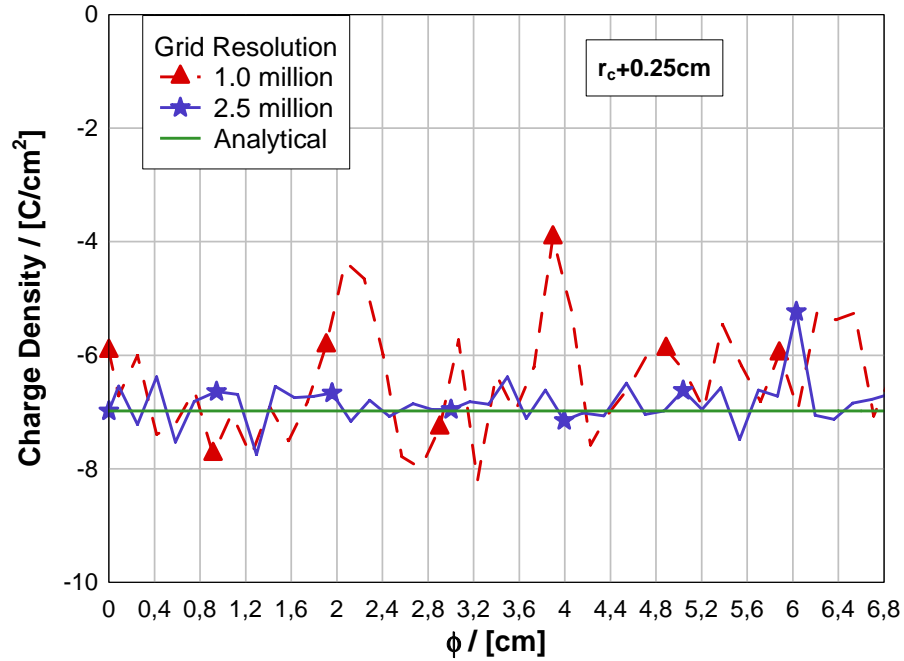
Figure 7.3: The plot shows a transversal profile of charge density at a distance of 0.25cm from the cathode
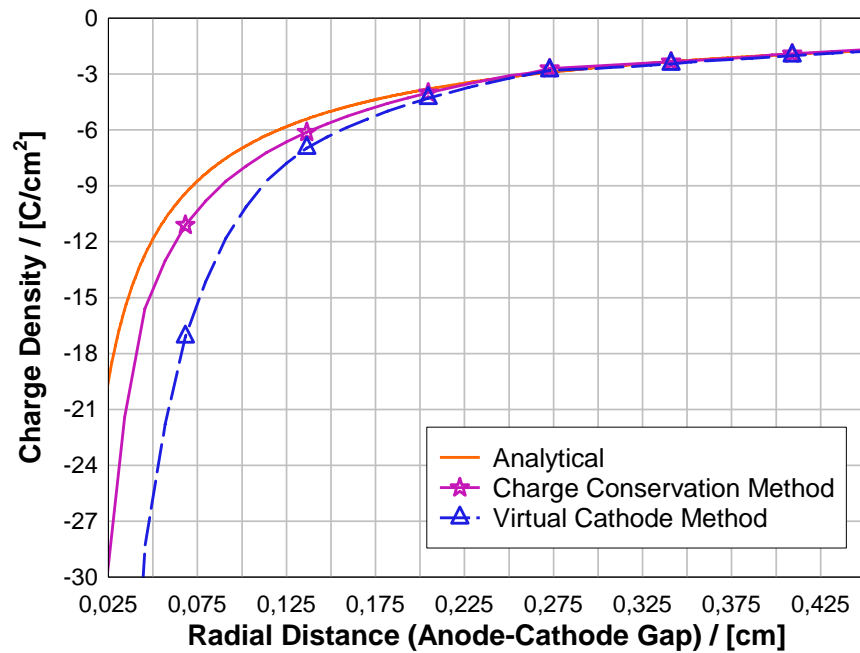

Figure 7.4: A comparison of charge density in the anode-cathode gap using *Virtual Cathode* and *Charge Conservation* methods.
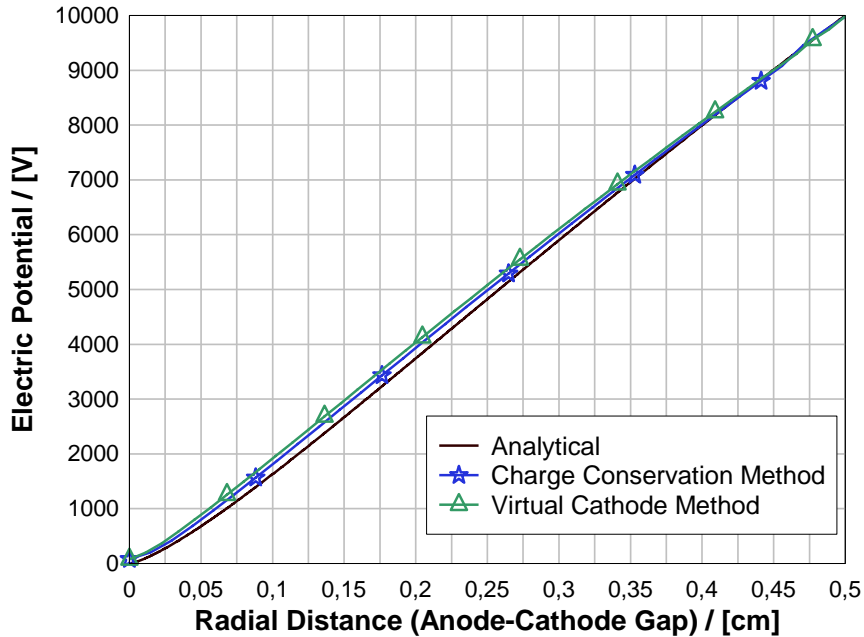
Figure 7.5: The plot shows potential distribution along the radial direction.

7.2 Cylindrical Diode

As a second validation problem a circular cylindrical diode is used for its many applications among electron tubes such as coaxial magnetrons and other cross-field devices. The analytical correction to the 1D space charge limited current is made by *Langmuir* given in eq (6.13). Though circular cylindrical diodes have axial symmetry and are often studied by reducing them into a 2D problem [44], curvature produces significant changes in the fields and charge on the surface of the emitter, necessitating a study in 3D. The diode in this problem consists of a cylindrical cathode of radius $r_c = 1.0cm$ and an anode of radius $r_a = 2.3cm$ as shown in Fig 7.6. The cathode is maintained at a potential of $-10kV$ with respect to the anode. The simulations are conducted with grid resolutions of 1 and 2 million mesh cells respectively.

The convergence of the *Virtual Cathode (VC)* method is given by the graphs in Figs 7.7 and 7.8. In the first graph the convergence for different gap widths (distance between actual cathode and virtual cathode) is shown. It can be noticed that when the gap width is varied from $0.02cm$ to $0.0002cm$ the convergence gradually improves and conforms well with the analytical solution.
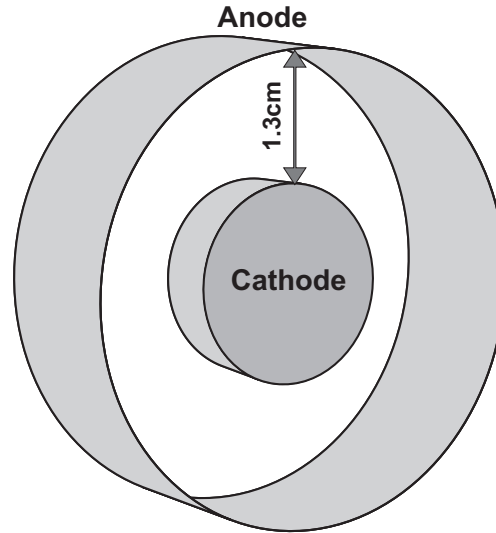
Figure 7.6: The cross-sectional view of a spherical diode. A grid of 2.5 million mesh cells was used to dicretize the problem space.

The reason for this, as mentioned previously is due to the planar model of *VC* method. But it can be seen from the Fig. 7.7, that when the gap width is further reduced from $0.0002cm$ to $0.00002cm$ there is no significant change in the convergence, which explains that when the gap width is smaller than the minimum grid step, the external fields cannot be resolved further and there would be no change in the current emitted. In the Fig. 7.8 the convergence is studied with respect to the external grid resolution. It can be noticed that the convergence is good and conforms well with the analytical solution as we take a finer grid as expected. At the same time it can also be noted that the gap width is a very crucial factor even with a fine discretization. As it can be seen, a gap width of $0.002cm$ shows almost same convergence with both finer and coarser grid resolutions, and the advantage gained in discretization is lost by selecting an incorrect gap-width. This also validates the above argument that a 2D model is not sufficient as it can be seen that there is considerable error in final output by not taking into account the exact curvature for a given anode-cathode gap.

The convergence in the case of *Charge Conservation* method can be visualized in the Fig. 7.9. It can be seen that the convergence improves quite well and conforms to the analytical solution as the number of mesh cells are increased from half a million to two million.
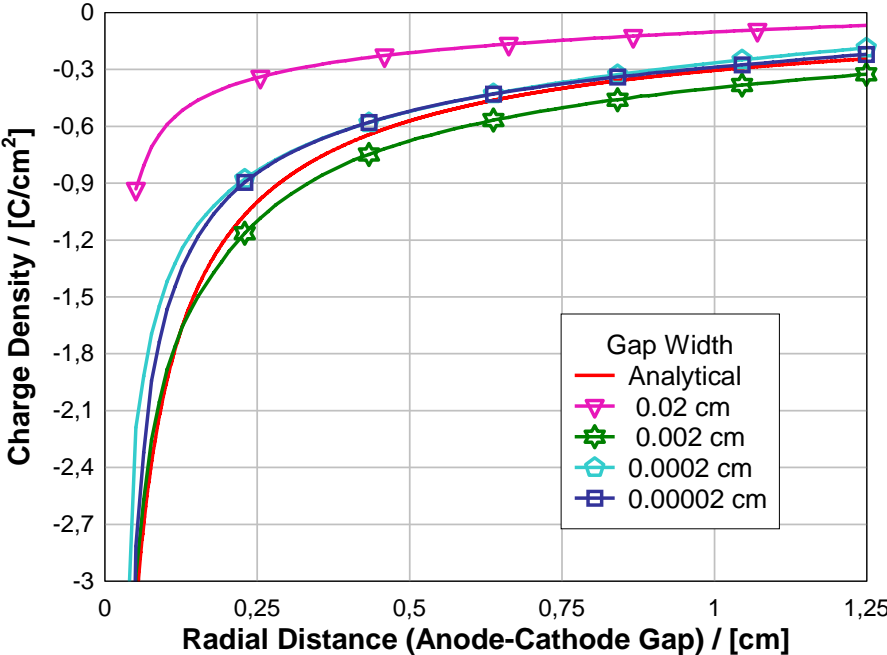
Figure 7.7: The graph depicting the importance of the gap width in *Virtual Cathode Method.*
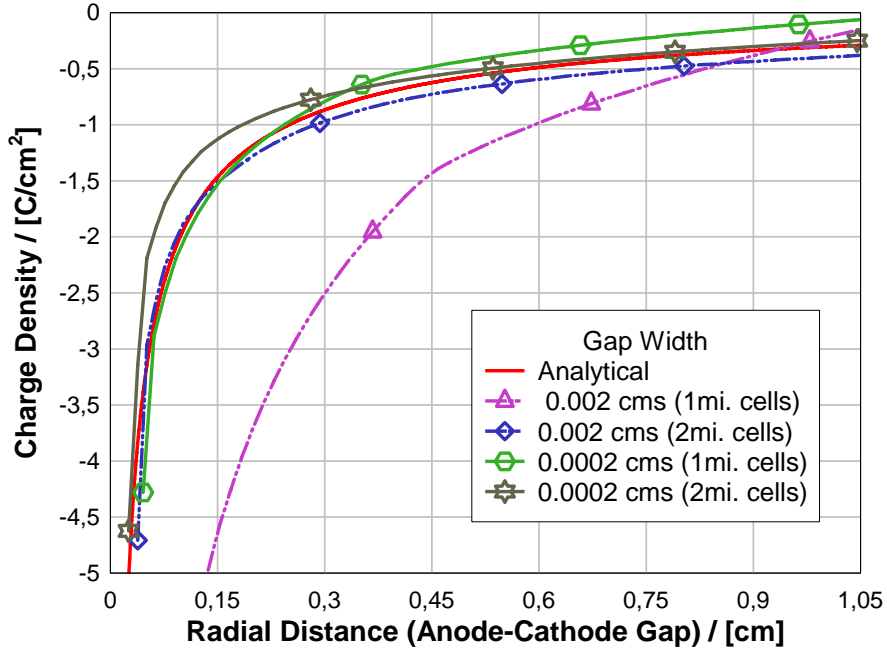

Figure 7.8: The plot of charge density in the inter-electrode space for different gap widths and grid resolutions.
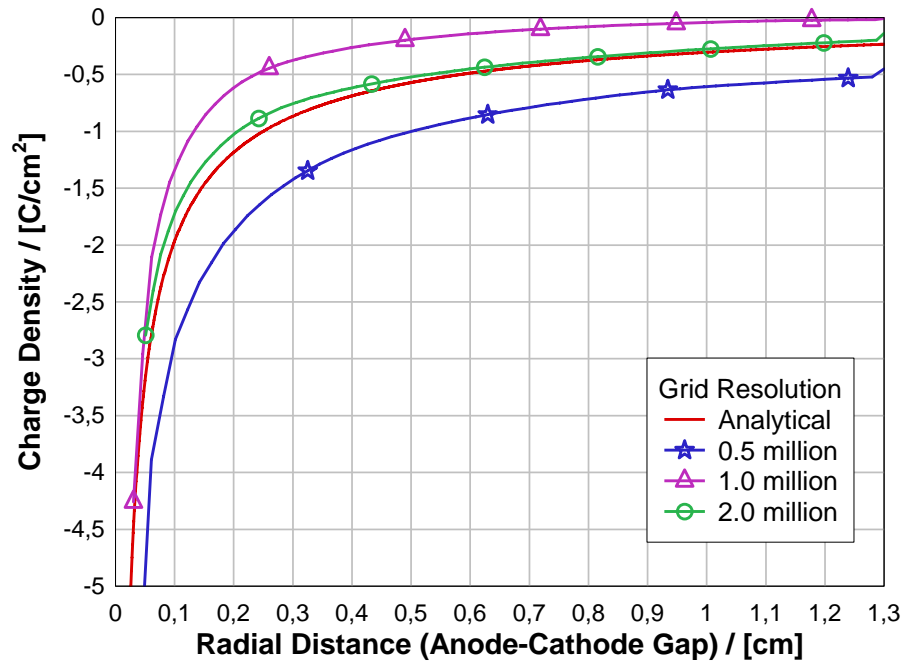
Figure 7.9: The plot depicting the convergence of the *Charge Conservation Method* for different grid resolutions.
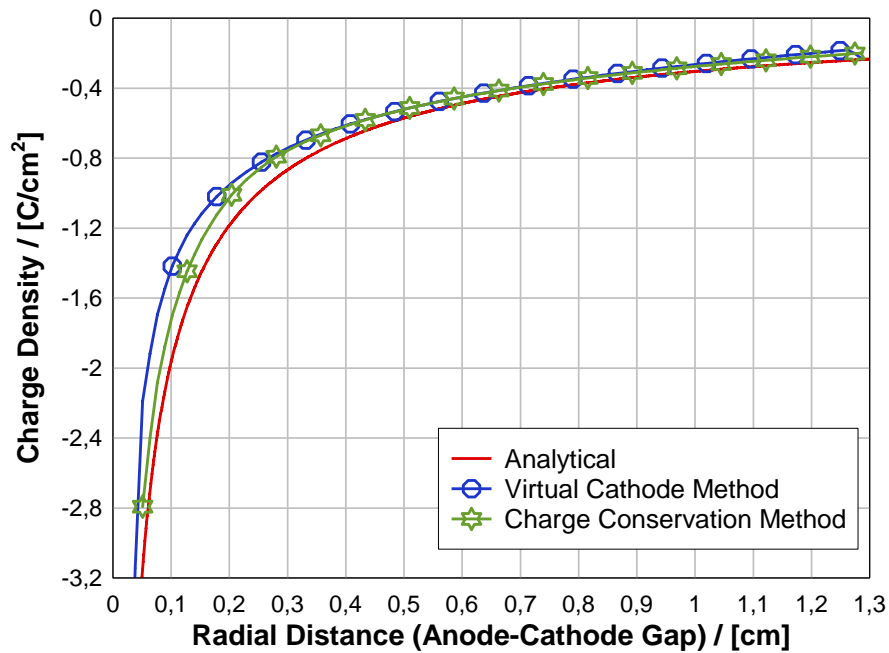

Figure 7.10: A comparison of the *Charge Conservation* and *Virtual Cathode* methods for a grid resolution of 2 million mesh cells.

The Fig. 7.10 shows a comparison of both the *Virtual Cathode* and *Charge Conservation* methods with a resolution of two million mesh cells. It can be seen that both the methods are in good agreement with the analytical solution. While gap width and grid resolution play a very important role in the convergence of the *Virtual Cathode* method,in *Charge Conservation* method it is just the resolution of the external grid that decides the convergence. In case of the latter method the accuracy of the conformal mesh is crucial as any errors in calculation of volumes and areas from the material intersections will result in an error in electric flux and that in turn results in an erroneous charge calculation. The *CFIT* is very precise for this purpose and hence the errors can be avoided.

7.3 Traveling Wave Tube Amplifier

The *Traveling Wave Tube Amplifier (TWTA)* is a broadband microwave device [45,46]. It is widely used in space and military applications. The device consists of an electron gun that forms the source of electrons, a beam focusing structure that guides the electrons through the tube, an interaction section where the beam interacts with the radio frequency (rf) signal and energy transfer takes place and finally the collector where the beam is dumped. The longitundinal cross-section of the device can be seen in Fig 7.11. Here only a part of the device is taken for simulation and the collector section is omitted as the emission problem doesn't require the simulation of the entire device, which is discussed in further sections. Here we shall consider the simulation of the above device using both the methods that have been discussed previously. Before that a brief description of the various components of a *TWTA* will be presented here.

Electron Gun :
The electron gun of a *TWTA* consists of a cathode that emits electrons, a focusing electrode to confine the emitted charge into a narrow beam and an anode that will accelerate the electrons away from the cathode. The *TWTA* discussed here uses a *Pierce type* electron gun [47]. The purpose of this type of arrangement is to focus the electrons into a thin laminar flow. The cathode is designed based on the principle of a spherical diode discussed in the beginning of the chapter. The *Pierce gun* is a conical section of a spherical diode as shown in the Fig. 7.12. This not only offers greater effective area of emission but also acts as a beam converging lens with a suitable positioning of the focusing electrodes. The total current in a spherical diode is given by

Focusing Magnets
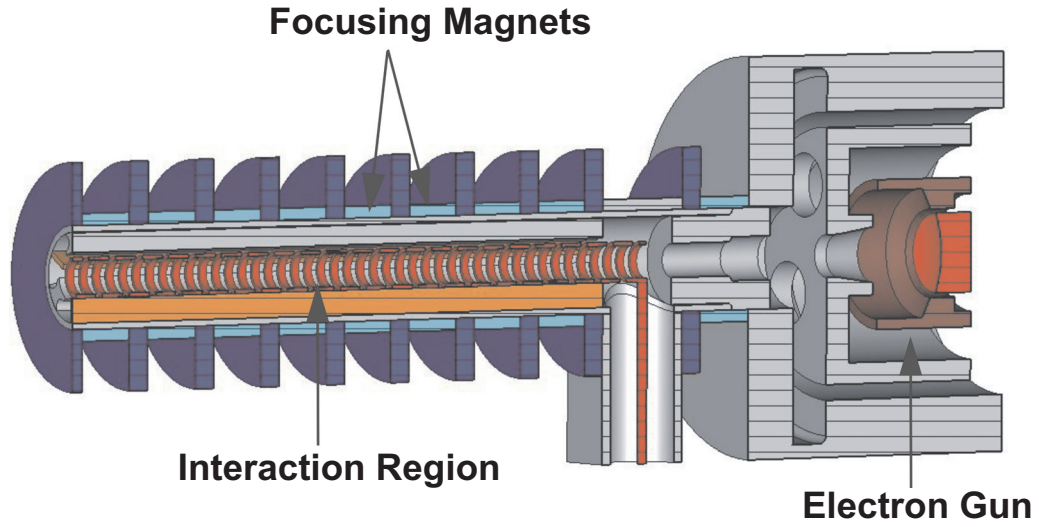

Interaction Region

Electron Gun

Figure 7.11: Longitudinal cross-section of the *Traveling Wave Tube Amplifier*.

the *Langmuir-Blodgett* eq. (6.15). Now the current in such a conical section, in terms of the total current in the spherical diode can be written as

$$I = \frac{1 - \cos\theta}{2} I_s \qquad (7.1)$$

where, I_s is the total current in the spherical diode with r_c and r_a as the radii of cathode and anode respectively and θ is the half angle of the cone.

The emitted electrons from the cathode are then drawn away under the accelerating field of the anode, which is maintained at a higher potential. The charge so emitted and accelerated has to be confined into a narrow, laminar flow enabling it to enter the interaction region. For this purpose a focusing electrode, maintained at the same potential as cathode is introduced to correct the electron trajectories, which would otherwise diverge under the space charge effects [48,49,50]. A schematic of the *Pierce gun* can be visualized in Fig. 7.13.

The path of the electrons is always perpendicular to the equipotential lines. If electrons were to travel freely under the accelerating field of the anode
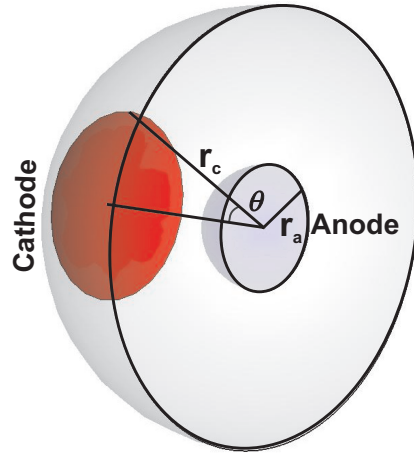
Figure 7.12: A conical anode-cathode section of *Pierce gun* realized from a spherical diode arrangement.

without a focusing electrode, then the equipotential lines would diverge due to the space charge created by the electrons as shown in Fig. 7.14(a). Under such conditions the electron beam would diverge and hit the walls of the tube. Hence a focusing electrode and its orientation with respect to cathode should be such that the equipotential lines are spherical despite the presence of the electron space charge Fig. 7.14(b). For simplicity if we consider a parallel plane diode, we have two regions of interest, one within the beam where *Poisson's equation* applies and another outside the beam where *Laplace's equation* holds. Now if we consider the trajectories of electrons at the edges of the cathode to be perpendicular to the surface, a one dimensional *Laplace's equation* with the boundary conditions $\partial\phi/\partial x = \partial\phi/\partial y = 0$ and $\phi = f(z)$ can be solved at the edge of the electron beam. Where ϕ is the potential and $f(z)$ is the *Child-Langmuir's* equation for the space charge limited emission.

The solution of the *Laplace's equation* in polar coordinates can be written as

$$\phi(r, \theta) = Ad^{4/3} \cos \frac{4}{3}\theta \tag{7.2}$$

where d is the inter-electrode distance. If $(4/3)\theta = \pi/2$ then $\theta = 67.5^0$, at which the potential is zero. Which means if an electrode of zero potential is placed at the above angle with respect to the edge of the cathode, the electron
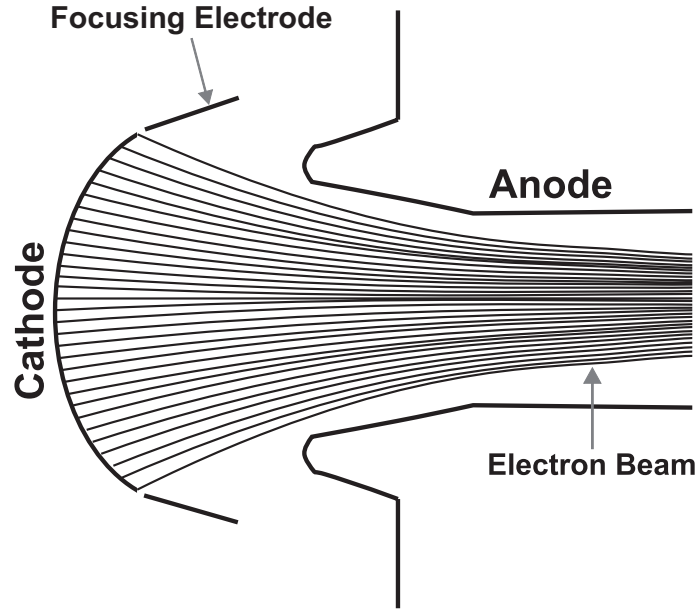
Figure 7.13: A typical *Pierce electron gun* with cathode, anode and focusing electrode.

beam can be confined to a laminar flow. In other words an electrode with zero potential placed at the above angle with respect to cathode will ensure perpendicular electron trajectories at the edge of the cathode that which can be found only in the case of a planar diode. This electrode is often referred to as *Pierce electrode* as can be seen in the Fig. 7.15. Once the electron beam is confined to a narrow laminar flow, it has to be extracted from the gun and injected into the interaction region. For this purpose the anode has an aperture through which the beam is extracted. At this point the effect of focusing electrode vanishes and the equipotential lines form a diverging lens. The beam then starts diverging, which then has to be confined using an appropriate magnetic field. The diverging lens has the effect that the beam, which has to converge at the edge of the anode, will now have the minimum beam width extending beyond the normal anode focal length Fig. 7.15.

The focal length of the defocusing lens can now be written as

$$f = -\frac{4\phi_a}{|\mathbf{E}|} \tag{7.3}$$

where ϕ_a is the anode potential and $\mathbf{E}$ is the electric field along the ax-
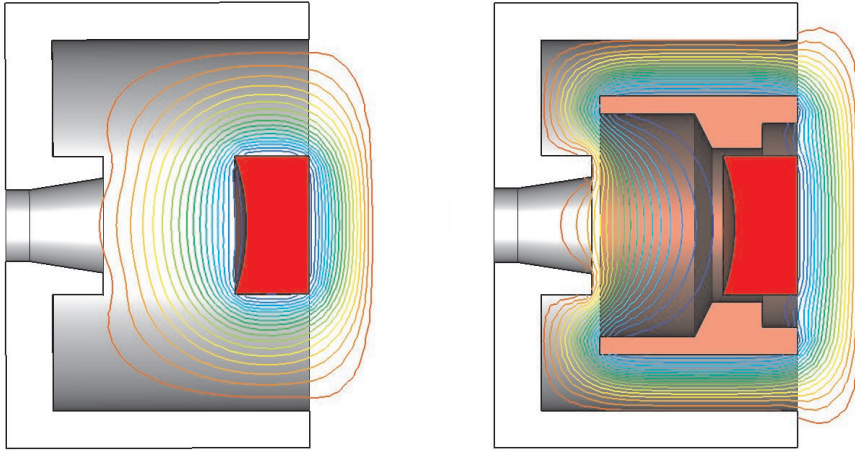
Figure 7.14: (a) Equipotential lines inside the electron gun without focusing electrode. (b) Equipotential lines with a focusing electrode. The focusing electrode forms a converging lens for the beam.

ial direction in the anode-cathode space, which can be calculated from the current-voltage relation of the conical diode.

Focusing Magnets :
The *TWTA* employs an axial magnetic field to confine the beam within the interaction region. For this reason *TWTs* are also referred as linear beam tubes, which means devices having magnetic field along the direction of the motion of electrons. The device under study uses *periodic permanent magnet (PPM)* focusing for this purpose. A stack of permanent magnets are placed end to end with reversed poles along the interaction region as shown in Fig. 7.16 to generate an axial, sinusoidal varying magnetic field. The *PPMs* are designed in such a way that there is no magnetic field extending into the electron gun and the beam is assumed to enter the interaction region in a laminar flow with no radial velocity components. The magnetic flux that is required to balance the space charge and centrifugal forces of the cyclotron motion is called *Brillouin flux* and the beam dynamics resulting from such a flux is called *Brillouin flow* [51].

If B_p is the peak magnetic flux and L the period of the magnets, then the magnetic flux along the axis of the tube can be written as

$$B = B_p \cos \frac{2\pi z}{L} \tag{7.4}$$
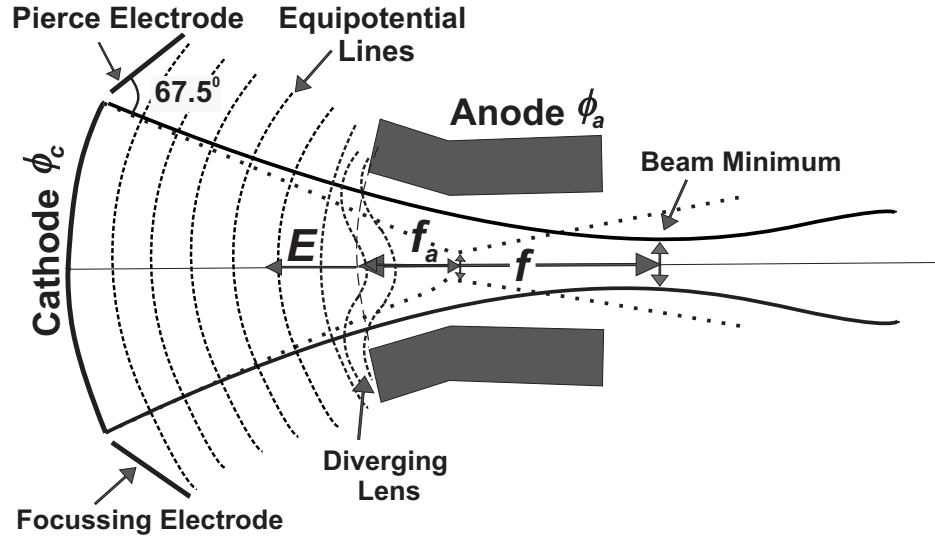
Figure 7.15: The focal length of the anode lens where the beam converges to the minimum radius shifts due to the diverging equipotential lines at the aperture.

The beam equation under the influence of above magnetic flux can now be written as

$$\frac{\partial^2 b}{\partial z^2} + b\left[\frac{\eta B_p}{2u_0}\cos\frac{2\pi z}{L}\right] - \frac{\eta I}{2\pi\varepsilon_0 u_0^2 b} = 0 \qquad (7.5)$$

where u_0 is the velocity and I the current of the beam respectively. Now taking the period of the focusing field as $T = 2/L$ and the cyclotron frequency $\omega = 2\pi u_0/L$ and substituting in the above equation gives

$$\frac{\partial^2 \Gamma}{\partial T^2} + \frac{1}{2}\left[\frac{\omega_L}{\omega}\right]^2 (1+\cos 2T)\Gamma - \frac{1}{2}\left[\frac{\omega_p}{\omega}\right]^2\frac{1}{\Gamma} = 0 \qquad (7.6)$$

where Γ is the normalized beam radius, $\omega_L = \eta B_p/2$ is the *Lamour frequency*, $\omega_p = 1/a\sqrt{2\eta I/\pi\varepsilon_0 u_0}$ is the average *Plasma frequency*, and a is the radius of the beam. Using these relations the magnetic coefficient and the space charge coefficient can be calculated. The beam is optimally focussed when these two

Figure 7.16: Periodic Permanent Magnets used for focusing electron beam along the axis of *TWTA*

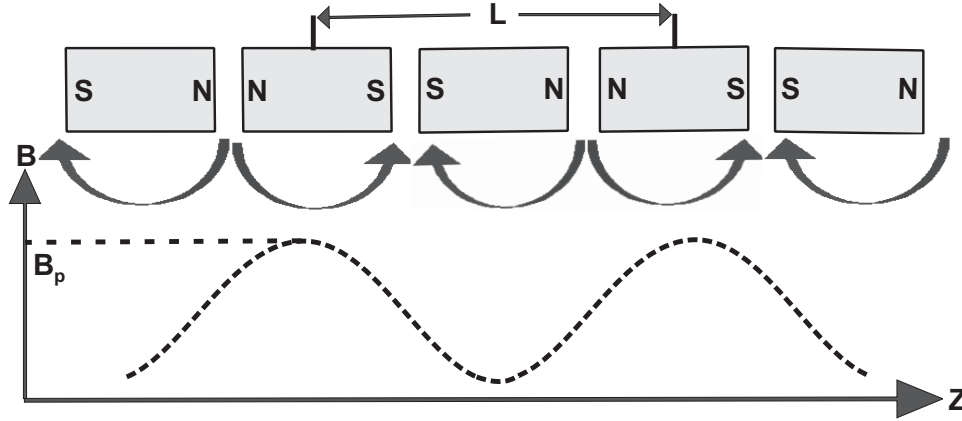coefficients are equal. Which means to say that when the *Lamour frequency* due to the magnetic field equals the cyclotron frequency of the plasma, the beam will be confined within the interaction structure. When the magnetic field coefficient is less than the space charge coefficient the beam diverges out of the interaction region due to insufficient focusing field and if the magnetic coefficient is in excess the electrons which are on the outer surface of the beam break into oscillations and escape out of the interaction region. A typical simulation of the magnetic fields for the *TWTA* can be seen in Fig. 7.17 and Fig. 7.18.

Interaction Region :
The interaction region is where weak radio frequency (rf) signals are amplified in a *TWTA*. This is achieved by coupling the energy of the electron beam that it acquires from the static fields of the anode-cathode gap, into the time varying *rf* signal by selecting a suitable structure for the interaction. Since the *rf* signal travels at the speed of light, it is impossible for the electrons to interact with it under normal conditions. Therefore a *slow-wave structure* such as the helix is used in the interaction region to bring down the axial velocity component of *rf* to that of electrons. The phase velocity of a time varying signal can be written as

$$V_p = \frac{\omega_\theta}{\kappa_n} \tag{7.7}$$

where ω_θ is the angular frequency of the wave, defined by the number of cy-
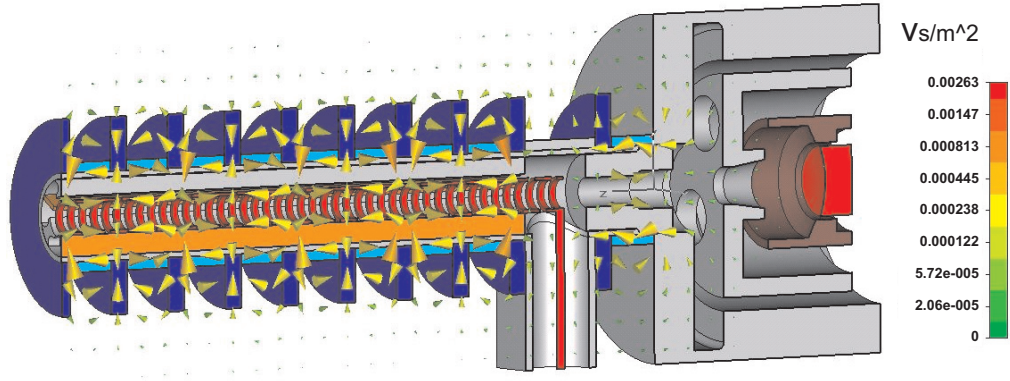
Figure 7.17: A Vector plot of the magnetic flux inside the interaction region of *TWTA*.

cles per unit time and κ_n the wave number, defined by the number of cycles per unit distance. Now if the *rf* signal is made to propagate on the helix, it would have to travel greater distance along the axial direction, which increases the wave number and assuming the helix to be non-dispersive, the phase velocity of the wave can be brought down. The reduction in the phase velocity would be equal to the pitch of the helix. By this arrangement, the phase velocity of *rf* is reduced to that of the axial velocity of electrons, which will have the effect that the electrons would see the same phase of the *rf* signal along the interaction region and an exchange of energy takes place, until the space charge forces become predominant and a steady state is reached. It has to be noted that the effect of the *rf* signal does not extend into the electron gun region and hence a static simulation of the emission is sufficient in the current problem.

7.3.1 Simulation of *TWTA*

The *TWTA* discussed above consists of an ungridded electron gun, a *rf* section (interaction region), a beam focusing section (magnets) and a collector, besides *rf* input and output. The emission problem requires only the simulation of the beam dynamics inside the electron gun and a part of the *rf* section to validate that the beam is launched correctly into the helix structure with the help of magnetic field. Therefore we remove the other half of *TWTA* along with the collector from our simulation. The technical specifications of the device are
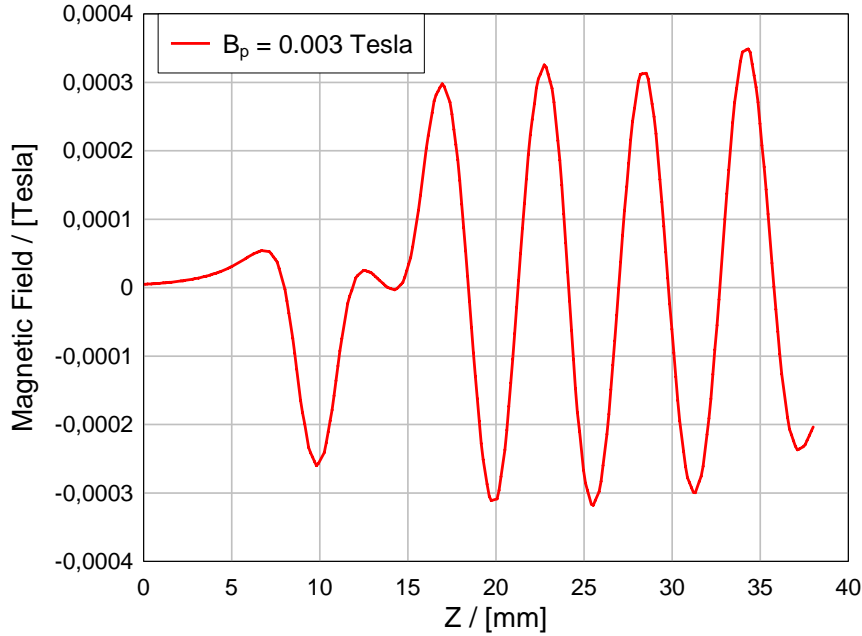
Figure 7.18: The magnetic field plotted along the axis of the tube. At the surface of cathode the magnetic field is almost zero and increases rapidly from the drift tube region where the beam starts to diverge due to space charge effects. The magnetic field along the tube keeps the beam within the helical interaction structure.

Operating Frequency	4.5 - 18 GHz
Cathode Potential (including focus electrode)	-4.55 kV
Anode Potential (including the body of *TWTA*)	Ground (0 V)
Cathode Radius	1.5mm
Peak DC current of the beam (pulsed mode)	$\approx 170mA$
Magnetic Field	0.003 Tesla

The model is discretized with a rectangular grid of nearly 2 million mesh cells and approximately 5000 particles in each time step. The emission is space charge limited and hence *Child-Langmuir law* is used for the calculation of the current. The simulation is performed using both the *Charge Conservation*, and *Virtual Cathode* methods. The operation of the *TWTA* in space charge regime can be visualized from the graph shown in Fig. 7.19.

The graph plots the electric field along the axis of the tube. The anode is at a potential of 4550 V with respect to the cathode and the surface of the

Figure 7.19: 19 The Electric field along the axis of *TWTA* with and without emission. The ordinate of the graph is the plane of the cathode.

cathode is the ordinate of the plot. It can be seen that when there is no emission the electric field increases gradually as we move towar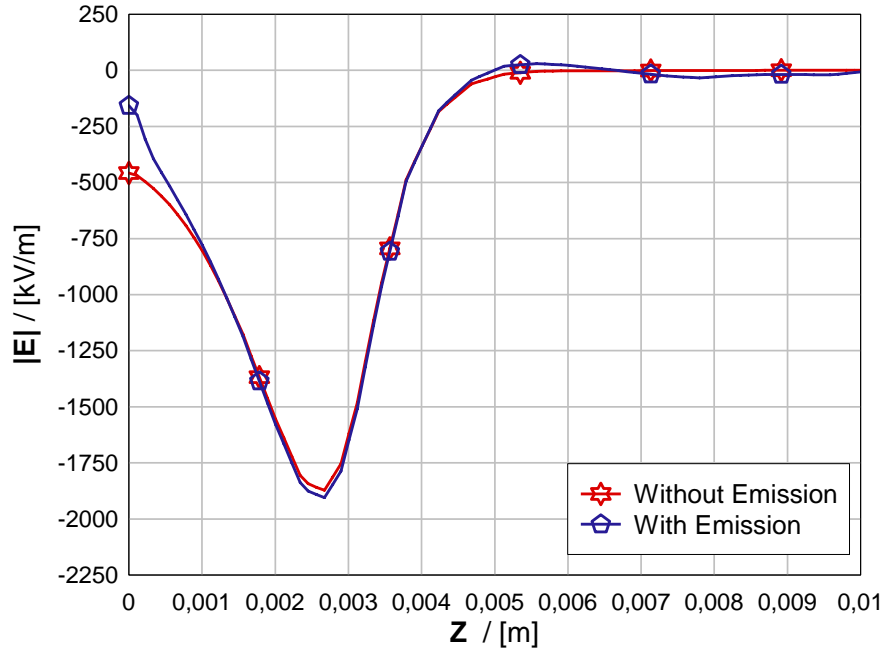ds the anode and after crossing the anode it falls off to zero since the rest of the tube is also at the same potential as anode and there is no dc electric field beyond. After the commencement of emission the electric field on the surface of the cathode drops due to the negative potential of electron space charge. The point where the emission curve deviates from the non-emission curve is the location where the space charge sheath (potential minimum) is located. If we move towards the anode, the space charge effects diminish, but beyond the surface of the anode, we see the electric field oscillating around zero, which is an indication of the space charge field. The oscillations will be more pronounced in the presence of the *rf* electric field, which is responsible for the bunching of electrons in the interaction region. If the tube was to be operated in saturation regime, the electric field would be so high that there would be no space charge cloud around cathode and the electric field on the surface of cathode will vary proportionately with the potential difference between the anode and cathode. But in space charge regime the electric field on the surface of the cathode is entirely dependent on the space charge potential. It can be seen that in practice, the electric field on the surface of cathode is
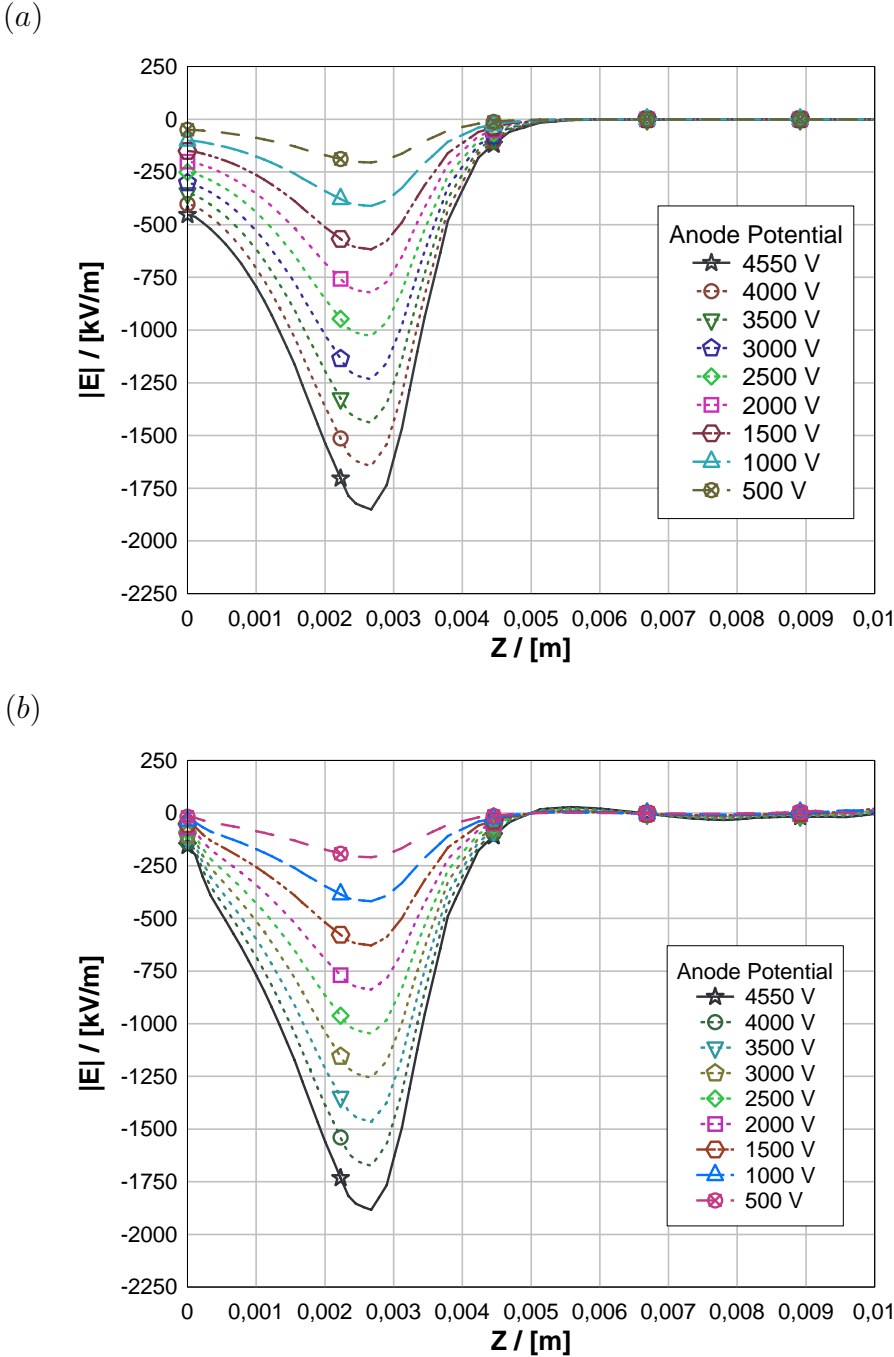
(a)

(b)

Figure 7.20: (a) Electric Fields along the axis of *TWTA* for different anode potentials. The plots are made prior to electron emission.
(b) Electric fields along the axis of the tube after the commencement of electron emission.

never zero even under space charge conditions contrary to the boundary condition we set to calculate the current. Under no space charge conditions the electric field is plotted along the axis for different anode potentials as shown in Fig. 7.20(a). The electric field on the cathode varies proportionately with the change in anode potential. In Fig 7.20(b) the electric fields are plotted after the commencement of emission. It can be seen clearly that the electric field on cathode is less influenced by the anode potential. The electric field drops to a minimum under space charge and varies very little from this value as we reduce the anode potential. At this point it has to be noted that in practice, reducing the anode potential beyond a certain minimum can cease emission altogether.

The charge is injected into the problem space with relaxation factor $\omega = 0.000002$, for which the charge residue (ratio of charge from two consecutive iterations) is found to be of the order of $1.0e - 06$. The trajectories of electrons are corrected in every iteration cycle after the fields are computed from the previous cycle. When the field-charge consistency is attained after the charge reaches within the give tolerance, the trajectories are well confined within the structure as can be seen in Fig. 7.21.

A thorough picture of the trajectories in the interaction region can be obtained by including the *rf* fields. But it can be seen from the electric field plots that the space charge fields inside the interaction region are very small when compared to the fields in anode-cathode gap, resulting in negligible effect of electron bunching on actual emission. The final current has been calculated using both the *Virtual Cathode* and *Charge Conservation* methods and is plotted in transverse coordinates along the surface of the cathode. The *Virtual Cathode* method uses a gap width of $0.0001m$ for the calculation of Child's law current. It can be seen from the graph Fig. 7.22, the current in the first time step is very large as the external fields are inconsistent with the *SCL* emission conditions. But within few iterations the charge converges well within the final steady state. When the residue reaches the given accuracy the iterations are stopped. The final steady state current is found to be $158mA$, which falls within 10 percent error of the peak DC current given in design specification mentioned previously. The simulation is then carried out with the *Charge Conservation* method with the same input conditions and the current is plotted across the cathode surface as shown in Fig 7.23. The final current in this case is found to be $161mA$, which is in very good agreement with the design specification.
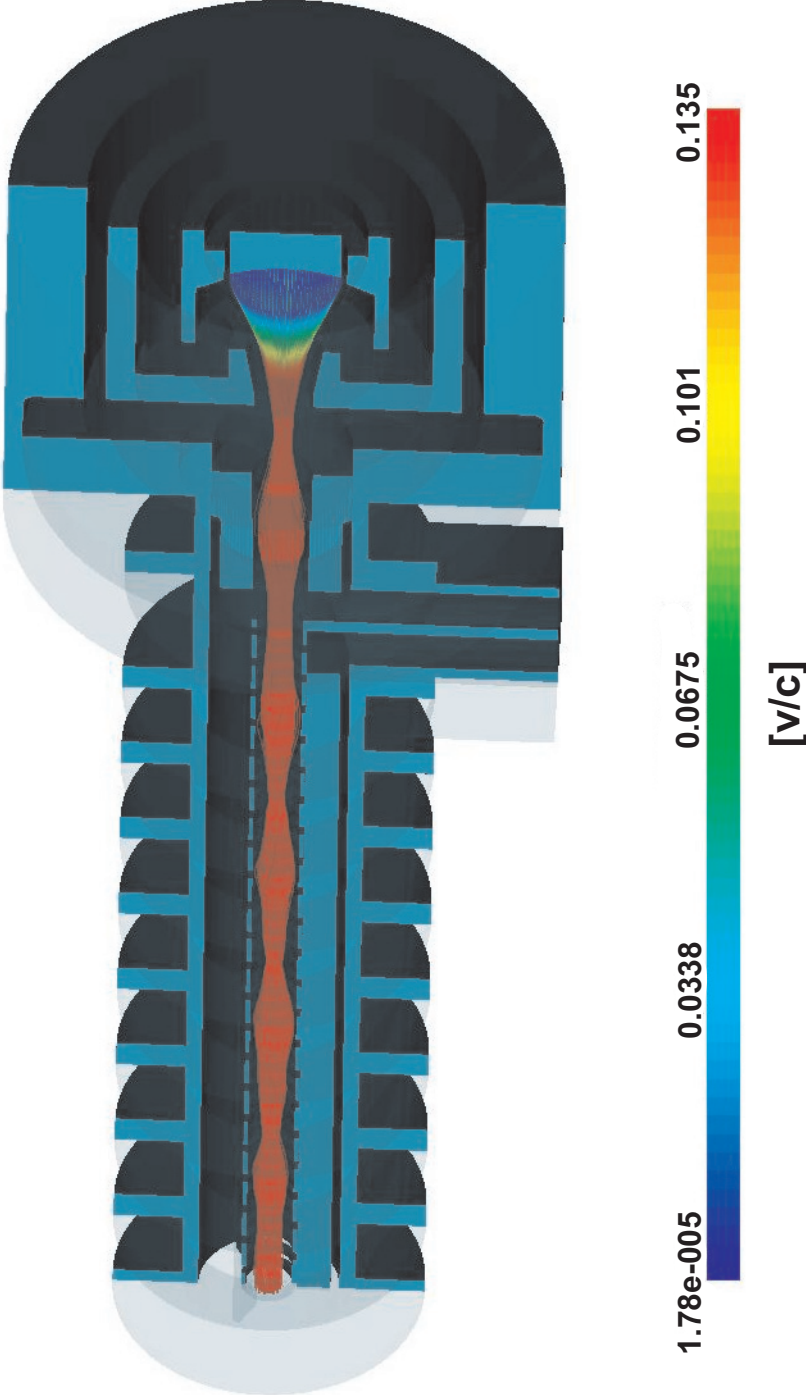
Figure 7.21: Trajectories of electrons along the length of the tube from the electron gun into the interaction region. The electrons acquire peak kinetic energy by the time they reach anode aperture. The beam then drifts under the influence of focusing magnetic field.
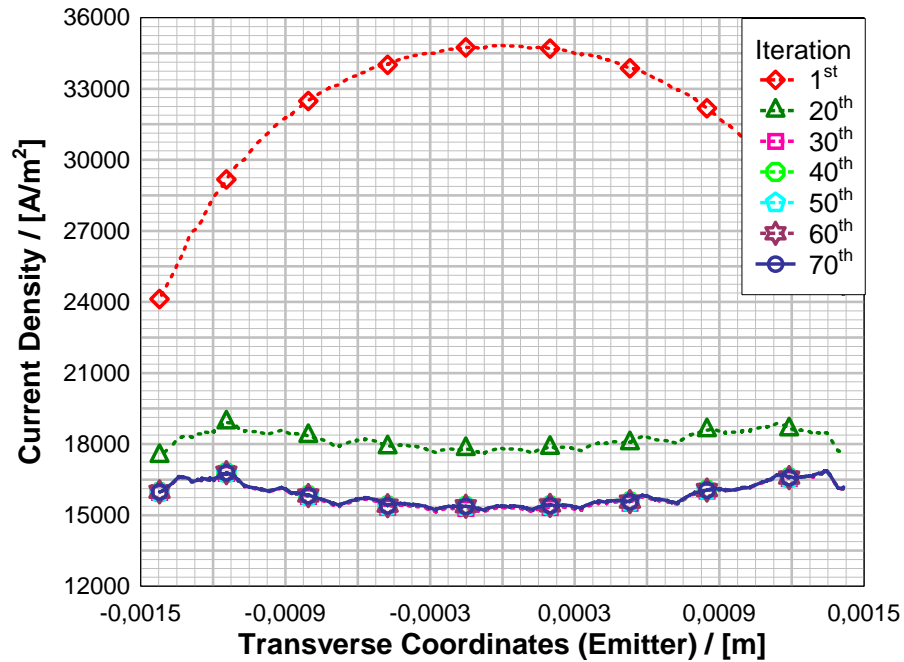
Figure 7.22: Plot of current across the surface of the cathode calculated with *Virtual Cathode* method. The current in first iteration is unphysical due to the incorrect fields inside the problem domain. After few iterations the current stabilizes to a final value and a steady state is reached.
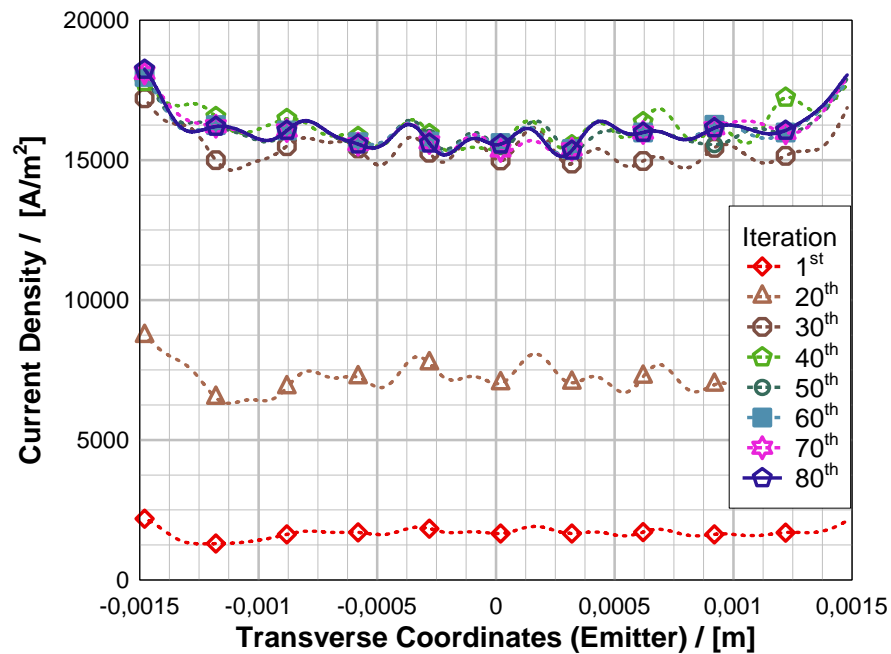
Figure 7.23: Plot of current across the surface of the cathode calculated using the *Charge Conservation* method. The Current gradually reaches steady state within few iterations and field-charge consistency is reached

7.3.2 Emission with Initial Velocities

The simulations until now have used a cold emission defined by zero initial velocities. But in a practical scenario the electrons are emitted with finite energy after they overcome potential barrier inside the metal [52]. Even though the boundary condition for *SCL* emission has zero electric field over the surface of the cathode, the emitted electrons can still have energy from the thermal excitation due to the heating of the cathode. The velocities of electrons emitted by thermal excitation can be written with the help of *Maxwell-Boltzmann* distribution function [53,54]

$$dN = \frac{Nmu_0}{kT}e^{-mu_0^2/2kT}du_0 \tag{7.8}$$

where u_0 is the velocity in normal direction and N the number of electrons that have velocities between the range u_0 and u_0+du_0 and T the temperature. Writing the above equation in terms of energy we have

$$\frac{dN}{N} = \frac{2}{kT}e^{-E_0/kT}dE_0 \tag{7.9}$$

where E_0 is the energy in normal direction. Rearranging the terms and taking logarithm on both sides we have

$$\ln\left[\frac{kTdN}{2NdE_0}\right] = -\frac{E_0}{kT} \tag{7.10}$$

The ratio inside the logarithm takes values from 0 and 1, which is nothing but the probability of finding the N electrons in a given velocity range. The normally directed velocity can now be written as

$$u_0 = \sqrt{\frac{2kT}{m}|-\ln(r_1)|} \tag{7.11}$$

where r_1 is a random number between 0 and 1. After obtaining the velocity, it has to be assigned to a particle in 3D space. The thermal electrons so obtained come out of the cathode in arbitrary directions and hence the above

calculated normal velocity should be assigned to a random vector coming out
of cathode Fig. 7.24(a).
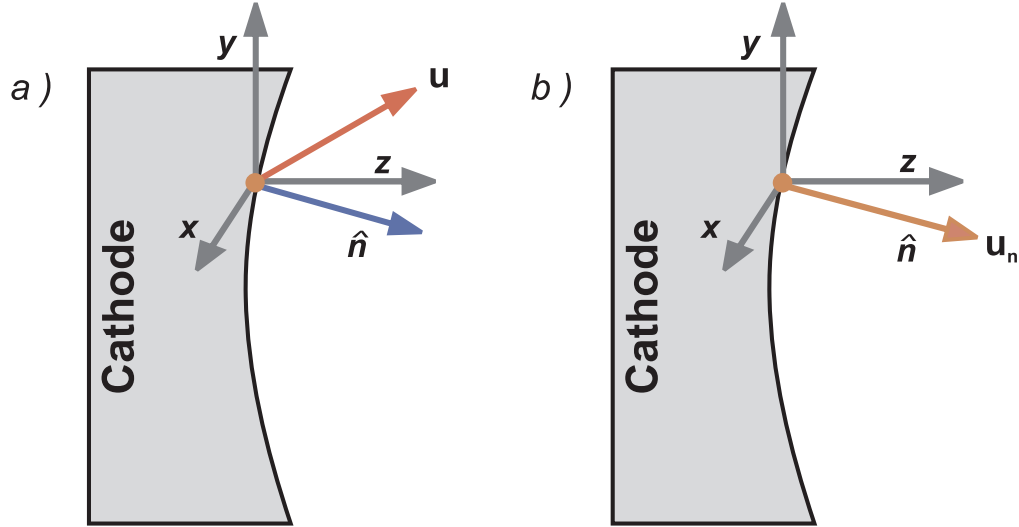
Figure 7.24: (a) Computational particles initialized with an arbitrary velocity
components over the surface of the cathode.
(b) Computational particles initialized with a normal velocity distribution
over the surface of the cathode.

If $x - y$ plane forms the transverse coordinates of the cathode, the velocity
obtained as above can be split into the three coordinates axes using the 3D
rotation matrix [55] as

$$\left.\begin{aligned}
u_x &= u_0 \cos(\pi/2 - r_2) \sin(\pi/2 - r_3) \\
u_y &= u_0 \sin(\pi/2 - r_2) \sin(\pi/2 - r_3) \\
u_z &= u_0 \cos(\pi/2 - r_3)
\end{aligned}\right\} \tag{7.12}$$

where r_1, r_2, r_3 are random numbers between 0 and 1 that generate random
angles in radians. Consequently the electrons can be assumed to come out of
cathode normal to the surface under high electric fields, which can be the case

in many practical problems. Under such conditions the normal component of velocity is much higher than the transverse components. The particles can now be emitted along the normal to the surface Fig. 7.24(b). The velocity of emitting particles can now be written as

$$\mathbf{u_n} = \mathbf{u_0} \cdot \mathbf{\hat{n}} \tag{7.13}$$

where $\mathbf{u_n}$ is the normal component of velocity and $\mathbf{\hat{n}}$ is the unit normal vector to the surface. The simulations have been performed with a much lower relaxation factor of $\omega = 0.0000002$ to obtain convergence when compared to that used in cold emission. This in-turn means more number of iterations that are required to reach a steady state. The temperature of the cathode is taken as $T = 2500^0 C$, which is a typical temperature of the cathode of the simulated $TWTA$. The final current for the three different cases of zero, arbitrary and normal initial velocities can be seen from the graph Fig. 7.25. It can be seen that the current for zero initial velocity agrees well with the previous result of $161mA$ and the current for initial velocities in arbitrary direction settles to a value of $163mA$ and that of normal velocities to a value of $165mA$.

The introduction of initial velocities is more pronounced at the edges of the cathode. More so in the case of normal velocities where the electrons emitted come out faster at the edges and result in pushing the space charge towards the center of the cathode. The convergence for the three cases can be seen in Fig. 7.26. It can be noticed that emission with initial velocities has an oscillatory convergence and a very low relaxation factor has to be used to keep the oscillations to minimum and obtain reasonable convergence. The convergence with normal velocities take more iterations to converge as the charge is injected faster into the problem space and the solution oscillates more than the other two cases before settling into the tolerance range. The thermal velocity distribution mentioned above does not include a spatial distribution over the surface of the cathode. If the temperature distribution over the cathode surface is given, a better initialization of the emission velocities can be made.
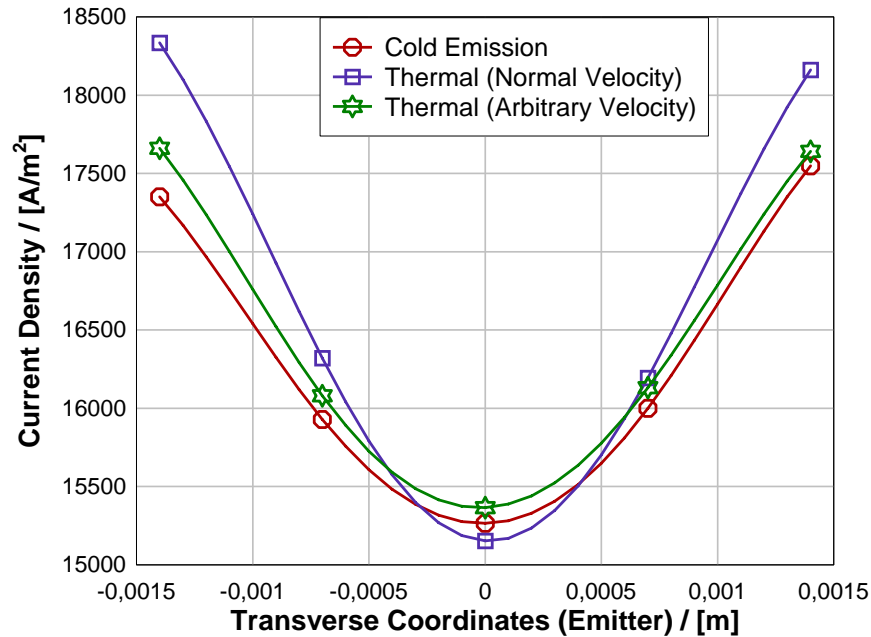
Figure 7.25: Final current along the transverse coordinates of the cathode for different initial velocity distributions. It can be seen that normal velocity distribution amplifies the current at edges thus pushing the charge towards the center and consequently a lesser current compared to other two plots. In case of arbitrary velocities an increase in the current can also be noticed.
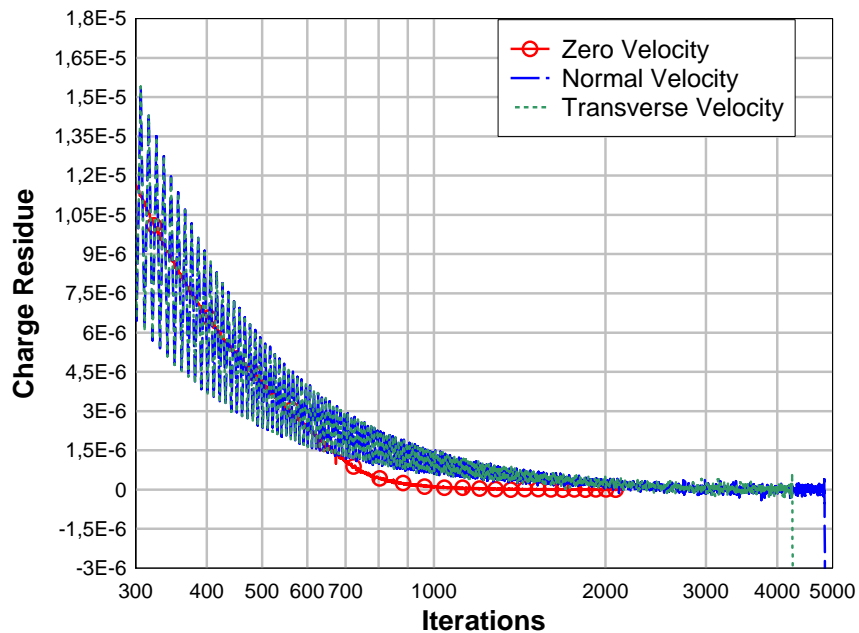
Figure 7.26: Convergence of the charge residue for all the three initial velocity distributions. It can be noted that the charge converges fast with no initial velocities, whereas in the other two cases convergence is slower. In other words, faster the induction of charge into problem space, slower is the rate of convergence.

Chapter 8

Summary and Outlook

The emission model presented in this work has many obvious advantages over the currently available simulation tools. The foremost of them is its ability to handle the exact curvature of the emission surfaces, which is vital in launching the electrons into the problem space without any errors that arise from boundary approximations. Most of the emission models are based on finite element or boundary element meshes, which require many operations and computationally cumbersome than the number of unknowns that can be easily solved with a simple dual orthogonal mesh system used in *Finite Integration Technique (FIT)*. The conformal field solutions increase the ability of the present model in exactly treating fields at the boundary, which in turn leads to the calculation of current and initial velocities with minimum error. The geometrical modeling of an emitter is the first step in ensuring a good spatial distribution of emitter samples that can closely represent the actual physical system. It has been shown that the *Gnu Triangulated Surface* libraries along with the constraints supplied by the emission problem, successfully execute the task of sampling the emission surface. The local mesh refinement, that can be performed with a cell based sampling is of great advantage in problems that have sharp curvature or emission tips such as *field emitter arrays (FEA)*. Hence the discretization of any practical emitters used in electron sources can be done with very good accuracy.

The *Particle-in-Cell (PIC)* method along with the *FIT*, offers a huge advantage of modeling electron-field interactions with good accuracy. The emission model here takes full advantage of this by initializing the particles in the conformal phase space. The model can interpolate fields on particle positions in the boundary cells using sub-grid information that enables in precise calculation of emission parameters. Based on the input specifications, the model can simulate thermal, field, photo or space charged limited emission. Besides

the traditional *Virtual Cathode* method, the space charge limited emission can also be modeled using *Charge Conservation* method, which offers obvious advantages over its predecessor. The simulations have been performed on planar, spherical and circular cylindrical diodes to validate that both methods conform well with the analytical solutions. Also a comparison has been made between both the methods and the characteristics have been analyzed. In the *Charge Conservation* method the advantage and ease of introducing thermal velocities to electrons at initialization has been highlighted. The electrons can be initialized with zero or arbitrary initial velocities using a thermal distribution function. The characteristics of the trajectory and time iterative algorithms has been discussed and verified. As an application, the *Traveling Wave Tube Amplifier* has been simulated using both the space charge limited emission algorithms and the results have been found to match well with the design specifications. This establishes that the model is accurate and can address any real time applications.

8.1   Outlook

There are few additions that can be made to the current model to enhance its application in simulation of a wide spectrum of devices. The first among them is emission in a time domain system. The *TWTA* that was simulated has no time varying fields effecting the emission. But in devices such as magnetron or other cross field tubes, the emitter can be under direct influence of *rf* fields and hence necessitates a thorough study using a time domain simulation. Also in such devices the emitter maybe under direct influence of the magnetic field, making it necessary to incorporate magnetic field into the phase space initialization of macro particles. The emission model also has to include a collisional emission to address the problems of secondary electron emission and primary emission due to ion or other particle collisions.

List of Notation

Mathematical Symbols

$\vec{r}$	Position vector
$d\vec{s}, d\vec{A}, d\vec{V}$	Infinitesimal length, surface and volume elements
$\Delta s, \Delta A$	Discrete length and surface elements
$\hat{u}, \hat{v}, \hat{w}$	Unit vectors of local coordinate system (u,v,w)
$\delta(x)$	Delta function
dx, dy, dz	Infinitesimal vectors in cartesian coordinates
du_x, du_y, du_z	Infinitesimal velocity vectors in cartesian coordinates
$\hat{n}$	Unit normal vector

Field Theory

$\vec{E}, \vec{H}$	Electric and Magnetic field strengths
$\vec{D}, \vec{B}$	Electric and Magnetic flux densities
$\vec{J}$	Electric current density
I	Electric current
ϕ	Electric potential
ρ	Charge density
ε_0	Permittivity of free space
$\varepsilon_r, \mu_r, \kappa$	Relative Permittivity, Relative Permeability and Conductivity
c	Velocity of light in free space
q	Charge

Finite Integration Technique

$G, \tilde{G}$	Primary and Dual grids
$L_r, \tilde{L}_r$	Primary and Dual grid edges
$A_r, \tilde{A}_r$	Primary and Dual grid faces
$V_r, \tilde{V}_r$	Primary and Dual grid volumes
$C, \tilde{C}$	Discrete Curl operator on primary and dual grids
$S, \tilde{S}$	Discrete Divergence operator on primary and dual grids

$D_s, \tilde{D}_s$	Diagonal matrices of primary and dual grid edges
$D_A, \tilde{D}_A$	Diagonal matrices of primary and dual grid faces
$M_\varepsilon, M_\mu, M_\kappa$	Material matrices
$D_\varepsilon, D_\mu, D_\kappa$	Diagonal matrices of averaged material parameters
$\hat{e}, \hat{h}$	Discrete electric and magnetic field vectors
$\hat{\vec{d}}, \hat{\vec{b}}$	Discrete electric and magnetic flux density vectors
$\hat{\vec{j}}$	Discrete electric current vector
q	Discrete grid electric charge

Theory of Electron Emission

E	Energy state inside a metal
E_f	Fermi energy level
$f(E)$	Probability distribution function
$n(E)$	Energy distribution function
dN	Velocity distribution function
k	Boltzmann's constant
n	Number of electrons per unit volume
T	Temperature in absolute scale
v	Infinitesimal volume element
ϕ	Work function
m, e	Mass and Charge of electron
u_x, u_y, u_z	Velocity components in cartesian coordinates
A_0	Richardson constant
V	Electric potential
$\vec{J}$	Electric current density
N	Number of electrons per unit surface area
ψ	Wave function
$\vec{E}_z$	Normal component of electric field
$T(E_z)$	Transmission coefficient of electron
a, b	Effective area of emission and Field enhancement factor
ν_0, λ_0	Cut off frequency and Cut off wavelength

Particle-in-Cell Method

$\vec{p}, \vec{v}$	Momentum and velocity vectors
Δt	Time step
$\vec{F}$	Lorentz force
$W(x)$	Weighting function
$F(x_p)$	Force interpolation function
$\rho(x_p)$	Charge interpolation function

N_p	Number of macro particles
H	Length of grid edge
m, q	Mass and charge of electron
Q	Total charge inside a cell

Space Charge Limited Emission and Applications

V, V_a, V_c	Potential difference between anode and cathode, Anode potential and Cathode potential respectively
V_{min}	Potential of the space charge cloud
Z_{min}	Position of the potential minimum
dZ	Infinitesimal length in normal direction
$\vec{u}$	Velocity vector
d	Distance between anode and cathode
η	Charge to mass ratio of electron
I	Total current over the surface of cathode
ϕ	Electric potential
r_a, r_c	Radius of anode and cathode respectively
$\vec{J}$	Electric current density
δ	Gap width in Virtual Cathode Method
Q_v, Q_e	Total Charge inside a cell, Total charge emitted from cathode
ω	Relaxation factor
f, f_a	Focal length of defocusing lens and focal length of anode respectively
E	Axial electric field
B, B_p	Magnetic field and peak magnetic field in axial direction
V_p	Phase velocity
ω_θ, κ_n	Angular velocity and Phase number of rf signal
u_0, u_n	Initial and Normal velocity of electrons
u_x, u_y, u_z	Velocity vectors in cartesian coordinates
E_0	Normal kinetic energy of electrons

Bibliography

1. LUDWIG BOLTZMANN: Lectures on Gas Theory, Dover Publications Inc, 1995.

2. CHARLES KITTEL: Introduction to Solid State Physics, John Wiley Sons Inc, 7th Edition, 1996.

3. A. H. W. BECK: Thermionic Valves their Theory and Design, Cambridge University Press, 1953.

4. OWEN W. RICHARDSON: Thermionic Phenomena and the Laws Which Govern Them, Nobel Lecture, 1929.

5. SCHOTTKY W.: Influence of Structure-Action, Especially the Thomson Constructive Force, on the Electron Emission of Metals, Physik Z. 15, 872-878, 1914.

6. SYLVAIN COULOMBE, JEAN-LUC MEUNIER: Thermo-Field Emission : A Comparative Study, Journal of Applied Physics 30, 776-780, 1997.

7. R. H. FOWLER, L. NORDHEIM: Field Emission, Proceedings of Royal Society London, A 119, 173, 1928.

8. J. D. JACKSON: Classical Electrodynamics, John Wiley Sons, 1999.

9. K. S. YEE: Numerical Solution of Initial Boundary Value Problems Involving Maxwell's Equations in Isotropic Media, IEEE-Transactions on Antennas and Propagation, Band 14, Nr. 3, S. 302-307, 1966.

10. T. WEILAND: A Discretisation Method for the Solution of Maxwell's Equation for Six-Component Fields, Electronics and Communication (AEU), Band 31, heft 3, S. 116-120, 1977.

11. T. WEILAND: On the Unique Solution of Maxwellian Eigenvalue Problems in Three Dimensions, Particle Accelerators, Band 17, S. 227-242, 1985.

12. T. WEILAND: Time Domain Electromagnetic Field Computation with Finite Difference Methods, International Journal of Numerical Modeling, Band 9, S. 295-319, 1996.

13. M. CLEMENS, R. SCHUHMANN, T. WEILAND: Algebraic Properties and Conservation Laws in the Discrete Electromagnetism, FREQUENZ, Band 53, Nr. 11-12, S. 219-225, 1999.

14. MARKUS CLEMENS, THOMAS WEILAND: Discrete Electromagnetism With the Finite Integration Technique, Journal of Electromagnetic Waves and Propagation, 2001.

15. P. THOMA, T. WEILAND: A Consistent Scheme For the Finite Difference Time Domain Method, International Journal of Numerical Modelling: Electronic Networks, Devices And Fields, Vol. 9, 359-374, 1996.

16. R. SCHUHMANN, T. WEILAND: The Nonorthogonal Finite Integration Technique Applied to 2D and 3D Eigenvalue Problems, Proceedings of the 12th Conference on the Computation of Electromagnetic Fields, Vol. 1, 134-135, 1999.

17. B. KRIETENSTEIN, R. SCHUHMANN, P. THOMA, T. WEILAND: The Perfect Boundary Approximation Technique Facing The Big Challenge of High Precision Field Computation, Proceedings of the XIX International LINAC Conference, 1998.

18. F. KRAWCZYK, T. WEILAND: A New Static Field Solver With Open Boundary Conditions in the 3D-CAD-System MAFIA, IEEE Transactions on Magnetics, Vol. 34, No.1, 55-58, 1988.

19. CST GmBH: MAFIA Ver. 4.x User Guide, www.cst.de, Computer Simulation Technology GmBH, Darmstadt, Deutschland, 2001.

20. CST GmBH: CST Microwave Studio Ver. 4.x User Guide, www.cst.de, Computer Simulation Technology GmBH, Darmstadt, Deutschland, 2001.

21. CST GmBH: CST Particle-Studio User Guide, Ver. 1.x, www.cst.de, Computer Simulation Technologies GmBH, Darmstadt, Germany, 2004.

22. H. SCHAMEL: Stationary Solutions of The Electrostatic Vlasov Equation, Journal of Plasma Physics, Vol. 13, 491-505, 1971.

23. R. W. HOCKNEY, J. W. EASTWOOD: Computer Simulation using Particles, Institute of Physics Publishing, Bristol and Philadelphia, 1988.

24. C. K. BIRDSALL, A. B. LANGDON: Plasma Physics Via Computer Simulation, Institute of Physics Publishing, 1991.

25. J. P. VERBONCOEUR: Particle Simulation of Plasmas : Review and Advances, Institute of Physics Publishing, Plasma Physics and Controlled Fusion, A231-A260, 2005.

26. C. K. BIRDSALL, D. FUSS: Clouds-in-Clouds, Clouds-in-Cells Physics of Many-Body Plasma Simulations, Journal of Computational Physics 135, 1997.

27. U. BECKER: Numerische Berechnung elektromagnetischer Felder in Wechselwirkung mit frei beweglichen Ladungen, Dissertation D17, Technische Universität Darmstadt, 1997.

28. S. HUMPHRIES: Charged Particle Beams, John Wiley Sons Inc., 1990.

29. ERION GJONAJ: Particle-in-Cell Simulations: Techniques and Applications, Workshop on Optimization and Coupled Problems in Electromagnetism, Napoli, 2003.

30. de BERG M., van KREVELD M., OVERMARS M., SCHWARZKOPF O.: Computational Geometry: Algorithms and Applications, 2nd Edition, Springer-Verlag, 2000.

31. Gnu TRIANGULATED SURFACE LIBRARY: The GTS Library, Release 0.7.4, http://gts.sourceforge.net/index.html.

32. C. D. CHILD: Discharge From Hot CaO, Physical Review 32, 492, 1911.

33. I. LANGMUIR: Theory of Electronic Conduction in a Space Devoid of Molecules or Positive Ions, Physical Review Letters Vol. 2, 1913.

34. C. B. WHEELER: Space Charge Limited Field Emission in a Parallel Electrode Geometry, Journal of Physics, Vol. 6, 1973.

35. THORNTON C. FRY: Potential Distribution Between Parallel Plane Electrodes, Physical Review Letters Vol. 22, 1923.

36. IRVING LANGMUIR, KARL T. COMPTON: Electrical Discharges in Gases Part II. Fundamental Phenomena in Electrical Discharges, Reviews of Modern Physics, Vol. 3, No. 2, 191-257, 1931.

37. IRVING LANGMUIR, KATHARINE B. BLODGETT: Currents Limited By Space Charge Between Concentric Spheres, Physical Review Letters Vol. 24, 49-59, 1924.

38. R. BECKER: Numerical Simulations in the Vicinity of the Virtual Cathode Regime, Proceedings of the International Symposium SCHEF '99 (Space Charge Effects in Formation of Intense Low Energy Beams), JINR Dubna, Russia, February 15-17, 1999, p. 19.

39. E. GJONAJ, T. LAU, T. WEILAND: Conformal Modeling of Space Charge Limited Emission From Curved Boundaries in Particle Simulations, Proceedings of the Particle Accelerator Conference, Vol. 5, 3563-3565, 2003.

40. STANLEY HUMPHRIES Jr.: Numerical Modeling of Space-Charge-Limited Charged-Particle Emission on a Conformal Triangular Mesh, Journal of Computational Physics 125, 488-497, 1996.

41. K. L. JENSEN, M. A. KODIS, R. A. MURPHY, E. G. ZAIDMAN: Space Charge Effects on the Current-Voltage Characteristics of Gated Field Emitter Arrays, Journal of Applied Physics Vol. 82, 845-854, 1997.

42. W. B. HERMANNSFELDT: EGUN-An Electron Optics Gun Design Program, SLAC-0331, Stanford, 1988.

43. DAVID M. YOUNG: Iterative Solution of Large Linear Systems, Dover Publications Inc, 1971.

44. Y. Y. LAU: Simple Theory for the Two-Dimensional Child-Langmuir Law, Physical Review Letters, Volume 87, No. 27, 2001.

45. A. S. GILMOUR Jr.: Microwave Tubes, Artech House Publishers, 1986.

46. A. S. GILMOUR Jr.: Principles of Traveling Wave Tubes, Artech House, Inc. , 1994.

47. J. R. PIERCE: Theory and Design of Electron Beams, D. Van Nostrand Company, 1954.

48. STEFAN SETZER: Design eines Integrierten 200 MHz Leistungsverstärkers für Linearbeschleunigerstrukturen, Dissertation D17, Technische Universität Darmstadt, 2003.

49. J. RODNEY, M. VAUGHAN: Synthesis of The Pierce Gun, IEEE Transactions on Electron Devices, Vol. Ed-28, No. 1-37, 1981.

50. LALIT KUMAR, ERWIN KASPER: On the Numerical Design of Electron Guns, Optik 72, No. 1, 23-30, 1985.

51. LEON BRILLOUIN: A Theorem of Larmor and Its Importance for Electrons in Magnetic Fields, Physical Review Letters, Vol. 67, No. 78, 260-266, 1945.

52. IRVING LANGMUIR: The Effect of Space Charge and Initial Velocities on the Potential Distribution and Thermionic Current Between Parallel Plane Electrodes, Physical Review Letters Vol. 21, 1923.

53. L. H. GERMER: The Distribution of Initial Velocites Among Themionic Electrons, Physical Review Letters, Vol. 25, 795-807, 1925.

54. J. R. PIERCE, L. R. WALKER: Brilllouin Flow with Thermal Velocities, Journal of Applied Physics, Vol. 24, No. 10, 1328-1330, 1953.

55. FREDERICK W. BYRON Jr., ROBERT W. FULLER: Mathematics of Classical and Quantum Physics, Dover Publications Inc., New York, 1992.

Acknowledgements

As I come to the end of this Dissertation, I would like to express my deep gratitude to all those who have directly and indirectly helped me produce this work.

First of all, I would like to thank Prof. Dr.-Ing. Thomas Weiland who gave me an opportunity to work at the *Institut für Theorie Elektromagnetischer Felder of TU Darmstadt.* I am deeply indebted to him for extending financial support and reviewing this work patiently.

I would also like to thank Prof. Dr.-Ing. Volker Hinrichsen for kindly reviewing this thesis as a co-referee.

No words can express my gratitude to Dr. -rer. nat. Erion Gjonaj for guiding me in my work. Without his unflinching support this thesis would have been impossible. His dedication to work, method of problem solving and helping nature will continue to inspire me for the rest of my career.

Special thanks goes to all my colleagues at the Institute who have helped me through scientific discussions and providing a friendly atmosphere that was a pleasure to work in.

I would also like to thank Prof. Dr.-Ing. Kartikeyan Machavaram for encouraging me to take up this work and also extending his experience in this area of research.

I extend my deep gratitude to Frau Stenger, Frau Selmanaj, Frau Seiler and Herr Veuskens for taking care of all administrative issues and helping me to focus on my work.

I also want to thank Herr and Frau Foeks, Mr. Ashok Kanumalla, Mr. Vamsi Krishna Palakuru, Mr. Bao Nguyen, Mr. Oleksandr Bedrynets and all my friends in Darmstadt and India who have helped me immensely during my stay away from home.

Finally, I am grateful to my parents and family who have supported me all these years. This work is the culmination of their faith in me and the values they have given us to lead a better life.

Curriculum Vitae

Jagadish C. Mudiganti
born on 18. April 1976 in Hyderabad, India

1981-1988   St. Andrew's Primary School, Hyderabad

1988-1991   St. Andrew's Secondary School, Hyderabad

1991-1993   Ideal Junior College, Hyderabad

1993-1996   Bachelor of Science from Osmania University, Hyderabad

1996-1998   Master of Science from Osmania University, Hyderabad

1999-2000   Worked as project scientist in Central Electronics Engineering
Research Institute, India

2000-2005   Worked as research assistant at *Institut für Theorie Elektromagnetischer Felder of TU Darmstadt.*